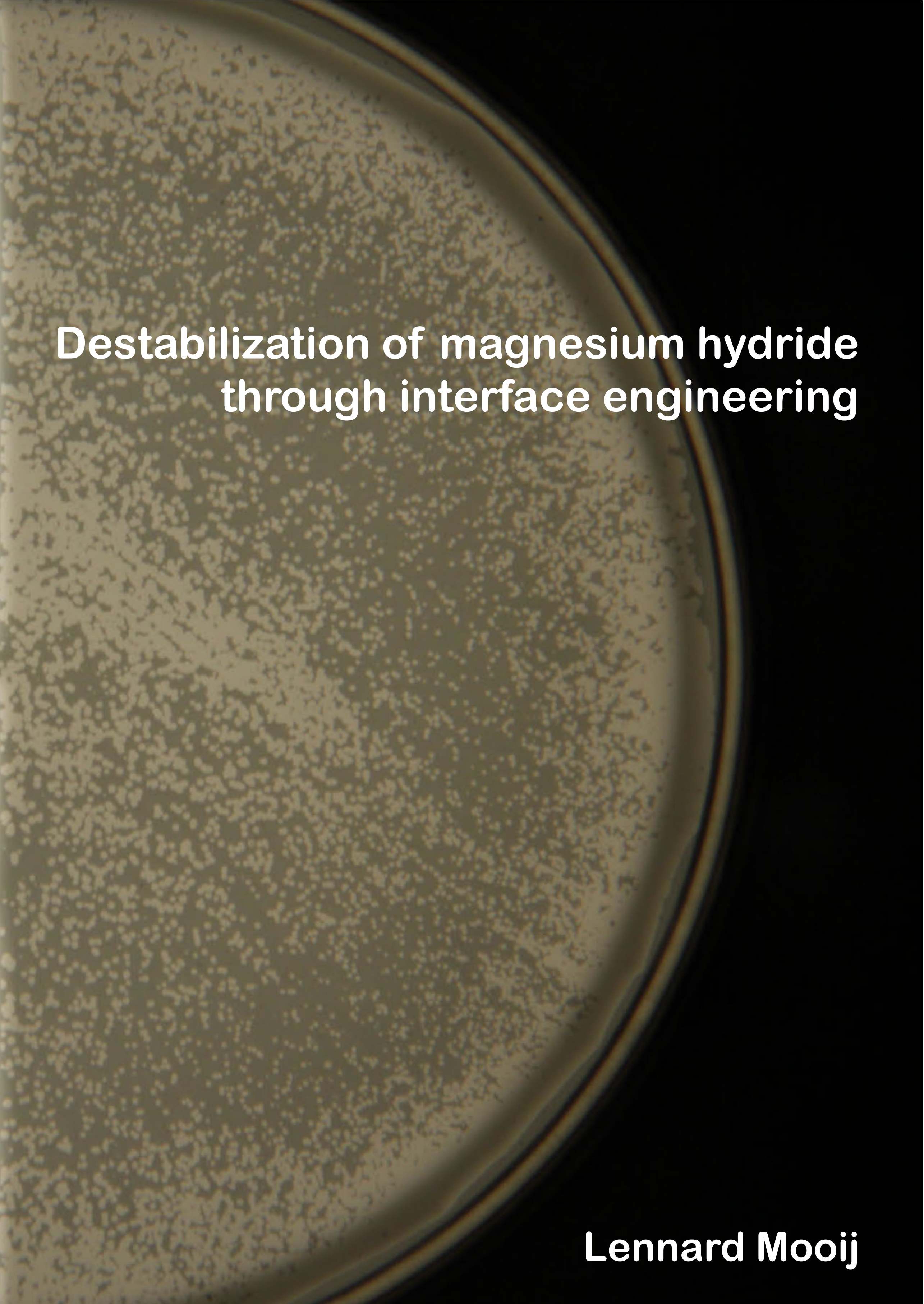

Destabilization of magnesium hydride through interface engineering

Lennard Mooij

Destabilization of magnesium hydride through interface engineering

PROEFSCHRIFT

ter verkrijging van de graad van doctor
aan de Technische Universiteit Delft;
op gezag van de Rector Magnificus prof. ir. K.C.A.M. Luyben
voorzitter van het College voor Promoties
in het openbaar te verdedigen op 1 oktober 2013 om 12:30 uur

door
Lennard Petrus Antonius MOOIJ
materiaalkundig ingenieur
geboren te Woerden.

Dit proefschrift is goedgekeurd door de promotor:
Prof. dr. B. Dam

Samenstelling promotiecommissie:

Rector Magnificus,	voorzitter
Prof. dr. B. Dam,	Technische Universiteit Delft, promotor
Prof. dr. B. Hjörvarsson,	Uppsala Universitet, Zweden
Prof. dr. J.J.C. Geerlings,	Technische Universiteit Delft
Prof. dr. P.H.L. Notten,	Technische Universiteit Eindhoven
Dr. P.E. de Jongh,	Universiteit Utrecht
Dr. G.H.L.A. Brocks,	Universiteit Twente
Dr. A. Borgschulte,	EMPA, Zwitserland
Prof. dr. F.M. Mulder,	Technische Universiteit Delft, reservelid

ISBN: 978-94-6186-184-9
Copyright © L.P.A. Mooij, 2013.
Graphic design by the author.
Printed by GVO drukkers & vormgevers, Ede.
Digital version available at http://repository.tudelft.nl

“You can’t stop the waves, but you can learn to surf.”

Swami Satchidananda

Contents

1 Introduction **7**

1.1 Sustainability and society . . . 7

1.1.1 The economics of sustainability . . . 8

1.1.2 Ethical aspects of sustainable energy . . . 8

1.2 Hydrogen . . . 10

1.2.1 Hydrogen as a renewable energy carrier . . . 10

1.2.2 Hydrogen storage . . . 10

1.3 Magnesium hydride . . . 13

1.4 Nanostructured metal hydrides . . . 14

1.5 Thin film metal hydrides . . . 16

1.5.1 Hydrogenography . . . 17

1.5.2 Magnesium thin films and multilayers . . . 19

1.6 This thesis . . . 21

2 Interface energy controlled thermodynamics **24**

2.1 Introduction . . . 24

2.2 Experimental . . . 25

2.3 Results and discussion . . . 26

2.4 Conclusion . . . 33

3 Hysteresis: The role of nucleation and growth **35**

3.1 Introduction . . . 35

3.2 Experimental . . . 38

3.3 Results . . . 40

3.3.1 Hysteresis scans of thin Mg layers . . . 40

3.3.2 Long time, low pressure hydrogenation: 2D-growth of the hydride phase . . . 46

3.4 Discussion . . . 49

3.4.1 Modeling of the lateral growth dynamics . . . 52

3.4.2 Absorption plateau pressure . . . 54

3.4.3 Deforming multiple layers: the edge boundary energy . . . 56

3.4.4 Mg thickness dependence . . . 58

3.5 Conclusion . . . 59

3.6 Appendix . . . 61

3.6.1 Edge boundary movement activation energy . . . 61

3.6.2 Pd thickness dependence of the lateral growth velocity 63

4 Nucleation and growth mechanisms 66
4.1 Introduction 66
4.2 Experimental 69
4.3 The JMAK equation for 2D nuleation and growth 69
4.4 JMAK analysis of hydrogen ab- and desorption 75
4.4.1 Absorption 75
4.4.2 Desorption 81
4.5 Conclusion 87

5 Mg/Pd alloys and multilayers 89
5.1 Introduction 89
5.2 Experimental 91
5.3 Results 92
5.3.1 Pd-capped Mg-wedge multilayers 92
5.3.2 $\mathrm{Mg}_{1-y}\mathrm{Pd}_y$ alloys 101
5.4 Discussion 111
5.5 Conclusion 113

6 Mg/Fe multilayers 114
6.1 Introduction 114
6.2 Experimental 116
6.3 Hydrogen ab- and desorption 117
6.3.1 Plateau width analysis 118
6.3.2 Plateau pressure analysis 123
6.3.3 Desorption 125
6.4 Structure and morphology 129
6.5 Discussion 133
6.6 Conclusion 138

Bibliography 139

Summary 146

Samenvatting 150

List of publications 155

Acknowledgements 157

Curriculum Vitae 159

Chapter 1

Introduction

The aim of this thesis is to study the thermodynamics of hydrogenation of nanoconfined magnesium within a thin film multilayer model system. Magnesium hydride is a potential material for hydrogen storage, which is a key component in a renewable energy system based on hydrogen. In bulk form, magnesium hydride is very stable, which means that hydrogen is released only at elevated temperature. Furthermore, the kinetics of hydrogen sorption is slow, which further hampers the practical use of this hydrogen storage material. A solution to both these issues may be found in nanoconfinement. At the nanoscale, the contribution of the surface (or interface) energy starts to play a large role and potentially destabilizes magnesium hydride. The kinetics is expected to improve due to the increased surface area and shorter diffusion lengths. With a thin film model system, the confinement of magnesium can be directly controlled by changing the magnesium layer thickness, as well as by changing the interfacing materials of the magnesium layer. The effect of the interface energy and further effects from nanoconfinement such as nucleation and growth, mechanical anisotropy and alloying are all investigated. These findings provide valuable insights for the optimization of nanosized hydrogen storage systems, thus paving the road to thin layered nanostructures enabling hydrogen desorption at 1 bar at room temperature.

1.1 Sustainability and society

Hydrogen storage materials are a potential part of an alternative, sustainable energy system. Technology by itself, however, can not solve our current global energy and environmental crises. The drive of society and its political leaders are equally, if not more, important. Therefore, in this section the broader scope of this thesis—a sustainable society—is explored. I wish to convey the ideas of several philosophers and scientists that, to my opinion, grasp the essence of our current energy and climate crisis.

1.1.1 The economics of sustainability

Because of the global financial recession of late 2008, governments are presently mostly focused on trying to increase consumption, the motor to economic growth. The idea that economic growth alone can bring prosperity to people seems deeply rooted in current thinking. The main problem with this dogma is that the coupling of growth to prosperity means that society will never be sustainable. Growth is unsustainable because it presupposes an infinite supply of raw materials, which is simply not available.

At the moment, the free market is unable to solve our ecological problems, because the costs to our ecology are externalized. Most notably, the costs of global warming due to anthroprogenic green house gases are potentially gigantic. Stern [1] estimates that at least 5% (and up to 20%) of the global gross domestic product (GDP) will be lost each year if we keep on going as we do now (*i.e.* business as usual scenario). The loss in GDP is due to, for instance, an increased number of natural disasters. Hence, these costs should be added to the prices of fossil fuels in advance. This proves difficult to do because the time lag prevents a clear accounting of the costs: Only in the second half of this century are the effects of climate change expected to contribute to a large extent of loss in GDP.

These huge costs of climate change to our future economy can be negated, but only if we act swiftly. Stern estimates that in order to limit the increase in global average temperature to 2 °C, we will have to invest about 1 to 2% of our current global GDP in renewable energy technology. Hence, if we act now, the cost savings will be enormous.

More recently, Carbon Tracker showed in their report Unburnable Carbon 2013 [2] that there is in fact enough capital available to invest 1-2% of the global GDP in renewable energy technology. The Unburnable Carbon report estimates that the current two hundred largest energy companies in 2012 alone invested $\$674{\times}10^9$ in the exploration and exploitation of new fossil fuel sources. These investments are, however, largely wasted if we wish to achieve a maximum of 2 °C global temperature rise: All these newly found reserves can simply not be burned. In fact, the 674 billion dollars is equivalent to 1% of the world GDP. Hence, if this amount is instead invested in renewable energy technology, it is possible to achieve the goal of stabilizing the global temperature. Furthermore, the return on investment (on a global scale) will be huge, because costs equal to 5-20% of the global GDP will never have to be paid.

1.1.2 Ethical aspects of sustainable energy

Although the economics of sustainable energy look very promising indeed, many still falsely argue that global warming is not real. Hence, here I approach the problem of fossil fuels and green house gas emission from a more ethical standpoint.

Whatever your point of view is on global warming, the emission of huge amounts of carbon dioxide into our atmosphere, without knowing the consequences beforehand, can only be described as a dumb experiment. This is even more true when considering that fossil fuel sources are finite—in the end, new energy sources will have to be used anyway.[3] It is therefore essential that society takes immediate steps towards achieving a sustainable energy system.

A different, but equally important argument starts with the precautionary principle: Whenever thinking of doing something that impacts the environment—such as building a power plant—only do so when you know beyond reasonable doubt that that impact is low. This principle is hardly ever practiced and understandably so: Besides having to define what a low impact is, this principle necessarily requires one to predict the future, which we may reasonably assume to be impossible. For instance, with respect to the impact of man-made CO_2 to climate change, the non-linear nature of the earth's climate does not allow for easy predictions. This is because we will never know the exact governing equations of the climate (if such a set of equations even exists). But it is exactly the non-linear nature of the climate that forces us to act conservatively, because in such a non-linear system, a tiny change of the input could dramatically alter the outcome. This is well described by the proverbial butterfly in India causing a hurricane in the Caribbean. Hence, when following the precautionary principle, the consequence is that we must be ecologically hyper-conservative.[4]

In any typical discussion on the anthroprogenicity of climate change, the burden of proof is often placed on the ecologically conservative. But the burden of proof should always be on the potential polluter. When we start from this principle, the discussion on whether global warming is caused by man or not is irrelevant: We don't know the precise effect of our gigantic emissions into the atmosphere, therefore we should not emit them in the first place.

If we follow the same line of thought, undoing the damage (*e.g.* removing CO_2 from the air) is not an ecologically sound action, as it might have an unknown (non-linear) effect on the climate that we do not know of beforehand.[4]

Of course, building a more sustainable energy system also has an impact on the environment, but less so than our current fossil fuel based system. In the end, we must still make a choice between the lesser of evils. The longer we postpone the choice, however, the higher the potential damage and the more difficult the inevitable transition will be.

1.2 Hydrogen

1.2.1 Hydrogen as a renewable energy carrier

The variable nature of renewable energy sources such as solar and wind power does not match with our nearly constant use of energy. This means that renewable energy has to be stored on a large scale, which for electricity is not trivial. Typically, electricity is converted to chemical energy by storage in batteries. The energy density of batteries is, however, relatively low. For instance, the gravimetric energy density of Li-ion batteries is typically ¡1 MJ/kg,[1] while that of gasoline is 45 MJ/kg. Hydrogen, on the other hand, has an even higher energy density of 120 MJ/kg. This energy density enables a car equipped with a fuel cell and 5 kg of H_2 to drive about 500 km, while for the same trip a normal car would require about 20 kg (25 L) of gasoline.

The use of hydrogen as a renewable energy carrier is summarized in the hydrogen cycle, shown in Figure 1.1.[6] This closed cycle comprises hydrogen production, storage and combustion. If produced in a sustainable way, there are no emissions other than the local emission of water. Sustainable hydrogen can be made by a combination of solar electricity and water electrolysis, as shown in the figure. A less expensive and promising option that is currently researched worldwide is direct water splitting with sunlight by photoelectrochemical devices.[7, 8]

Hydrogen storage is another key component of the hydrogen cycle, where for many applications the challenge lies in the reduction of the volume of hydrogen.

1.2.2 Hydrogen storage

A straightforward way of storing hydrogen is in high pressure gas cylinders. Typically, these cylinders are made of stainless steel and reduce the gravimetric density of hydrogen from 100wt% to about 2.5wt% (200 bar).[9] Liquid hydrogen provides an alternative, but requires energy to cool the hydrogen down. Furthermore, small liquid hydrogen tanks would lose all the hydrogen within two weeks due to boil-off.[9]

Hydrogen storage in metal hydrides offers a safe alternative, with higher volumetric densities than both high pressure hydrogen gas and liquid hydrogen. The thermodynamics of hydrogen ab- and desorption from these materials can be described in terms of so called pressure-composition isotherms. Figure 1.2a shows isotherms for a typical metal hydride. At low hydrogen pressure, the hydrogen concentration is low in the metallic phase (α-phase). Upon increasing the hydrogen pressure, at a certain point a phase transition occurs to the metal hydride phase (β-phase), indicated by the equilibrium plateau plateau pressure. This is the pressure where the two phases co-exist, similar to phase transitions such as the condensation of gases.

---

[1] The Li-air battery, still in the research stage, has a potential energy density of about 12 MJ/kg.[5]

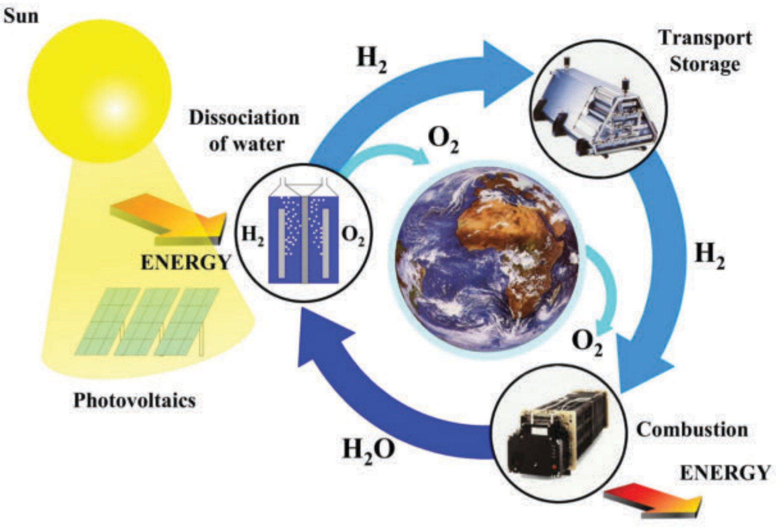
Sun
H$_2$
Transport
Storage
Dissociation
of water
O$_2$
H$_2$
O$_2$
ENERGY
H$_2$
O$_2$
Photovoltaics
Combustion
H$_2$O
ENERGY

Figure 1.1 The closed hydrogen cycle: Hydrogen and oxygen are produced via electrolysis of water with electricity. Here the electricity comes from photovoltaic cells, but any renewable electricity source may be used. The produced hydrogen is stored, transported and distributed. Finally, hydrogen is combusted together with oxygen in a fuel cell, which delivers work and heat. Adapted from [6] (© 2008 Wiley-VCH Verlag GmbH & Co).

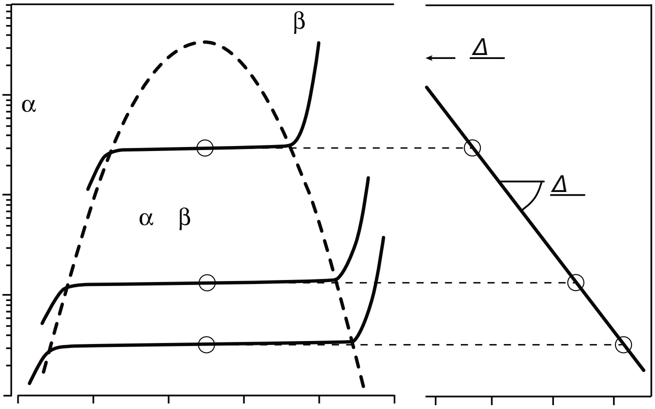

Figure 1.2 (a) Pressure-composition-isotherms of a typical metal hydride showing the phase transition from the H-dilute α-phase to the H-rich β-phase and (b) the corresponding Van 't Hoff plot, which relates the plateau pressures to the temperature. Adapted by permission from Macmillan Publishers Ltd: Nature, copyright 2001.[10]

With increasing temperature, the hydrogen pressure at which the transition to the hydrogen-rich phase occurs increases as well. The pressure-temperature relation is described by the Van 't Hoff equation:

$$\ln \frac{p}{p_0} = \frac{\Delta H}{RT} - \frac{\Delta S}{R} \tag{1.1}$$

with p the equilibrium pressure, p_0 the standard pressure (1 atm), R the gas constant ($8.314\ \mathrm{J/Kmol}$), ΔH the heat of formation of the hydride phase and ΔS the entropy change, both defined per mol H_2. For most metal hydrides, ΔS is equal to $130.8\ \mathrm{J/Kmol\,H_2}$. This is the entropy loss that hydrogen gas undergoes when absorbed into the metal, when hydrogen loses many degrees of freedom. Figure 1.2b shows the Van 't Hoff plot—a plot of $\ln \frac{p^{pl}}{p_0}$ versus $\frac{1}{T}$—from which ΔH is obtained from the slope and ΔS from the intercept with the y-axis.

A classical example of a hydrogen storage material is $LaNi_5H_6$, which has a volumetric H-density of about 118 kg H_2/m^3.[11] More importantly, the ab- and desorption of hydrogen to and from $LaNi_5$ occurs readily at room temperature at a pressure close to atmospheric pressure. Of course, the trade off is the weight of La and Ni, resulting in a poor gravimetric density of about 1.4wt%. This does not mean that there are no applications for a material such as $LaNi_5H_6$. In fact, at the end of the 1990's and early 2000's this material was popular in batteries (*e.g.* in mobile phones) because of its small volume and low weight compared to alternatives. Currently, $LaNi_5H_6$ is used as a hydrogen storage material in applications where the added weight does not matter, or is even beneficial. For example, forklifts need a counter weight to keep in balance. In hydrogen fuel cell forklifts the weight of the hydrogen storage material is hence not an issue. The much faster charging (several minutes) compared to batteries (about eight hours) offers a distinct advantage of fuel cell/metal hydride forklifts over battery powered forklifts.[12]

For other mobile applications, however, the weight is a critical issue. For this reason, light weight metal hydrides and complex metal hydrides are extensively investigated. The materials with the largest gravimetric hydrogen densities are the complex metal hydrides such as $NaAlH_4$ (7.5wt%), $NaBH_4$ (10wt%) and $LiBH_4$ (18wt%). All of these materials are, however, very stable and release hydrogen only at high temperature, because hydrogen is covalently bonded in the AlH_4 and BH_4 groups. Furthermore, the hydrogen dissociation reaction often occurs via multiple steps, which means hydrogen is released at several hydrogen pressures and/or temperatures. In some cases, removing all the hydrogen from the material makes the rehydrogenation impossible, which is highly impractical.

Hence, a light-weight, binary hydride offers practical advantages over the complex metal hydrides. Magnesium hydride is one of these binary hydrides.

1.3 Magnesium hydride

Magnesium—an abundantly available light metallic element—absorbs hydrogen to form magnesium hydride (MgH_2), which contains 7.6wt% hydrogen. The volumetric density is 119 kg H_2/m^3,[13] which means that 42 liters of MgH_2 contain enough H_2 for driving a fuel cell car 500 km.[2] Contrary to the complex metal hydrides, all of the hydrogen can be desorbed from magnesium hydride according to a single reaction:

$$MgH_2 \rightarrow Mg + H_2$$

The change in enthalpy of MgH_2 formation is -74.4 kJ/mol H_2 and the entropy change is -135 J/K mol H_2.[14] From the Van 't Hoff relation (Equation 1.1), it follows that the decomposition temperature at which hydrogen will desorb at a pressure of 1 bar is:

$$T_{dec} = \frac{\Delta H}{\Delta S}$$

Hence, for MgH_2 the decomposition temperature is 551 K, equal to 278 °C. This temperature severely limits the potential application of MgH_2 as a storage material because especially in mobile applications there is no waste heat available at such a temperature (*i.e.* from the fuel cell). Therefore, there have been many efforts of lowering the Mg-H bond energy by alloying with for instance Si [15], C [16, 17], Cu[18], V [19], Ni [20] and rare-earth elements [21, 22]. These approaches have varying rates of success, often the hydrogen cycling stability is low and all suffer from a reduced hydrogen storage capacity compared to pure MgH_2.

Furthermore, hydrogen diffusion in MgH_2 is very slow. Depending on the hydrogenation pressure and temperature, this can limit the hydrogen uptake of magnesium. It has been shown that often a MgH_2 shell is formed that greatly lowers the rate of hydrogen uptake. The result is that a large volume of untransformed Mg remains (Figure 1.3). The underlying reason for this slow diffusion in the hydride phase is probably its thermodynamic preference of forming stoichiometric MgH_2. Hydrogen diffusion is slow in this phase, because there are hardly any hydrogen vacancies.

Thermodynamically, hydrogen should desorb from MgH_2 at 278 °C. However, the desorption rate is low because of poor catalysis of the hydrogen association reaction ($2H \rightarrow H_2$). Therefore, the addition of a catalyst is required. Examples are transition metals[24, 25, 26], binary transition metal alloys[27, 28, 29] and metal oxides [30], which all enhance the (de)hydrogenation reaction.

Thus, the application of magnesium hydride as a hydrogen storage material requires many obstacles to be overcome. A solution to the hydrogen transport problem (due to the MgH_2 shell) and perhaps to the high stability of MgH_2 is found in nanostructuring.

---

[2] In a real system the MgH_2 storage tank would take up more volume as will the lost volume due to powder packing.

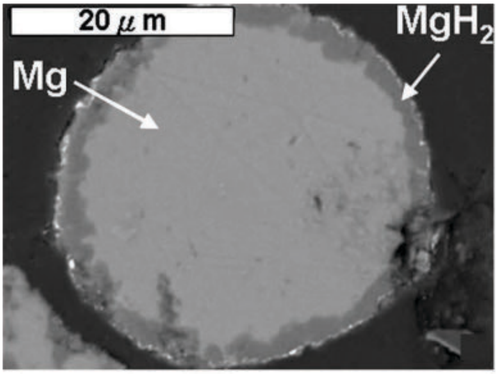

Figure 1.3 MgH_2 shell formation in on a Mg nanoparticle, resulting in a lowered hydrogen uptake. Copied from Tien et al. [23] with permission.

1.4 Nanostructured metal hydrides

At the nanoscale, changes in kinetics and thermodynamics of metal hydrides are expected because of an increased (reactive) surface area, shorter diffusion distances, increased density of grain boundaries and—for ternary and complex metal hydrides—a closer contact between the different metal constituents after desorption.[31] Indeed, nanosized magnesium hydride made by ball-milling can ab- and desorb hydrogen with fast kinetics.[32] Upon cycling with hydrogen, however, the beneficial effects tend to disappear because the nanoparticles agglomerate and grow.[33] Therefore, nanostructuring is not enough—the metal hydride nanoparticles have to be confined.

Methods to nanoconfine (complex) metal hydrides are, for example, melt-infiltration in nanoporous carbon [34], solution impregnation in carbon aerogels [35], solution infiltration in metallo-organic-frameworks (MOFs) [36] and preparation of nanoparticles in a core-shell geometry[37, 38]. Furthermore, Mg nanocrystals confined in a polymer matrix are shown to be insensitive to oxidation, which for Mg nanoparticles is essential.[39] All of these methods have shown the ability to produce metal hydrides with improved hydrogen (de)sorption kinetics. Some indications for changes in thermodynamics have been found in, for instance, $LiBH_4$ confined in nanoporous carbon, which shows a reduced desorption temperature compared to bulk $LiBH_4$.[40] However, an investigation on the underlying nature of this destabilization is so far not available. One possible reason to expect a change in the thermodynamics is from a change in the surface energy of the nanoparticle upon hydrogenation.

Surface/interface energy

If the surface energy of a metal particle changes upon hydrogenation to the metal hydride phase, this will affect the thermodynamics of hydrogenation. If the particle is large, the surface-to-volume ratio is small and the effect can be neglected. In a nanoparticle however, the surface-to-volume ratio is much larger. The simplest theoretical description of the surface energy effect is based on the Gibbs approximation, in which the surface has no volume and the rest of the particle is bulk. The hydrogenation of Mg goes according to the reaction:

$$\text{Mg} + \text{H}_2 \leftrightarrow \text{MgH}_2$$

For bulk Mg, *i.e.* large particles, the change in Gibbs free energy for the reaction is:

$$\Delta_r G^0 = G_{\text{MgH}_2} - G_{\text{Mg}} - G_{\text{H}_2} = \Delta_f G^0_{\text{MgH}_2}$$

with G_i the free energies of the corresponding phases, and $\Delta_f G^0_{\text{MgH}_2}$ the standard Gibbs free energy of MgH_2 formation from the elements. For a nanoparticle, we have to account for the surface energies of the present phases:

$$\Delta_r G^0_{nano} = (G_{\text{MgH}_2} + A_{\text{MgH}_2}\gamma_{\text{MgH}_2}) - (G_{\text{Mg}} + A_{\text{Mg}}\gamma_{\text{Mg}}) - G_{\text{H}_2}$$

Here A_i the surface area of the respective phases and γ_i the surface energy. Combining the above two equations:

$$\Delta_r G^0_{nano} = \Delta_f G^0_{\text{MgH}_2} + \{A\gamma\}_{\text{MgH}_2} - \{A\gamma\}_{\text{Mg}}$$

Formally we should take the anisotropy of the surface energies for different surface orientations into account:

$$\Delta_r G^0_{nano} = \Delta_f G^0_{\text{MgH}_2} + \sum_j \{A\gamma\}_{\text{MgH}_2|j} - \{A\gamma\}_{\text{Mg}|j}$$

with j the different surface orientations.

With the definition of the equilibrium constant K, we can relate $\Delta_r G$ to the hydrogen pressure (and find the Van 't Hoff equation [eq. 1.1]):

$$-\ln K = \ln \frac{p_{H_2}}{p_0} = \frac{\Delta_r G^0}{RT}$$

with p_0 the standard pressure (1 atm) and p_{H_2} the equilibrium hydrogen pressure. For the hydrogenation of bulk Mg this equation becomes:

$$\ln \frac{p_{bulk}}{p_0} = \frac{1}{RT}\left(\Delta_f G^0_{\text{MgH}_2}\right) \tag{1.2}$$

with p_{bulk} the equilibrium hydrogen pressure for bulk Mg. For nano Mg we find:

$$\ln \frac{p_{nano}}{p_0} = \frac{1}{RT} \left(\Delta_f G^0_{\mathrm{MgH_2}} + \sum_j \{A\gamma\}_{\mathrm{MgH_2}|j} - \{A\gamma\}_{\mathrm{Mg}|j} \right) \tag{1.3}$$

Now we subtract equation 1.2 from equation 1.3 and find:

$$\ln \frac{p_{nano}}{p_{bulk}} = \frac{1}{RT} \left(\sum_j \{A\gamma\}_{\mathrm{MgH_2}|j} - \{A\gamma\}_{\mathrm{Mg}|j} \right)$$

A further derivation depends on the shape of the Mg that is studied, it is further derived in Chapter 2 for thin film Mg. A general feature for spherical particles and thin films is that $\ln p_{nano} \propto 1/d$ (with d the particle diameter or film thickness), which follows from the surface-to-volume ratio.

With calculations of the surface energies of several metals / metal hydrides based on first principles, Kim *et al.* [41] used the above approach to calculate the effect on the thermodynamics of hydrogenation. They found that the surface energies for MgH_2 were slightly larger than those for Mg (*i.e.* $\Delta\gamma > 0$), which means that MgH_2 is destabilized compared to bulk MgH_2 when made sufficiently small—exactly what is required for MgH_2 as a hydrogen storage material.

The calculations by Kim *et al.* are, however, done for free surfaces in vacuum. Given the reasoning above—the nanoparticles have to be confined in some way—the surfaces of Mg and MgH_2 will be in contact with surrounding materials. This means that not the surface energy, but the interface energy should be considered. The derivation that considers interface energies is completely analogue to the above derivation for surface energies. Now, however, the effect of the interface energy will depend on the material that interfaces with Mg and MgH_2. It is not trivial to investigate the effect of the interface in nanoconfined particle systems, where first of all the preparation of a uniform sample, with uniform size and interface geometry, is difficult. Therefore, to enable control over size and surroundings of the Mg/MgH_2, in this thesis we nanoconfine Mg/MgH_2 in one dimension within thin film multilayers to study the effects of nanoconfinement (not limited to the interface energy).

1.5 Thin film metal hydrides

Research on thin film metal hydrides was inspired by the discovery of switchable mirrors by Huiberts *et al.* in 1996.[42] Figure 1.4 shows that upon hydrogenation of thin films of yttrium, the optical properties of the film change drastically. After hydrogenation, the checker board behind the previously reflective metal film can now be seen. The origin of this effect is the transition of Y metal to YH_3 semiconductor

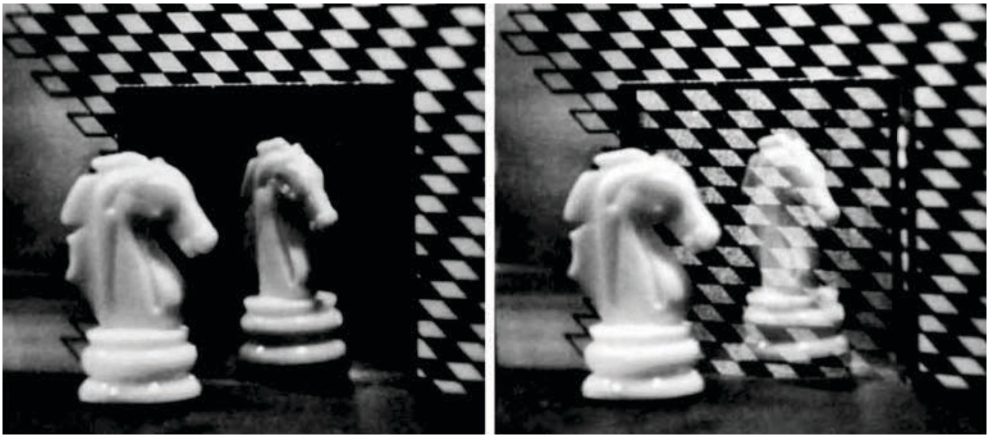

Figure 1.4 (left) A 600 nm reflective Y film capped with 10 nm Pd and (right) the same film hydrogenated to YH_3 is now optically transparent. Adapted by permission from Macmillan Publishers Ltd: Nature, copyright 1996.[42]

(with the intermediate formation of YH_2 metal). On a bare Y film, the formation of an yttrium oxide layer on yttrium inhibits hydrogen uptake. Therefore, a thin layer of Pd is deposited on the yttrium thin films. The Pd layer protect against oxidation and dissociates and absorbs hydrogen, which then diffuses to the yttrium layer. The large change in optical properties allowed for the investigation of, among others, H-diffusion in Y and La [43], the hydrogenation kinetics of YH_x [44] and a combinatorial approach to the investigation of alloys [45] and catalysts for H-uptake [46]. Furthermore, the technique Hydrogenography was developed which measures the thermodynamic properties of metal hydrides based on the optical changes occurring as a function of temperature and hydrogen pressure.

1.5.1 Hydrogenography

Many techniques exist to measure the thermodynamical properties of metal hydrides. A classical example is Sievert's method, which is based on controlling the volume of hydrogen exposed to a sample. Upon introducing a known volume of hydrogen into a hydrogenation cell, the measured pressure drop gives the absorbed volume of hydrogen by the sample. In this way, the equilibrium values of hydrogen pressure and concentration can be obtained. Another method relies on recording the weight of the sample, which becomes heavier if hydrogen is absorbed. These techniques are usually not suitable for the small sample volumes found in thin films. Other techniques such as X-ray or neutron diffraction can detect the change in lattice parameter or structure transitions and thereby identify the metal to metal hydride transition, but

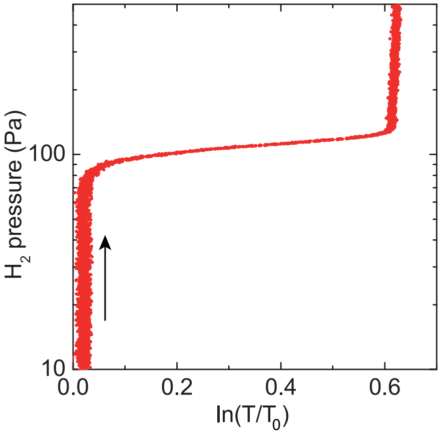

Figure 1.5 An example pressure-transmission-isotherm of the hydrogenation of a 10 nm Mg thin film (absorption). Given the signal-to-noise ratio of this 10 nm layer, the hydrogenation of a 1 nm Mg layer can easily be measured.

the time resolution is typically rather low.

The optical change, however, can be large even for very thin films. Based on this principle, Gremaud *et al.* developed the experimental method Hydrogenography, which measures the hydrogenation thermodynamics and kinetics from the change in optical transmission of thin films as a function of hydrogen pressure and temperature.[47] This technique does not only work for metal-semiconductor transitions, but equally well for metallic hydrides such as Pd.[48] Similar techniques have been developed of which one example is the use of the shift in the optical plasmonic resonance to detect hydrogen.[49]

A Hydrogenography measurement gives the change in optical transmission as a function of the applied hydrogen pressure and temperature. Hence, instead of pressure-composition-isotherms, now pressure-transmission-isotherms (PTIs) are recorded. An example PTI for the hydrogenation of a 10 nm Mg thin film is shown in Figure 1.5. The optical transmission is taken as $\ln {}^{T}\!/_{T_0}$, with T the measured optical transmission and T_0 the transmission at time zero—the start of the experiment. The natural logarithm of T/T_0 is found to be proportional to the amount of MgH_2—and thereby to the Mg layer thickness—based on both experiments and Lambert-Beer law.[50]

Hydrogenography moreover is a combinatorial method, capable of scanning a changing parameter across a single thin film sample (the parameter can be *e.g.* alloy composition, layer thickness, catalyst composition). Hence, in effect, many samples are measured at the same time under exactly the same conditions. A schematic drawing of a hydrogenography setup is shown in Figure 1.6a, where a white light

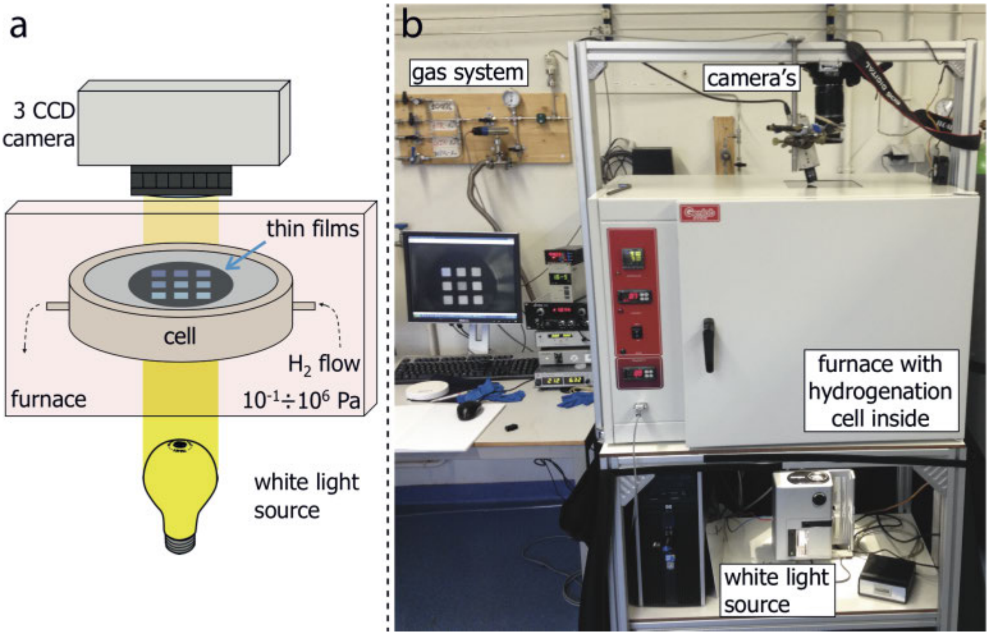
a
3 CCD camera
thin films
cell
H_2 flow
furnace
$10^{-1}÷10^{6}$ Pa
white light source
b
gas system
camera's
furnace with hydrogenation cell inside
white light source

Figure 1.6 (a) Schematic overview of a Hydrogenography setup and (b) a photo of the setup including the gas system and computer control.

source shines through the sapphire windows of a stainless steel hydrogenation cell which contains the thin film sample(s). The hydrogenation cell is placed in a furnace to control the temperature. One can choose to measure (a combination of) up to nine 10x10 mm samples, three 70x5 mm gradient samples or one single 3" wafer sample. The change in optical transmission of the samples is typically recorded with a 3-CCD camera, while for experiments that require a higher image resolution a Canon EOS 550D is mounted—as shown in Figure 1.6b.

1.5.2 Magnesium thin films and multilayers

Hydrogengraphy was used as a tool to find new Mg-based alloys for hydrogen storage. Binary alloys (such as Mg-Ni[51], Mg-Al [52] and Mg-Ti [53]) were investigated, but also ternary alloys (Mg-Ni-Ti [54] and Mg-Ti-Al[55]) were studied. One sample can cover a large range of the binary and ternary phase diagrams, which results in measurements of the thermodynamical properties for thousands of compositions at the same time. From these results, several promising compositions were found for hydrogen storage at suitable conditions, although these results have yet to be verified.

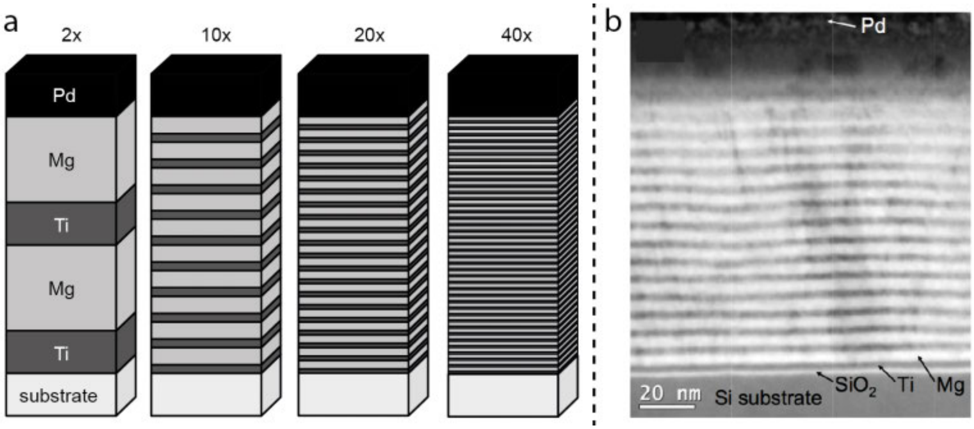

Figure 1.7 (a) Mg/Ti multilayer geometries with constant total thickness and varying repetitions and Mg/Ti layer thicknesses [57], and (b) a cross section TEM image of a 20x multilayer sample. Reprinted figure with permission from Baldi et al., Phys Rev B 81, 224203 (2010). Copyright (2010) by the American Physical Society.[56]

Especially interesting is the Mg$_y$Ti$_{1-y}$ system. Although Mg and Ti are immiscible, with the physical vapor deposition technique magnetron sputtering a single phase alloy is still made because of the rapid quenching on the substrate. Borsa *et al.*[53] found that the hydrogenation properties are strongly influenced by the Ti concentration. For $y > 0.87$ the alloy hydrogenates in the tetragonal (rutile) phase, similar to the structure of MgH$_2$. For $y < 0.87$, the hydride phase has a fcc (fluorite) structure, which is the structure of pure TiH$_2$. It was found that the local order of Mg was an important parameter to explain the hydrogengraphy results. Despite the rapid quenching during the deposition process, still locally Mg and Ti partially segregate, resulting in Mg having a higher likelihood to have Mg as a nearest neighbor than expected from a random alloy. To enable the direct control of the local order of Mg, multilayers of Mg/Ti were made with varying Mg and Ti thicknesses (Figure 1.7).[56] The hydrogenation of the multilayers has indeed been shown to be roughly the same as the Mg-Ti alloys with equal local ordering of Mg.

In the 2x Mg/Ti multilayer samples, the top Mg layer—which is Pd-capped—behaves differently than the bottom Mg layer which is surrounded by Ti layers. The absorption pressure for the Pd-capped Mg layers is found to be orders of magnitude larger, and furthermore this effect is enlarged when the Mg thickness is decreased (from 40 to 10 nm).[58] Alloying at the interface was found to be a governing property, because the same effect was found for Ni (which alloys with Mg), but not for V, Nb and Ti (all immiscible with Mg). Baldi *et al.* [58] proposed that the increase in absorption pressure is due to the elastic clamping of the interface alloy on the Mg layer. The basis for this interpretation lies in the hydrogen-hydrogen (H-H) interaction. If hydrogen dissolves in a medium that is free to expand, the medium will expand (tensile) and it will be favorable for the next H-atom to dissolve into the medium is well. When, on the other hand, the medium is not free to expand, the dissolution of one hydrogen atom will cause a net compressive stress. The elastic clamping model predicts, however, that upon desorption the effect should be equally large, *i.e.* the desorption pressure should increase with the same amount as absorption. However, the hydrogen desorption isotherms of these Pd-capped Mg layers were not measured.

Clamping to the substrate is one example of how the hydrogenation of thin films can not be directly extrapolated to a bulk hydrogen storage material. Pivak *et al*. [59] have shown an increased hysteresis of the hydrogenation of Pd strongly adhering the substrate compared to free Pd. Furthermore, the hydrogenation of 50 nm Mg films was found to show increased hysteresis as well, although the measured enthalpy and entropy values are very similar to bulk values.[60] One reason why thin films behave differently from bulk is the anisotropy of the mechanical deformation upon hydrogenation of the thin metal film. For strongly adhesive thin films, it is found that the volume expansion due to hydrogen absorption is completely accommodated by the out-of-plane expansion of the thin film.[61] This process requires plastic deformation of the film to release the stresses, which weakly adhesive films may release by forming buckles.[62]

When investigating nanoconfinement effects, however, these thin film effects may be equivalent to effects in nanoparticle samples. For instance, Mg confined in a rigid shell may behave similar to a Mg layer clamped by the substrate and/or interface alloy. To investigate nanoconfinement effects on the hydrogen sorption of Mg, Ti-surrounded Mg is an ideal system to start with. The immiscibility of Mg and Ti make sure that no alloying is to be expected. Furthermore, upon the first exposure to hydrogen of such a thin film, Ti will absorb hydrogen to form highly stable TiH_2. This results in a stable interface upon cycling with hydrogen, which explains why Ti-sandwiched Mg layers behave as bulk when their thickness is larger than 10 nm. Hence, in such a sample only physical effects such as from the interface energy will influence the hydrogenation behavior of magnesium / magnesium hydride.

1.6 This thesis

This thesis investigates the effects of size and local surroundings on thin magnesium layers. Following the interface energy effect described above, if the interface energy of the MgH_2/TiH_2 interface is larger than the one for Mg/TiH_2, we expect that MgH_2 destabilizes compared to bulk Mg. The magnitude of destabilization is a function of the interface-to-volume ratio, which for thin films is equal to $A/V = 1/d_{Mg}$—with d_{Mg} the Mg layer thickness. Earlier experiments, however, point out that for Mg layers of 20-50 nm no significant difference of the hydrogenation pressure is observed compared to bulk Mg.[63, 60] Therefore, in Chapter 2 we investigate what happens at larger interface-to-volume ratios, equivalent to thinner magnesium layers (2-10 nm). The results show that indeed there is an interface energy effect that causes the destabilization of MgH_2 compared to bulk. A ten-fold increase in the absorption pressure is observed for 2 nm Mg compared to 10 nm Mg. For hydrogen desorption, however, we find that the destabilization is smaller than for absorption. This effectively means that the hysteresis—the difference between the ab- and desorption plateau pressures—increases with decreasing d_{Mg}.

To investigate whether this hysteresis broadening is caused by nucleation and growth effects, in Chapter 3 we measure sub-hysteresis isotherms (hysteresis scans) of a 10 nm and a 3.1 nm magnesium layer. For hydrogen absorption (MgH_2 nucleation in Mg), the effects of a nucleation barrier are that the Mg phase will be metastable until the driving force is large enough to overcome the nucleation barrier. For these hydrogen absorption experiments, an increased driving force is equivalent to an increased hydrogen pressure. For desorption (Mg nucleation in MgH_2), the same reasoning applies but a larger driving force now means a lower hydrogen pressure. During a hysteresis scan, the direction of a measured isotherm is reversed in the middle of the phase transition (*i.e.* from increasing to decreasing pressure or *vice versa*). Hence, at the point of switching in a hysteresis scan, already MgH_2 or Mg (ab- or desorption) have nucleated. What we found is that, for 10 nm Mg layers, the observed hysteresis from a hysteresis scan is indeed smaller than the hysteresis of complete isotherms. Especially the absorption plateau pressure is increased due to the barrier for MgH_2 nucleation.

Furthermore in Chapter 3 we describe how, under special conditions, we can optically detect the growth of MgH_2 domains. The growth occurs in-plane, parallel to the substrate. The nucleation mechanism, however, is more difficult to observe. Therefore, in Chapter 4 we use the Johnson-Mehl-Avrami kinetical model to investigate the nucleation and growth mechanism in further detail, also as a function of the driving force (applied H_2 pressure). The nucleation mechanism that is expected from the interface energy model is that, upon hydrogenation, the top and bottom Mg/TiH_2 interfaces are instantly replaced with MgH_2/TiH_2 interfaces. Only then will the measured plateau pressure account for the exchange of interfaces. We find that, while for hydrogen absorption such a mechanism may be valid, the desorption mechanism is certainly different. Hence, this indicates that the ab- and desorption processes are highly asymmetric. Both in Chapter 3 and 4, we propose that the origin of this asymmetry is the mechanical deformation of the Mg and overlying TiH_2 and Pd layers. Additional evidence that supports this interpretation is given in the Appendix to Chapter 3.

In Chapter 5, we attempt to unravel the underlying mechanisms of the hydrogen ab- and desorption behavior of Pd-capped magnesium layers. Upon hydrogen absorption a large increase in the plateau pressure was observed, which was explained by the elastic clamping of the Mg layer by an interface alloy.[58] More recently, Chung *et al.* [64] proposed that the MgH_2 is destabilized by the enthalpy effect of the alloy formation. Both of these models predict that the desorption plateau pressure is increased by the same amount as the absorption pressure. While desorption isotherms are essential to validate these models, they were not measured. In Chapter 5 we show that the desorption pressure is not significantly affected by the presence of Pd, which counters both the elastic clamping and interface alloy models. These results are compared to Mg-Pd alloys, which show a similar asymmetry between the ab- and desorption pressures. The microstructure and morphology of these alloys is, however, completely different than the Pd-capped samples. This chapter investigates the origin of the unexpected similarities in ab- and desorption isotherms and dissimilarities in the structural and morphological properties of these MgPd alloy and Pd-capped Mg samples.

In Chapter 6, we return to the physical destabilization of magnesium hydride via the interface energy. In an attempt to increase the destabilization effect, we investigate what happens when the interfacial material TiH_2 is exchanged with Fe. Similar to Ti, Fe is immiscible with Mg. Furthermore, Fe does not readily form a hydride. Hence, from a simple reasoning we expect the destabilization effect of the interface to be increased. We find that for hydrogen absorption indeed the plateau pressures of Fe-sandwiched Mg are increased compared to TiH_2-sandwiched Mg. Now, however, there are two pressure plateaus instead of one. The desorption isotherms are, on the other hand, unaffected by the presence of Fe. Hence, this chapter investigates the origin of the double plateau and asymmetry in the sorption properties. We do so by relating the hydrogen sorption experiments to the structure and morphology of the Mg/Fe multilayers, as measured with X-ray diffraction (XRD), X-ray reflectometry (XRR) and Cross-Section Transmission Electron Microscopy (CS-TEM). Based on our analysis, we optimize the sample and show that MgH_2 can indeed be stabilized when it is interfaced with Fe.

This thesis shows that nanoconfined metal hydrides can indeed be destabilized through the interface energy. Chemical and mechanical interactions with the confining materials, however, have the unwanted effect of reducing the destabilization—something that must be taken into account when designing a hydrogen storage system based on nanoconfinement. Hence, a major, seemingly trivial, conclusion is that a proper treatment of all of these effects demands that both the hydrogen *ab*- and *de*sorption thermodynamics are investigated. From such a complete investigation, we find that control of the microstructural properties can optimize the destabilization effects.

Chapter 2

Interface energy controlled thermodynamics

2.1 Introduction

Compared to 700 bar gas cylinders which are currently used by most car manufacturers, hydrogen stored in metal hydrides offers the advantage of a much higher volumetric density.[10] A PEM fuel cell, however, needs to be provided in the order of 1 bar hydrogen pressure at temperatures around 60 to 85 ℃. An attractive storage material such as magnesium hydride is thermodynamically too stable and has to be heated to over 250 ℃ to obtain a 1 bar hydrogen desorption pressure. This means that, on the storage system level, high pressure storage remains superior in current hydrogen car concepts.[65]

In order to reduce the required heat to desorb hydrogen and increase the equilibrium desorption pressure, chemical destablization of MgH_2 can be achieved by alloying.[15] So far, the improved properties mainly reflect the enhanced (de-)sorption kinetics.[66, 67, 68, 69]

Physical destabilization of metal hydrides can in principle be achieved via two mechanisms: elastic clamping,[58] and interface energy.[70, 39, 71, 72] The latter effect can cause both destabilization and stabilization of the hydride phase at the nanoscale, depending on whether the difference in interface energy between the metal and hydride phase is positive or negative, respectively.

Until now, such an effect on the thermodynamics due to a change in interface energy accompanying a metal-metal hydride phase transformation has not been demonstrated experimentally, although it is expected to occur from theory.[73, 74, 41] While it is not trivial to directly relate the particle size to the thermodynamics of hydrogenation in nanoparticle systems, this relation can be probed by using thin films.

In this chapter we experimentally show for the first time that nanostructured MgH_2 is destabilized by interface energy effects using Mg thin films with varying and gra-

---

This chapter is based on: Lennard Mooij, Andrea Baldi, Christiaan Boelsma, Kun Shen, Marnix Wagemaker, Yevheniy Pivak, Herman Schreuders, Ronald Griessen and Bernard Dam, Advanced Energy Materials 1, 2011, 754-758 dient thicknesses (1.5 - 10 nm). The interface energy change we deduce from the thickness dependence of the equilibrium hydrogen pressure, is in excellent agreement with the one obtained from first principle calculations.

2.2 Experimental

Multilayer thin film preparation

Mg/Ti thin film multilayers are prepared using an ultra-high vacuum (UHV) multitarget sputter system (base pressure 10^{-7} Pa) in 3 μbar of Ar (6N). The multilayer stacks are deposited on rotating substrates, in order to obtain constant thicknesses of the individual layers. The substrates are 10 × 10 × 0.5 mm float glass. The Ti thickness is 5 nm, and the Mg layers have thicknesses ranging from 1.5 to 10 nm. As a catalyst/capping layer, 10 nm of Pd are deposited on top of the stack. Structural characterization showed well defined Mg/Ti interfaces, with the (0001) planes of both Mg and Ti oriented in parallel to the substrate.[56] Thin magnesium wedges are deposited on 70×5×0.5 mm UV-grade quartz substrates. A uniform layer of 10 nm Ti is deposited first by rotating the substrate. After this step, the rotation is stopped, and a Mg-wedge with a thickness ranging from 1.7 to 10 nm is deposited. Finally, uniform cap-layers of Ti (10 nm) and Pd (40 nm) are deposited for the samples measured below 373 K. For samples measured above that temperature, Pd is exchanged with a Ni cap layer (40 nm). The thickness of the wedges and uniform films is determined from by the sputter rate, provided by stylus profilometry (DEKTAK) recorded on thick layers (200 nm).

Hydrogenography

The hydrogenation thermodynamics and kinetics are characterized using hydrogenography.[48] The optical transmission of the samples is measured using a white light source and a 3CCD camera. Transmission data of the samples with uniform layers are averaged across the whole sample, while for the 7 cm long wedge samples the data was only averaged in the direction perpendicular to the thickness gradient. The hydrogen pressure is gradually varied between 4 and 1000 Pa. For this purpose gas mixtures of 0.1% H_2 in Ar and 4% H_2 in Ar are used. The gas flow is set to 20 sccm. Typically, the time taken for an absorption isotherm is 8.5 hours per order of magnitude in H_2-pressure, and in desorption 20 hours per order of magnitude in H_2-pressure. The pressure-steps are exponentially in- or decreasing, thus increasing the chemical potential of the gas linearly.

Computational Methods

The excess energy associated with the coherent interfaces is calculated using the plane wave basis VASP code, implementing the generalized gradient approximation (GGA). The relaxed dimensions of the slabs are typically around 40 Å in the direction perpendicular to the interface. In addition the ionic positions are relaxed leading to a total energy convergence below 10^{-6} eV for all calculations. To extract the interface energy without introducing elastic energy due to the imposed strain, which scales with the volume of the calculated slabs, the following procedure was performed. For the bulk cells the cell parameters in the plane of the interface were fixed to the value of the slabs, relaxing only the cell parameter perpendicular to the interface. In this way subtraction of the bulk cell energies from the interface slab energy guarantees that the elastic energy due to the imposed strain is subtracted and the excess (interface) energy of the interface is obtained.

2.3 Results and discussion

To measure the thermodynamics of hydrogenation in ultra-thin (1.5–10 nm) Mg films deposited between protective Ti layers we use Hydrogenography.[56] Upon hydrogenation, the metal-to-insulator transition from Mg to MgH_2 causes a marked increase in optical transmission at the equilibrium plateau pressure p_{eq}. The Pressure-Optical Transmission-Isotherms (PTIs) provide the same thermodynamic information as the typical Pressure-Composition-Isotherms (PCI) measured for bulk metal hydrides,[63] with the advantage of a much higher sensitivity. Well-defined plateaus can even be observed in Mg films as thin as 1.5 nm (∼6 atomic layers). Compared with a PCI, in a PTI the hydrogen concentration—plotted along the x-axis—is replaced by the normalized transmission $\ln(T/T_0)$, which is proportional to the hydrogen concentration in the two-phase (Mg-MgH_2) region. To obtain a thermodynamical description of the influence of the interface energy change upon hydrogenation of a Mg layer sandwiched between TiH_2, we use a classical approach. Upon the first exposure of a Ti/Mg/Ti stack to hydrogen, the Ti sandwich layers hydrogenate to form TiH_2. We assume a uniform hydrogenation of Mg according to:

$$Mg + H_2 \longleftrightarrow MgH_2 \tag{2.1}$$

with the corresponding equilibrium constant K:

$$-\ln K = \ln \frac{p_{H_2,bulk}}{p_0} = \frac{\Delta_r G^0}{RT} = \frac{\Delta_f G^0_{MgH_2}}{RT} \tag{2.2}$$

Here K is a function of $p_{H_2,bulk}$, the equilibrium hydrogen partial pressure in bulk Mg, p_0 the standard pressure (10^5 Pa), and $\Delta_r G^0$ the Gibbs free energy change of the

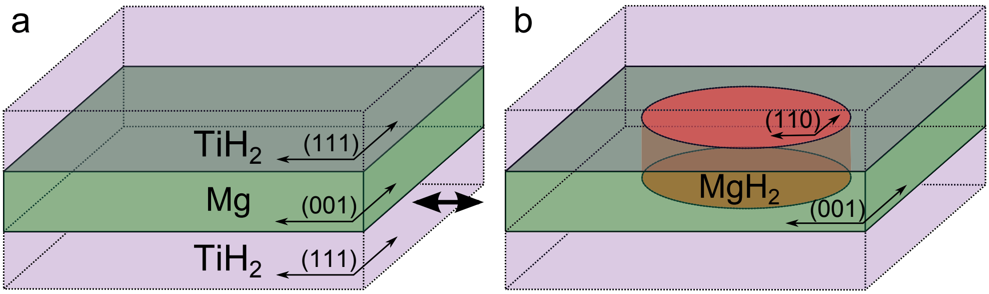

Figure 2.1 Scheme of the layer geometry and thin film crystal orientation. (a) After the first exposure to hydrogen, TiH_2 is formed textured with the (111) plane parallel to the substrate; (b) on further raising of the H_2 pressure MgH_2 nucleates as represented by the red cylinder . We assume that the MgH_2 (110)-plane is parallel to the substrate. After the initial hydrogenation, the multilayer is cycled between (a) and (b). Lattice expansions are not shown here for the sake of clarity.

reaction, which here is equal to $\Delta_f G^0_{MgH_2}$, the Gibbs free energy of formation. For nanosized Mg the interface energy contribution to the Gibbs free energy has to be taken into account:

$$\ln \frac{p_{nano}}{p_0} = \frac{\Delta_r G^0_{nano}}{RT} = \frac{1}{RT}\left[\Delta_f G^0_{MgH_2} + \sum_i \{A\gamma\}_{MgH_2|i} - \{A\gamma\}_{Mg|i}\right] \tag{2.3}$$

where p_{nano} is the equilibrium pressure of nanosized Mg, A the interfacial area per mole Mg, and γ the interface energy. Note that γ is a Gibbs free energy per unit of surface containing both an enthalpy and entropy term. The subscripts '$MgH_2|i$' and '$Mg|i$' describe the nature of the interface, where i can be either TiH_2 or Mg, depending on where a MgH_2 nucleus is formed. When combining Equations 2.2 and 2.3, only interface energy terms remain:

$$\ln \frac{p_{nano}}{p_{bulk}} = \frac{1}{RT}\left[\sum_i \{A\gamma\}_{MgH_2|i} - \{A\gamma\}_{Mg|i}\right] \tag{2.4}$$

In principle, the summation over all interface energy terms should take into account all crystal orientations. In the present work, the magnetron sputtered hexagonal Mg and Ti thin films grow highly textured, with the (002)-plane parallel to the substrate. Upon hydrogenation of Ti, textured fluorite TiH_2 is formed with the (111)-plane parallel to the substrate (Figure 2.1). Although no diffraction peak of MgH_2 could be seen for hydrogenated Mg layers < 20 nm, we assume the MgH_2 (110)-plane to be parallel to the substrate (Figure 1b), as is the case for hydrogenated 20 nm thick Mg.[56] Furthermore, we assume that the size of the critical nucleus of MgH_2 is larger than the Mg-layer width, thereby forming across the whole Mg layer width. Once these nuclei are formed Equation 2.4 simplifies to:

$$\ln\frac{p_{nano}}{p_{bulk}} = \frac{\{\gamma A\}_{MgH_2|TiH_2} - \{\gamma A\}_{Mg|TiH_2}}{RT} \tag{2.5}$$

In a recent work on similar samples, we showed by High Resolution Transmission Electron Microscopy (HRTEM) that the Mg/TiH_2 interfaces remain well-defined after loading and unloading with hydrogen. Furthermore the thin films expand only in the direction perpendicular to the substrate, resulting in a constant interface area.[56] Therefore:

$$A_{Mg|TiH_2} \approx A_{MgH_2|TiH_2} \approx A$$

and with $\gamma_{MgH_2|TiH_2} - \gamma_{Mg|TiH_2} = \Delta\gamma$, Equation 2.5 now becomes:

$$\ln\frac{p_{nano}}{p_{bulk}} = \frac{A}{RT}\Delta\gamma \tag{2.6}$$

Neglecting the small MgH_2/Mg interfacial area, the interface area per mole of thin film is proportional to the molar volume V of magnesium divided by its thickness d:

$$A = \frac{2V}{d} \tag{2.7}$$

The factor 2 accounts for the interfaces with TiH_2 on both sides of the Mg-layer. Equations 2.6 and 2.7 lead to an expression for the plateau pressure p_{eq} of a thin film with thickness d:

$$\ln\frac{p_{eq}(d)}{p_{bulk}} = \frac{2V}{RTd}\Delta\gamma \tag{2.8}$$

It is clear that a positive $\Delta\gamma$ results in a destabilization of the nanosized hydride phase with respect to the bulk hydride ($d = \infty$). From Equation 2.8 it follows that from the determination of p_{eq} for various thicknesses d, we can derive both $\Delta\gamma$ and p_{bulk}.

To determine p_{eq} as a function of d we deposited two different multi-layer stacks of Mg and Ti by magnetron sputtering on quartz and float glass substrate wafers. The first stack consists of 6 Mg layers, with thicknesses of 10, 7, 4, 3, 2 and 1.5 nm (six-layer sample), with every Mg layer surrounded by two 5 nm Ti thin films acting as spacers. The second stack has the same geometry but with only three Mg layers (three-layer sample) of 10, 5 and 2 nm (Figure 2.2a). On both types of stacks 10 nm of Pd are deposited as catalytic capping layer. After the initial loading, the hydrogenation of Mg is reversible, as the second and third absorption cycles perfectly overlap.

Figure 2.2b shows the absorption PTIs of the third cycle of the six- and three-layer samples measured at 333 K. Clearly, we observe different plateau pressures

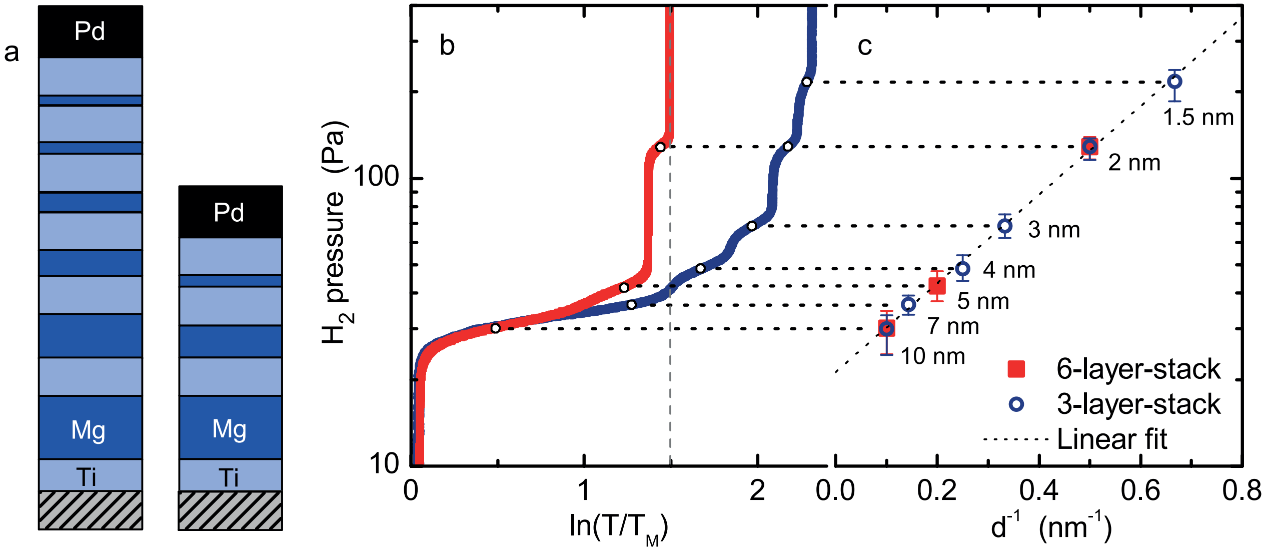

Figure 2.2 Hydrogen absorption isotherms and their plateau pressures versus inverse Mg layer thickness. (a) A schematic representation of the two Mg-Ti multilayer geometries, with (b) their absorption isotherms (cycle 3) taken at 333 K. In the six-layer sample (blue) layers of 10, 7, 4, 3, 2 and 1.5 nm Mg are interlaced by 5 nm Ti. The three-layer sample (red) consists of a stack in which Ti is alternated by 10, 5 and 2 nm thick Mg-layers. (c) From the equilibrium pressures versus the inverse thickness, the slope of the linear fit gives $\Delta\gamma = 0.35$ J·m^{-2} and the intercept $p_\infty = 20$ Pa. The error-bars indicate the pressure-span of the plateaus.

indicating several distinctive thermodynamic equilibria. From the Lambert-Beer law it follows that the width of the pressure plateau (the change in transmission when going from metallic Mg to insulating, transparent MgH_2) is directly proportional to the thickness of the corresponding Mg layer.[61] Hence, we conclude that the thicker Mg layers load first. We verified this by comparing the optical reflection from the substrate side to that from the top of the film.[58] By plotting the plateau pressure as a function of the inverse layer thickness d-1 (Figure 2.2c), we find a clear linear dependence in perfect agreement with the model described in Equations 2.1-2.8. Note that, while the 10 and 7 nm plateaus of the six-layer sample are hard to distinguish visually, their width exactly matches the plateau width of the completely hydrogenated three-layer sample (total thickness of 17 nm of Mg) (Figure 2.2b). Moreover, we find that the 10 and 2 nm Mg layers load at exactly the same pressure in both stacks. Hydrogen has to overcome kinetic barriers in the form of several layers of Mg and TiH_2 before the thickest Mg layers can hydrogenate. Despite these barriers, the thickest layers load first: A strong indication for the thermodynamic nature of the effect.

To judge the validity of our result, we also have to consider the desorption isotherm. The hysteretic behavior of most metal hydrides reflects the first order nature of the phase transition.[75] As the contribution of the interface energy to the hydrogenation energy should be the same on hydrogenation and dehydrogenation, the effect of interface energy is equivalent to a thermodynamical bias. Therefore, on desorption we expect to observe the same increase in pressure as a function of thickness. Since the desorption kinetics in the multilayer stack is too slow to measure, we prepared single- layer Mg-wedges, again sandwiched between two 10 nm Ti layers and capped by Pd. In this case, the wedge thickness ranges between 1.7 and 10 nm across the length of the 7 cm long quartz substrates (Figure 2.3a). With Hydrogenography, we measured the (de-)hydrogenation thermodynamics of 620 positions simultaneously. As a typical output we constructed an image where the y-axis represents the hydrogen pressure, and the x-axis the thickness of the film, in this case for the third H-absorption. The transition from dark to light reflects the change in optical transmission due to the transition from metallic Mg to insulating MgH_2, with the thick part of the wedge hydrogenating first. In this way we directly observe Mg thickness dependence of the plateau pressure.

Plotting the normalized transmission $\ln(T/T_M)$, the pressure-transmission-isotherms are constructed for a few thicknesses at 363 K (Figure 2.3b). The same procedure is followed to construct the desorption isotherms. In absorption we again observe well-defined plateaus for single Mg layers as thin as 2 nm. In desorption the plateaus of $d < 3$ nm have a visible slope, usually indicative of a kinetic limitation. However, the thicker MgH_2 layers do exhibit flat plateaus in desorption.

Because of the large amount of simultaneously recorded isotherms we determined p_{eq} in an automated fashion, using again the smallest slope in the isotherm

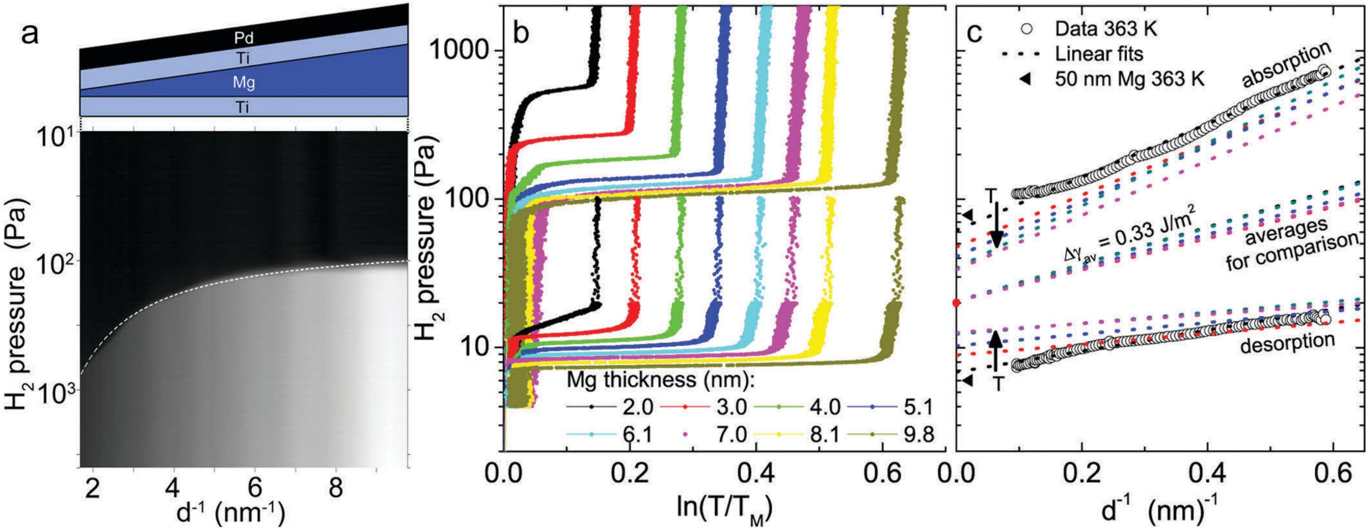

Figure 2.3 (a) Wedge layer geometry (top) with a thickness gradient of 1.7 to 9.8 nm (over 7 cm) in between two 10 nm Ti layers capped with Pd; with (bottom) its Hydrogenography image (T = 363 K). The change from black to white at a certain H_2 pressure measures the transition from metallic Mg to transparent MgH_2, which is clearly dependent on the Mg-thickness. The dashed white line is a 1/(Mg-layer thickness) function added as guide for the eye. (b) Selected ab- and desorption isotherms of the Mg wedge measured at 363 K. (c) Equilibrium pressures versus inverse layer thickness for various temperatures. For clarity we only show the data points for 363 K while for all other temperatures only the linear fits are shown (black = 363 K, red = 393 K, blue = 423 K, green = 453 K, pink = 473 K). The fits are normalized to the average equilibrium pressure at 363 K at $d^{-1} = 0$ nm^{-1}, indicated by the red dot. This normalization allows for the graphical comparison of the hysteresis and slopes, while making the pressure-axis to correspond only with the data measured at 363 K. Furthermore the data of a ‘thick’ 50 nm Mg film at 363 K are indicated by the black triangles.

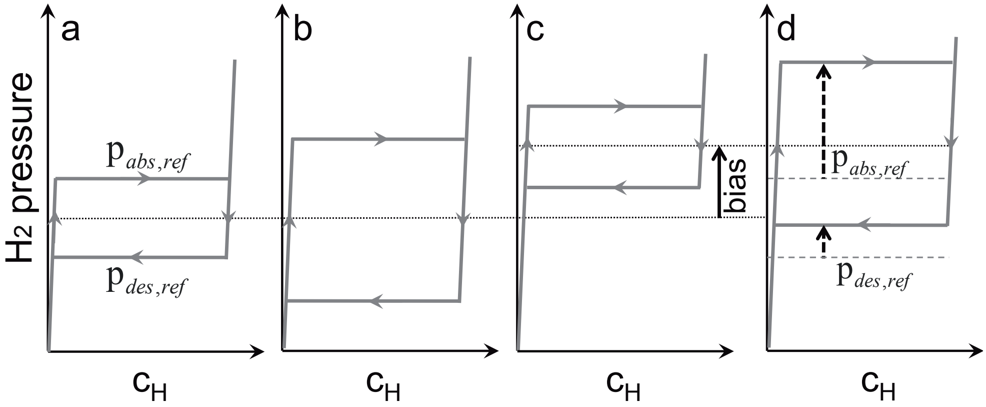

Figure 2.4 Behavior of the absorption/desorption hysteresis. (a) The unperturbed reference state, affected by (b) an additional hysteretic component, from *e.g.* plastic deformation energy, (c) a thermodynamic bias (solid arrow) from *e.g.* surface/interface energy, and (d) a combination of a thermodynamic bias and extra hysteretic component. Compared to the reference state, the increase in plateau pressure of absorption is larger than that of desorption (dashed lines). Due to the symmetry of the process, the average of the absorption and desorption plateau pressures compared to the reference state is the thermodynamical bias, as in (c).

as the definition for the equilibrium pressure. As shown in Figure 2.3c the plateau pressure increases both in absorption and desorption with decreasing d. However, this slope is found to be larger in absorption ($\Delta\gamma_{abs} = 0.44$ Jm^{-2}) than in desorption ($\Delta\gamma_{des} = 0.17$ Jm^{-2}). Recorded isotherms of several single, uniform Mg layers between TiH_2 show the same slopes of p_{eq} versus d^{-1}. This behavior is not expected since the interface energy should act similarly on both branches of the hysteresis (Figure 2.4a and b). A widening is expected only when additional energy is brought into the system, for instance due to plastic deformation (Figure 2.4c).[61] Isotherms measured at 393 K, 423 K, 453 K, and 473 K reveal that the hysteresis decreases with increasing temperature, as can be seen by comparing the normalized linear fits of the equilibrium pressures at various temperatures (dotted lines in Figure 2.3c). It is therefore likely that the creation and removal of defects—a thermally activated process needed to induce plastic deformation—is the cause of the additional hysteretic component. Since out-of-plane expansion upon hydrogenation equals the theoretical bulk volumetric expansion of ~30% [56], the amount of residual strain between hydrogenated Mg and TiH_2 is negligible.

Hence we deduce that the equilibrium pressure is the sum of both an interface energy related thermodynamic bias and an additional hysteretic component induced by plastic deformations (Figure 2.4d). The linearly increasing size of the hysteretic component with d^{-1} indicates that the amount of plastic deformations is proportional to the surface area, thus remaining the same for all thicknesses. This points at the formation of misfit dislocations upon hydrogenation at the interface[62] to accommodate the misfit between MgH_2 and TiH_2. As the amount of misfit dislocations formed per unit volume of Mg increases with d^{-1}, so will the energy per unit volume of Mg required to form these misfit dislocations increase with d^{-1}. Because of the symmetry of the process, we can now separate the interface energy from the plastic deformation. Only the average of the two slopes of $p_{eq,abs}$ and $p_{eq,des}$ versus d^{-1} of Figure 2.3c provides the thermodynamical bias (Equation 2.8). From this average we deduce an interface energy difference of $\Delta\gamma = 0.33 \pm 0.01$ Jm^{-2}.

This destabilization comes at a cost as the presence of TiH_2 lowers the reversible hydrogen content of the system. For a 2 nm Ti/5 nm Mg/2nm Ti stack, the hydrogen weigth density is reduced to 3%. We do not expect the hydrogen content of the MgH_2 layers to be affected since the optical contrast scales linearly with the Mg thickness.

Finally, we compare our experimental results with calculations based on first principles. Theoretical calculations on Mg-nanoparticles in vacuum have revealed a destabilization of MgH_2 at the nanoscale due to an increase in surface energy on hydrogenation.[41] Furthermore, recent calculations revealed the stabilization of fluorite MgH_2 compared to rutile MgH_2 with decreasing thickness.[76] SAED patterns showed no presence of the fluorite phase in Mg (4 nm) / Ti (2 nm) multilayers.[56] We calculated the difference in excess energy associated with coherent interfaces without introducing elastic energy of periodic regions of TiH_2 (111) and MgH_2 (110), as compared with those of TiH_2(111)-Mg(001) using the plane wave basis VASP code, implementing the generalized gradient approximation (GGA). The resulting interface energies of these calculations are $\gamma_{TiH_2|MgH_2} = 0.196$ eVÅ^{-2} and $\gamma_{TiH_2|Mg} = 0.163$ eVÅ^{-2}, leading to a difference $\Delta\gamma^{calc} = \gamma_{TiH_2|MgH_2} - \gamma_{TiH_2|Mg} = 0.033$ eVÅ^{-2} $= 0.53$ Jm^{-2}. This value, calculated for perfectly coherent and flat interfaces, is in excellent agreement with the one determined experimentally on ultrathin Mg layers.

2.4 Conclusion

We have experimentally shown for the first time the possibility to tailor the thermodynamics of a metal-hydrogen system by means of the interface energy. Using thin films as a model system, we find an energy difference of ∼0.3 Jm^{-2} between the MgH_2(110)—TiH_2(111) and Mg(001)—TiH_2(111) interface. Assuming an isotropic interface energy this implies that embedded MgH_2 nanoparticles with a radius of ∼1.8 nm would experience an order of magnitude increase in equilibrium pressure at 393 K compared to bulk Mg. Hence, this effect is expected to play a role in for example melt-infiltrated nano-materials (*e.g.* Ref. [72]). Depending on the nature of the interaction of the matrix with the metal hydride an even stronger destabilization is possible. To verify the thermodynamic nature of such an effect, it is essential to measure both branches of the hysteresis in order to rule out the effect of plastic deformations. Thus, the use of thin film multilayers in combination with Hydrogenography provides a powerful platform to explore interface and confinement effects metal hydride storage materials.

Chapter 3

Hysteresis: The role of nucleation and growth

3.1 Introduction

Metal hydrides are capable of storing hydrogen at higher mass and volume densities than high pressure gas cylinders and liquid hydrogen.[9] Many light-weight metal hydrides are, however, very stable and require heat to release the stored hydrogen. The proton exchange membrane (PEM) fuel cells that will be used in vehicles, have an operating temperature between 60 and 80 °C. In this case, the waste heat is not large enough to release hydrogen from for instance MgH_2—a high weight-capacity (7.6 wt%) metal hydride that releases hydrogen at 1 bar around 300 °C. Hence, the search continues for a light-weight, compact metal hydride material with a suitable hydrogen release temperature at a reasonable pressure (around 1 bar).

One way to find a suitable metal hydride is to thermodynamically destabilize a known metal hydride. This can for instance be done through nanostructuring.[33, 41, 74] The increased surface (or interface) area per unit volume destabilizes the hydride phase, if the surface (or interface) energy of the hydride phase is higher than that of the metal phase.

In addition, nanosized and nanoconfined metal hydrides show improved kinetics, [39, 40, 77, 78, 79, 80] as well as different reaction pathways compared to the bulk materials.[34] This suggests that nucleation and growth processes are affected by the nanoscale. Recently, for instance, a beneficial effect due to added TiF_3 on the kinetics of MgH_2 nanoparticles has been ascribed to easier nucleation of the MgH_2 phase.[81]

For the physically similar Li-intercalation materials, calculations by Wagemaker *et al.*[82] and Malik *et al.*[83] have recently shown that the unexpectedly small hysteresis gap of nanosized Li_xFePO_4 might be due to the presence of a single phase, low energy pathway from Li-poor to Li-rich Li_xFePO_4. The nucleation of the Li-rich

---

This chapter is based on: Lennard Mooij and Bernard Dam, Phys. Chem. Chem. Phys. 15, 2013, 2782 phase can in this case be avoided, which explains the exceptionally fast kinetics of this battery electrode system.

In chapter 2, we found that thin layers of MgH_2 can be destabilized compared to bulk when made sufficiently thin (< 10 nm) and sandwiched between two TiH_2 layers.[84] From the average of the absorption and desorption pressure as a function of the Mg layer thickness, we derived an interface energy difference between hydride and metal phase of $0.33\ ^{\mathrm{J}}\!/_{\mathrm{m}^2}$. Because this interface energy difference acts as a thermodynamic bias, the width of the hysteresis should be unaffected by this energy term. We observed, however, that the hysteresis increases with decreasing Mg thickness, thus the desired increase of the desorption pressure is less than expected.

The interface energy model we used to understand the thickness dependence of hydrogenation pressure, implies that the nucleation of the magnesium hydride phase should occur across the whole Mg layer width, followed by a lateral outgrowth of these nuclei. Thereby the Mg/TiH_2 interface is exchanged with a MgH_2/TiH_2 interface. The opposite should hold for the desorption process. This model is in contrast with what has been deduced previously for Pd-capped Mg thin films. In that case, MgH_2 formation occurred preferentially at the Mg/Pd interfaces, thus creating a layered Mg/MgH_2 structure.[85] Since hydrogen diffusivity in MgH_2 is extremely low, this observation explaines why thick Pd/Mg films are usually difficult to fully hydrogenate.

In general, especially at low temperatures, we expect nucleation and growth to often play an important role in the hydrogenation process.

Hence, in this chapter we investigate the effect of nucleation and growth processes on the hydrogenation of thin Mg layers in relation to the behavior of the hysteresis. We do so through hysteresis scans using Hydrogenography [47], an optical technique that relies on the change in optical properties that characterizes many metal-to-metal hydride transitions such as in Magnesium. It allows us to detect the ab- and desorption pressure plateaus, $\overrightarrow{p}$ and $\overleftarrow{p}$ respectively, as is shown in Fig. 3.1.

The two pressures $\overrightarrow{p}$ and $\overleftarrow{p}$ define the hysteresis. In case the nucleation of the hydride or metal phase requires an additional driving force to proceed, this will affect the ab- and desorption pressure. During hydrogen absorption, the increased driving force would result in a higher pressure plateau, while in desorption the pressure plateau would be lowered. Thus, the measured (apparent) hysteresis would be larger. Using hysteresis scans, we investigate the relation between the hysteresis and the nucleation barrier. In principle, a single hysteresis scan (in red in Fig. 3.1, for instance from **a** to **b**) is by itself sufficient to detect the ab- and desorption plateau pressures and hence the size of the hysteresis.[86] If indeed a higher hydrogen pressure is required to initiate the nucleation, a hysteresis scan from for instance **a** to **b** would not return again to **a**. It would instead return to for example point **c**, at a lower

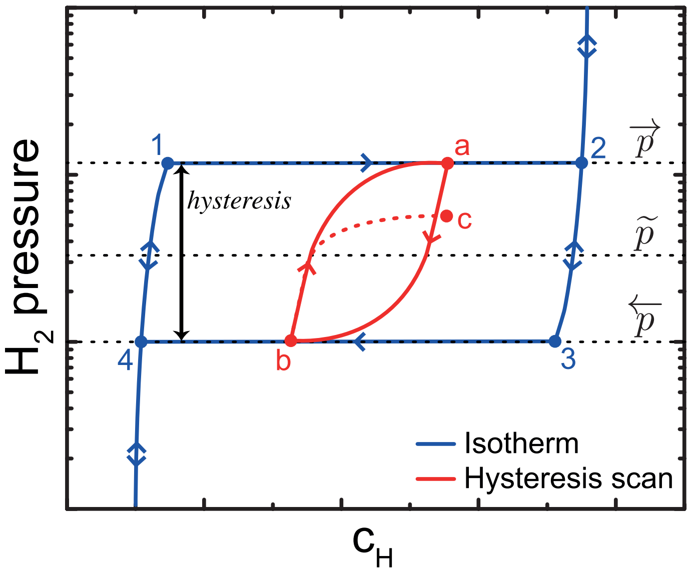

Figure 3.1 Example isotherm showing hysteresis. The absorption pressure plateau ($\overrightarrow{p}$) and desorption pressure plateau ($\overleftarrow{p}$) describe the hysteresis. A hysteresis scan is initiated within the pressure plateau at point **a**, and reaches the desorption pressure plateau at point **b**. Hence a hysteresis scan describes the hysteresis completely. If, for example, an increased driving force (*i.e.* higher hydrogen pressure) is needed to initiate the absorption of hydrogen, the measured value for $\overrightarrow{p}$ is too high, and the hysteresis scan will return to, for example, point **c** instead of **a**.

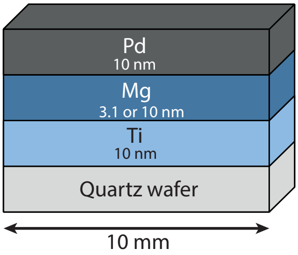

Figure 3.2 As deposited sample layout. The Mg layer thickness is either 3.1 or 10 nm.

hydrogen pressure.

The nature of our experimental technique requires the use of a multilayer model system. With hysteresis scans, we observe proof for the importance of nucleation of the metal hydride on the size of the hysteresis in a 10 nm Mg layer sandwiched between two Ti layers.

Because the nucleation process acts as a kinetical barrier, waiting for a very long time without increasing the driving force should also result in the transformation to the hydride phase to occur. By such long-term experiments, we directly observe the nucleation and subsequent growth of the magnesium hydride phase in the same 10 nm Mg layers.

The outcome of our experiments furthermore shows the importance of taking into account the role of plastic deformation in the nucleation and growth of metal hydrides. It is therefore relevant for metal-to-metalhydride and other phase transitions with an accompanying large volume change (*e.g.* Li-intercalation materials).

3.2 Experimental

Multilayers of 10 nm Ti, 3.1 or 10 nm Mg, 10 nm Ti and 10 nm Pd (Fig. 3.2) are deposited on 10x10 mm quartz wafer substrates by magnetron sputter deposition. The ultrahigh vacuum chamber has a base pressure of 10^{-9} mbar (AJA Int.). Sputter rates are typically 0.08 $\mathrm{nm/s}$ for Ti (200 W DC), 0.23 $\mathrm{nm/s}$ for Mg (150 W RF) and 0.12 $\mathrm{nm/s}$ for Pd (50 W DC).

The change in optical transmission of the multilayer sample is recorded as a function of hydrogen pressure at constant temperature (here 90 °C) with Hydrogenography. Hence with this technique we measure Pressure-Transmission-Isotherms (PTI's). The change in transmission is related to the change in hydrogen concentration, which means that a PTI provides similar data as a Pressure-Composition-Isotherm. In fact, for a perfect mixture and within the two-phase plateau region, the optical transmission ($\ln({}^{T}\!/_{T_0})$) is proportional to the fraction of the metal hydride

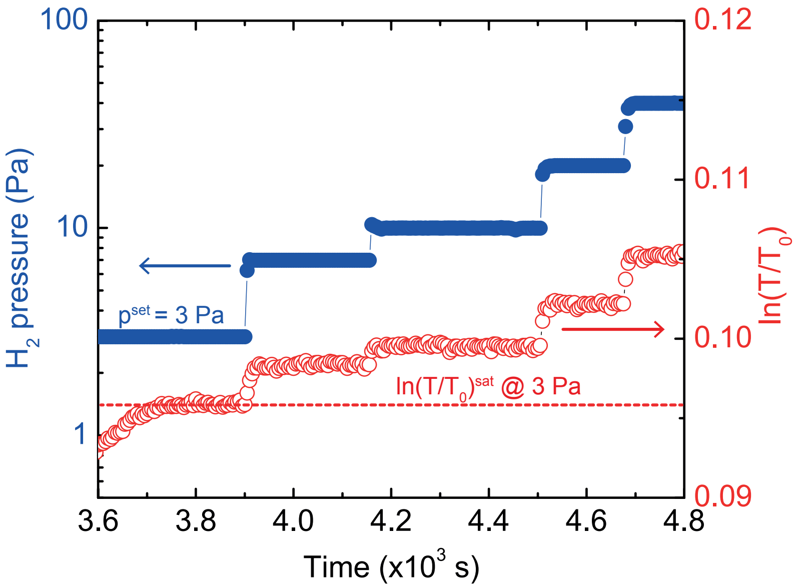

Figure 3.3 Upon changing the hydrogen pressure (left axis, blue), the dynamical response in the transmission (right axis, red) is recorded. When the transmission saturates at a certain pressure, such value is said to be in equilibrium.

phase formed.

To measure a PTI, we place multiple samples in a stainless steel hydrogenation cell, which in turn is placed in a furnace. Both cell and furnace have windows to allow light to pass through the thin films. The transmitted light—which comes from a 150 W quartz-tungsten-halogen lamp—is recorded either with a 3-CCD camera or a Canon EOS 550-D.

With the 3-CCD camera we record the average transmission of the samples every 5 seconds. After a change in hydrogen pressure is applied, we monitor the dynamics of the hydrogen sorption (Fig. 3.3). When the optical transmission—$\ln\left({}^{T}/_{T_0}\right)$, with T_0 the transmission at t = 0—reaches a constant value, quasi-equilibrium is reached. Thus, we obtain one datapoint of a PTI. To measure a full ab- or desorption PTI, we incrementally increase or decrease the hydrogen pressure ($10^2 < p < 10^6$ Pa).

To study the hysteresis in more detail, we measure sub-hysteresis cycles, or hysteresis scans.[86] The same experimental method is followed as for a normal PTI, except that the direction of the pressure steps (up or down) is reversed at a certain point. To indicate the direction of the scan, a hysteresis scan that is started at an absorption plateau pressure is called a desorption scan. Similarly a scan that is started from a desorption plateau upwards in pressure is termed an absorption scan. Some data points are indicated in the isotherm although a steady-state transmission value (hydrogen concentration) has not been reached, *e.g.* at the start of an hysteresis scan the ab- or desorption process will not have reached a steady-state. Such data points are denoted with an asterisk (*).

With the aid of the Canon EOS 550-D, we investigate hydrogenation processes by a second method: we record a visual image of the sample on hydrogenation every ten minutes for up to two weeks, while a constant hydrogen pressure (which lies within the hysteresis) is applied. Depending on the pressure and Mg thickness, we observe the formation of small hydride domains and observe the time-dependence of the expansion of these nuclei at a resolution of 20 $^{\mu\text{m}}\!/_{\text{pixel}}$.

3.3 Results

3.3.1 Hysteresis scans of thin Mg layers

We measure the hysteresis on Mg/Ti multilayer samples, having a Mg layer thickness of either 3.1 nm or 10 nm. Characterization of such Mg/Ti multilayers by X-ray diffraction and X-ray reflectometry showed that the Mg is textured with the hcp (001) plane parallel to the substrate. Upon hydrogenation, rutile MgH_2 is formed with the (110) surface parallel to the substrate.[63, 56] The fact that the hcp-(001) plane is parallel to the rutile (110) plane is no coincidence: a topotactic transformation is part of the reason that the 30% volume expansion can be accommodated by a 30% thickness expansion.[87] This anisotropic hydrogenation mechanism is due to the clamping of the film by the substrate, which makes an in-plane expansion impossible.

The hydrogenation of the (001) textured hcp-Ti layers exhibits a similar hydrogenation process with the fluorite TiH_2-(111) plane oriented parallel to the substrate.

The Pd layer serves as a catalytic layer for the dissociation of H_2 and protects the underlying layers against oxidation. In all our experiments the hydrogen pressure is kept low enough to prevent the transition of the (111) textured fcc Pd layer to the $PdH_{0.6}$ phase.

10 nm Mg layers

Upon the first low pressure (< 1 Pa H_2) exposure to hydrogen, the Ti 10 nm / Mg 10 nm / Ti 10 nm / Pd 10 nm multilayer first absorbs hydrogen to form TiH_2 ($\Delta_f H^0 = -130$ kJ/mol H_2). This causes a slight decrease in optical transmission to negative values of $\ln\left({}^{T}\!/_{T_0}\right)$ (not shown here). Thereafter, still at low hydrogen pressures, the optical transmission increases to a typical value of 0.1. This is most likely because defects—located at the interface between the Mg and Ti layers—hydrogenate.[88] Previously it was found that this initial change in optical contrast scales with the amount of Mg/Ti interfaces.[56] Because hydrogen is stable in TiH_2 and at defects,

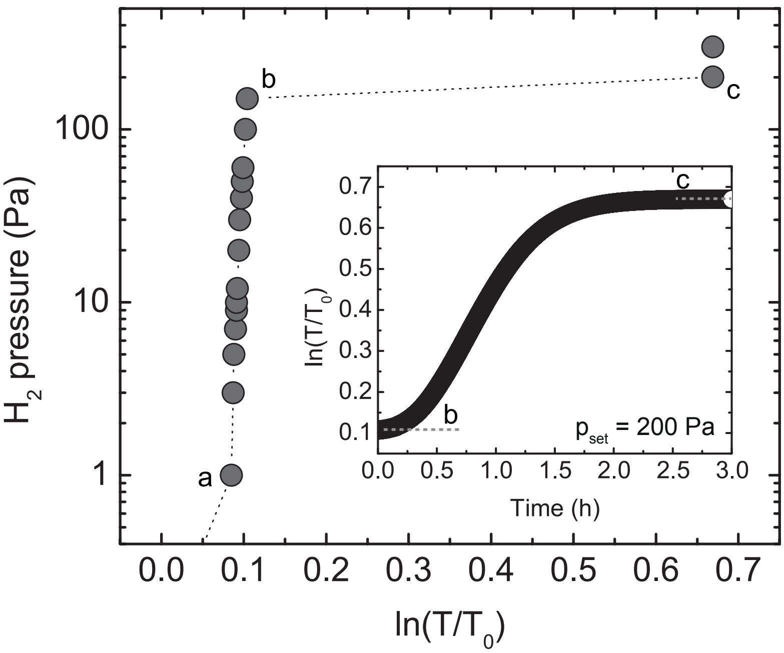

Figure 3.4 Hydrogenation isotherm (90 °C) constructed from equilibrium data of the first hydrogenation of a 10 nm Mg layer sandwiched between Ti. The inset shows the change in transmission versus time between points **b** and **c** from the moment the hydrogen pressure is set to 200 Pa.

subsequent hydrogenation cycles return to this state of initial hydrogenation with $\ln(T/T_0) \approx 0.1$.

Figure 3.4 shows the quasi-equilibrium data of the first hydrogenation cycle recorded at 90 °C. Each data point represents the saturation value of the optical transmission after applying a pressure step (as in Fig. 3.3). The optical transmission does not change much between points **a** and **b** and the saturation value is obtained within 10 minutes. In this pressure range, hydrogen dissolves in α-Pd, TiH$_2$, and α-Mg. A subsequent increase in hydrogen pressure to 200 Pa is enough to start the hydrogenation process of Mg. Here, as well as in subsequent cycles, we find that once the hydrogenation process starts, it continues until the Mg is fully converted to MgH$_2$. Thus, after the hydrogenation of Mg is complete, we reach the point **c** in the graph. This is elucidated by the inset of Fig. 3.4, which shows the dynamical data that were recorded when going from point **b** to **c**, with the pressure-increase at time zero. The S-shape curve shows that the hydrogenation of Mg is indeed one single process. Therefore, there are no points within the plateau of the PTI: only the last point before the transition (**a**) and the first point after the transition (**c**) are indicated in the

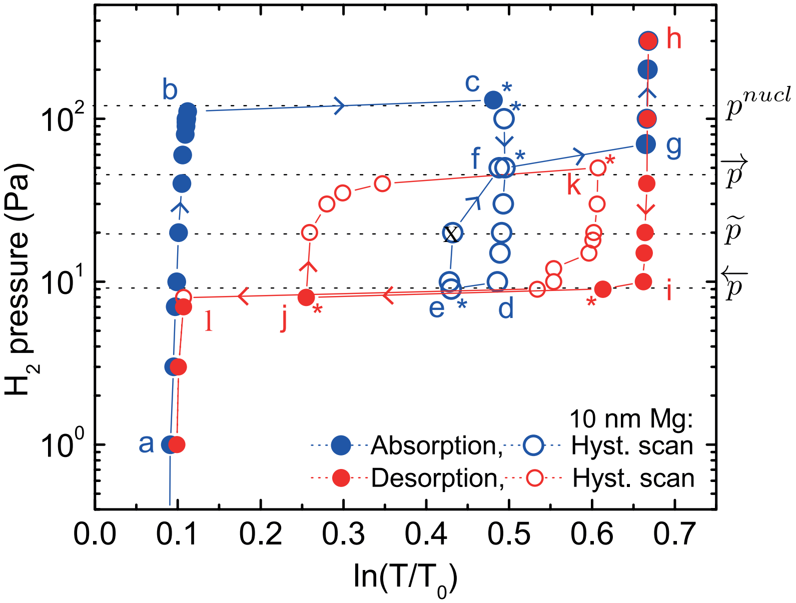

Figure 3.5 Sub-hysteresis isotherm (90 °C) constructed from equilibrium data of the second hydrogenation of a 10 nm Mg layer sandwiched between Ti. Data points marked by an * are the non-saturated, final values for $\ln\left({}^{T}\!/_{T_0}\right)$ at the set pressure just before the hydrogen pressure is changed. The gray area indicates the total apparent hysteresis from the path followed if the sample is completely hydrogenated and dehydrogenated. The slight increase in contrast occurring from point **a** to **b** we ascribe to the solid solution of hydrogen in α-Pd.

isotherm.

To analyse the nature of the hysteresis, in the second hydrogenation cycle we perform two hysteresis scans; one during hydrogen absorption (Fig. 3.5, blue data) and one during desorption (red data). The hysteresis scan data are indicated by open symbols, while 'normal' data have closed symbols.

We first focus on the absorption branche, shown in blue. Again we start at the dehydrogenated, metallic state (point **a**, p = 1 Pa) from where we increase the hydrogen pressure incrementally up to 120 Pa (point **b**). Similar to cycle 1, between points **a** and **b** there is little change in optical transmission and the typical waiting time for the transmission to saturate is 10 minutes. From previous experiments, we know that after the first cycle, a reproducible hydrogenation is obtained at slightly lower pressures in subsequent cycles.[84] Accordingly, in this second cycle a small increase of the pressure to 130 Pa already initiates the hydrogenation of Mg.

In order to start the desorption scan, the absorption process is not allowed to be completed. After 2.7 hours we stop the hydrogenation process at point **c**, where the 66% of the sample is hydrogenated. At this point, the pressure is lowered in small steps (**c** to **d**). The first of the points between **c** and **d** are marked by an asterisk (*) to indicate that the transmission still increases even though the pressure is lower than the 130 Pa needed to start the hydrogenation. In the following data points only a small decrease in optical transmission is observed. Only when reaching a hydrogen pressure of 9 Pa at point **d**, a decrease in transmission indicates that the MgH_2 dehydrogenates back to Mg.

We stop the dehydrogenation process, however, at point **e** where we incrementally increase the pressure again. Surprisingly, at 50 Pa, the sample reverts back to the 66% of the full loading reached before (point **f**, $\Delta t = 0.5$ h). This pressure is almost half an order of magnitude lower than the pressure required for the initial loading (point **c**). A further increase of the pressure to 70 Pa provides sufficient driving force to achieve a 100% hydrogenation of the sample (point **g**, $\Delta t = 11$ h).

From this experiment we learn that the Mg layer can be hydrogenated at a much lower pressure (50-70 Pa) than expected (130 Pa). Consequently, in a normal loading experiment the metallic Mg is supersaturated with hydrogen when the hydride phase forms. We propose that this is caused by a nucleation barrier: To nucleate small MgH_2 domains an energy barrier has to be overcome since the hydride phase has a 30% larger volume than Mg and has a different crystal structure; furthermore the TiH_2 and Pd layers will have to be pushed up and bent. In section Section 3.3.2 we will show proof for the existence of a nucleation and growth mechanism.

The reduced hysteresis is only observed with respect to the absorption branch of the hysteresis. This is evident from the absorption scan started on a desorption isotherm. Starting in the fully hydrogenated state at point h (red data in Fig. 3.5) we lower the hydrogen pressure until point **i** (10 Pa) we find that desorption starts when lowering the pressure to 9 Pa. The desorption pressure is equivalent to the pressure found in previous, continuous dehydrogenation experiments. To increase the speed of dehydrogenation, we decrease the pressure to 8 Pa at the asterisk mark *.

Upon reaching point **j**, we stop the desorption process and begin the absorption scan (shown as open symbols) with a first step to 20 Pa. Hereafter, the transmission begins to increase again, indicating the onset of the hydrogenation process. When the pressure is again slightly higher than the plateau pressure, 50 Pa, the absorption can continue. This non-linear behavior is typical for hysteretic systems and represents the irreversible nature of the transformation that is accompanied by hysteresis.[89]

At point **k** the hysteresis scan direction is again reversed by slowly decreasing the pressure back to the desorption plateau pressure. The transformation to metallic Mg is completed at point **l** (8 Pa). The hysteresis scan shows a 180° point symmetry around the point marked with X. It lies at the average pressure of the plateau pressures in absorption ($\overrightarrow{p}$) and desorption ($\overleftarrow{p}$). This average pressure $\widetilde{p}$ we estimate to be 20 Pa, which according to Flanagan *et al.*[89] must be the equilibrium pressure, especially given the symmetry around it.

3 nm Mg layers

Thin 3.1 nm Mg layers show a different behavior than the 10 nm layers. In accordance with our previous studies, we find that the hydrogenation pressure is higher than in thicker films. However, in this case, we did not find conditions to make a transformation to the hydride phase possible at pressures lower than the pressure needed to initiate the hydrogenation. This becomes clear from Fig. 3.6, where the blue data again represent the absorption measurement and the red data the desorption measurement.

Let us first focus on the absorption data in blue. The closed data symbols represent the hydrogenation up to 66% of the Mg (point **a** to **b**, p = 250 Pa, $\Delta t = 3.1$ h), which is followed by an instant lowering in pressure to 50 Pa (**b** to **c**). From point **c**, the pressure is again increased (open symbols). No large increase in transmission is observed until again reaching point **b**, where the hydrogenation continues and is completed at point **d**.

To perform an absorption scan during the desorption isotherm, we start in the fully hydrogenated state (point **e**). We lower the pressure stepwise and find that the desorption starts at point **f** ($p = 12$ Pa). To speed up the desorption, we further decrease the pressure to 8 Pa. Before reaching the fully desorped state, we initiate the hysteresis scan at point **g** by increasing the hydrogen pressure (open symbols), finally reaching point **h**.

Although we stop the hysteresis scan at **h**, from a rough extrapolation we see that the rehydrogenation would complete at the full loading—as indicated by the dashed red line. Such behavior is known as Return Point Memory (RPM), and is observed for many transitions that show hysteresis.[90] Here the full loading is the memorized return point, because it is the point up to where the sample was previously hydrogenated. After we reach point **h**, we again decrease the pressure and thereby return to the (memorized) starting point of the hysteresis-scan: point **g**.

Again we observe a 180° point symmetry around the point marked X, at the average pressure of the absorption and desorption plateau pressures, $\overrightarrow{p}$ and $\overleftarrow{p}$ respectively. In this way, we find an equilibrium pressure $\widetilde{p}$ of 47 Pa.

In summary, contrary to the 10 nm layers, the 3 nm layers do not show any hydrogenation at lower pressures than the pressure needed for the hydrogenation process to initialize.

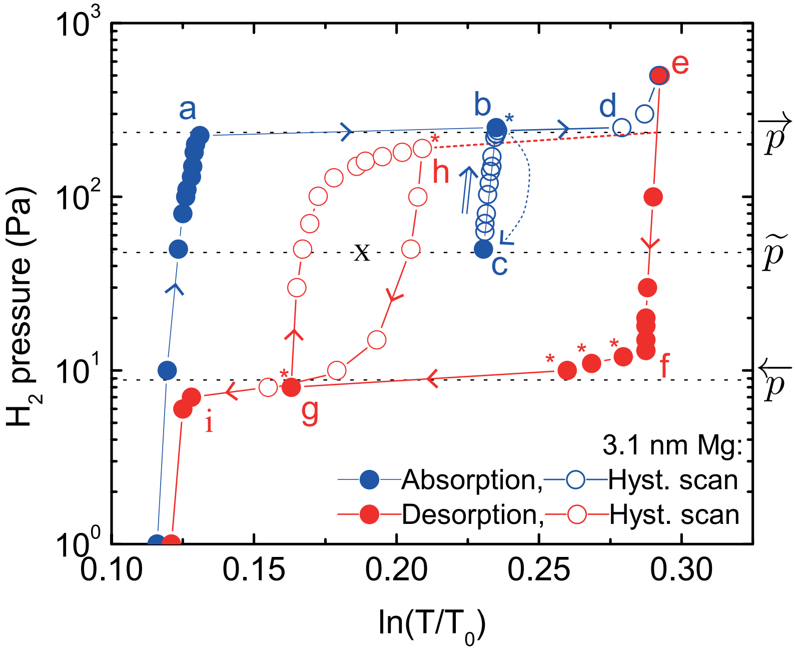

Figure 3.6 Absorption (blue) and desorption (red) isotherms (90 °C) from quasi-equilibrium data of the second hydrogenation of 3 nm Mg. Closed symbols represent the partial (de-)hydrogenation from a fully (de-)hydrogenated state. with the final point (C) representing the lowest final pressure reached. Open symbols continue from this final state and show the completion of the (re-)load cycle. The slight increase in contrast occurring up to point **a** we ascribe to the solid solution of hydrogen in α-Pd.

3.3.2 Long time, low pressure hydrogenation: 2D-growth of the hydride phase

To verify the presence of a nucleation barrier during hydrogen absorption, we set out to observe the nucleation and subsequent growth of MgH_2 in the 10 nm Mg sample. For this purpose we apply a constant pressure and observe the sample for an extensive period of time. We choose a pressure between p^{nucl}—where the oversaturation is high enough for the hydride phase to form (130 Pa)—and the absorption plateau pressure $\overrightarrow{p}$, which from the hysteresis scans we estimate to be $\backsim 50$ Pa. The idea is that the nucleation barrier can be overcome by the driving force—which we have already measured via the hysteresis scans—or by time: while applying a pressure slightly above $\overrightarrow{p}$ we observe the sample for a very long time. If one waits long enough, a MgH_2 nucleus should form somewhere within the Mg layer.

Hence, the experiment is performed as follows. We start at very low hydrogen pressure ($<$ 1 Pa) and then instantly change the pressure to 70 Pa. After a long waiting time, we find that the Mg layers can be hydrogenated at this pressure, which is well below the previously determined onset pressure of 130 Pa. Figure 3.7 shows a selection of unedited images taken every 10 minutes of a 10 nm Mg sample (10x10 mm, visible area 9x9 mm). After approximately 6.5 hours, islands with a high transmission are observed, which represent the formation of MgH_2 nuclei (Fig. 3.7, inside the white dashed circles). In time, these MgH_2 islands grow radially outwards, without a change in optical transmission of the islands. Thus, we conclude that MgH_2 islands form through nucleation, and then expand laterally.

The slow nucleation rate suggests that the associated nucleation barrier is large. Also the amount of nucleation sites is exceptionally low. Furthermore, on subsequent cycles the MgH_2 nuclei form at identical locations. This suggests the presence of preferential nucleation sites such as lattice defects or contaminating phases. At such sites the activation barrier for nucleation is reduced with respect to the pure lattice.

By following the outgrowth of the MgH_2 islands in time (movie online)†, we deduce the radial growth velocity from the domain edge position (Fig. 3.8). The red line in the inset indicates the direction along which we measured the expansion of the island. The edge position is determined at half the intensity difference between low intensity (Mg) and high intensity (MgH_2). The slope of the nucleus edge position versus time gives a constant growth velocity (2.9 nm/s for this spot). By averaging the front velocities of six hydride domains we find an average front velocity of 2.8 nm/s at a hydrogen pressure of 70 Pa and at 90 °C.

Remarkably, when two domains approach each other, bridges suddenly form (Fig. 3.9). These avalanche events occur at irregular distances and can not always be observed. From their occurrance we deduce that there is some long-distance interaction between the islands. Note that hydrogen may enter the edge of the nuclei simply through the Pd/TiH_2 layer, a path that is orders of magnitudes smaller than

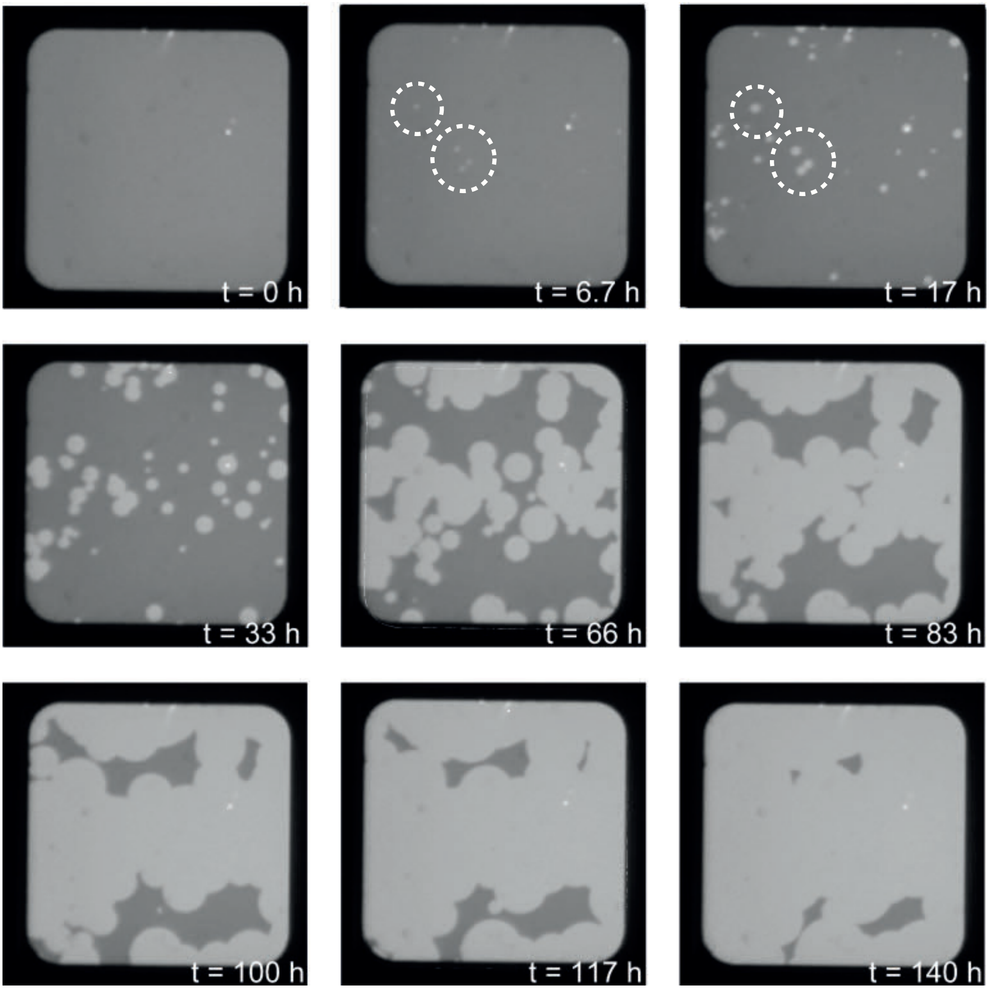

Figure 3.7 Sample hydrogenation at several times during a full hydrogenation cycle. The sample is 10x10mm in size (visible area 9x9 mm) and the conditions are $p_{H_2} = 70\ \mathrm{Pa}$ and 90 °C. After 6.7 h (top, middle) the first nuclei can be seen in the center of the sample, as indicated by the white dashed circles. After that more nuclei are formed. All grow radially outward at constant speed until the sample is completely hydrogenated.

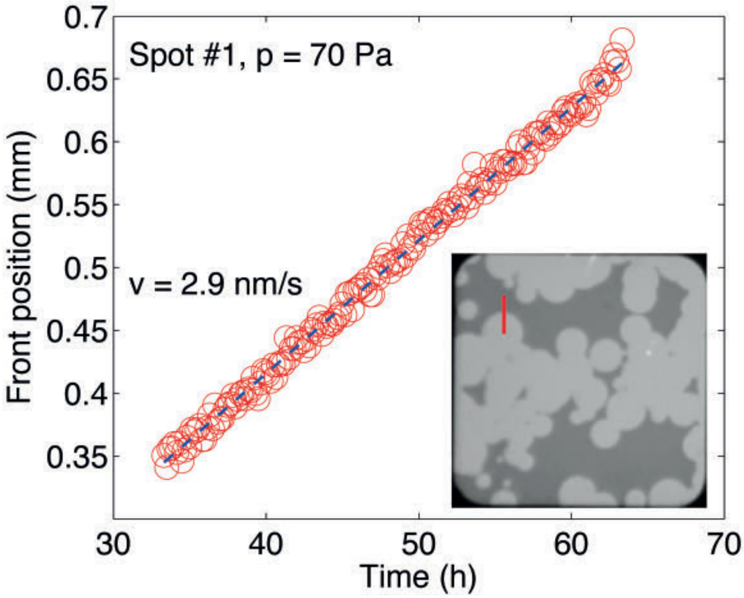

Figure 3.8 The domain edge position along the red line in the inset ($t = 33\ \mathrm{h}$, visible sample area 9x9 mm) of the hydride domain as a function of time. The slope of the edge position versus time gives the front velocity. The edge positions are extrapolated from the linescans at different time steps by fitting with a Fermi function (with the minimum and maximum being fit parameters instead of 0 and 1).

the observable distance between the islands (Fig. 3.10).

Desorption

Also, in the nucleation experiments we find that the desorption differs markedly from the absorption process. Even at very long measurement times, no nucleation and 2D-growth of the metal phase is observed in a fully hydrogenated sample. Neither do we observe a shrinkage of the 2D-nuclei when we switch from absorption to desorption. Instead, the optical transmission decreases gradually across the whole sample, which indicates that the MgH_2 phase desorbs hydrogen uniformly.

Remarkably, after desorbing all hydrogen from a partially 2D-loaded sample (Fig. 3.11a and b), the subsequent raise in pressure results in a very fast rehydrogenation ($t < 10$ min) of the regions that had been hydrogenated earlier (Fig. 3.11c). Note that a ‘normal’ hydrogenation at this hydrogen pressure would take at least several days. After keeping the dehydrogenated sample in 50 mbar 20% O_2 in Ar for several hours, such a quick rehydrogenation does not occur.

We propose that the absence of a significant nucleation barrier in desorption may be due to a difference in the mechanics of the ab- and desorption processes: when hydrogen is absorbed, the film has to be plastically deformed to accomodate the 30% thickness expansion. In desorption, however, the the contraction may occur on a different timescale than the hydrogen desorption. In this case, first a porous structure with voids or vacancies may be formed.[91, 92] With time this structure may collaps and rearrange plastically to form a dense film again. This mechanism may be accomodated by the good lattice match between (0001)-Mg and (111)-TiH_2, which would allow for easy nucleation of Mg. This nucleation effect has been observed in TiF_3 catalyzed Mg nanoparticles.[81]

The above mechanism explains the very fast rehydrogenation of films that were dehydrogenated shortly before. Exactly the areas that had been hydrogenated before quickly rehydrogenate, because little work is needed for the hydride to fill up the already defect-rich Mg layer. Apparently, plastic rearrangements take place at a time scale of several hours. If the unstable porous structure could be stabilized, fast hydrogenation with limited hysteresis is possible in such confined systems.

3.4 Discussion

Our observations clearly show the importance of nucleation in the hydrogenation process of confined thin films. The direct observation of growth fronts allows us to evaluate essential aspects of the growth process in relation to the thermodynamic driving force. On the basis of a simple model, we obtain the exact value of the absorption plateau pressure $\overrightarrow{p}$ for 10 nm Mg, and deduce its value for bulk Mg.

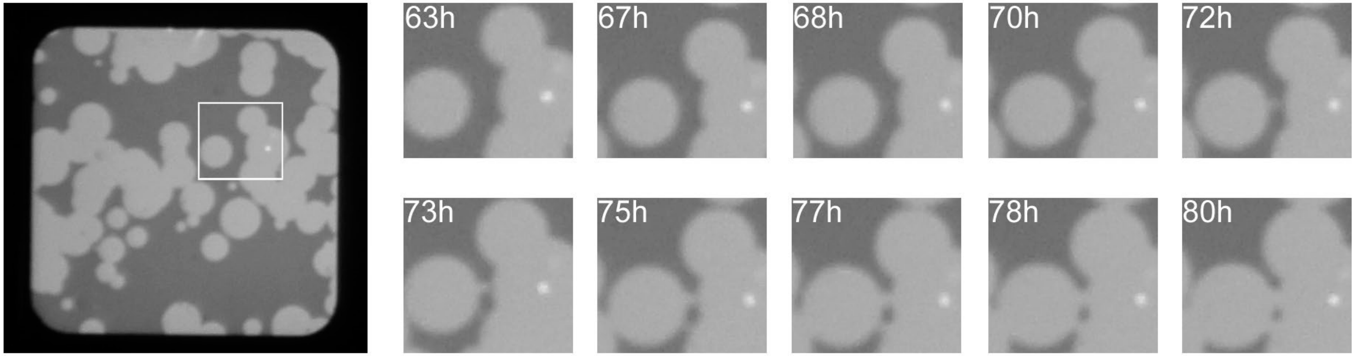

Figure 3.9 Sample (10 nm Mg, illuminated area 9x9 mm) after 63 h (left), where the white square (2.3x2.5 mm) indicates the region that is followed in time. The followed region at several times (right), shows the avalanche-type growth which can occur when two nuclei grow towards each other. From $t = 72\ \mathrm{h}$ and onwards, the formation of two bridges can be distinguished. The first forms between the hydride domain on the left and the middle of the domain on the right. The second bridge forms again between the domain on the left and the bottom of the domain on the right.

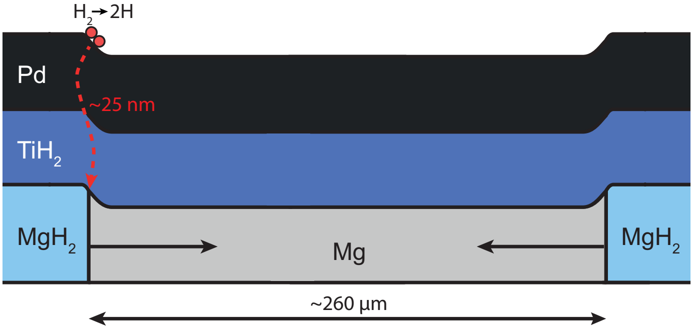

Figure 3.10 The maximum distance across which the hydride bridges can form is about 260 $\mu\mathrm{m}$, while the distance hydrogen has to travel (along the red arrow) is merely 25 nm.

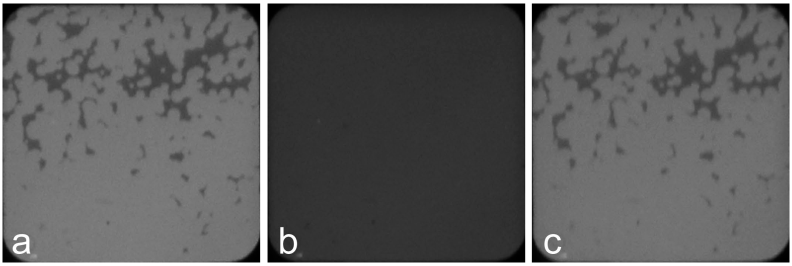

Figure 3.11 Fast reload of earlier hydrogenated domains with (a) the sample in its final state of the first hydrogenation after 25 h, (b) the sample after desorption of hydrogen as evidenced by the low light transmission, and (c) the sample during the second hydrogenation cycle after merely 10 minutes. The illuminated sample area is $9\mathrm{x}9\ \mathrm{mm}$.

Furthermore, we derive the energy needed to create the edge of the hydride domains. Due to the lattice expansion on hydrogenation a large plastic deformation takes place, which explains the large amount of energy that is needed in the nucleation process. Finally, we will discuss the thickness dependence and the asymmetry between the desorption and the absorption process.

3.4.1 Modeling of the lateral growth dynamics

We use the theory of irreversible thermodynamics to model the lateral growth of a hydride within a metallic domain. According to Machlin,[93] this theory can be applied to a system with two regions with different free energies that are joined through an interface. The main result—equal to the result from reaction rate theory[94]—states that the flux (here the interface velocity) is proportional to the driving force, if the driving force is smaller than RT. For the lateral growth of the hydride domains, the interface velocity is then equal to the boundary mobility (M^B) multiplied by the thermodynamical energy change $-\delta G$ of an infinitesimal volume containing δN mol Mg:[95]

$$v = M^B(T) \cdot \left(-\frac{\delta G(p,T)}{\delta N} \right) \tag{3.1}$$

We first describe the Gibbs free energy gained by the transition of a small volume of α-phase at the edge of a β-phase domain (Fig. 3.12). If a part of the hydride domain with length l along the α/β-interface grows with a distance δr, the corresponding Gibbs free energy change is:

$$\delta G = -\delta V \frac{\Delta g^{\alpha\beta}}{\Omega} + \delta l \gamma_e + 2\delta A \Delta\gamma_{int}$$

with δV the volume of α-phase transformed to the β-phase, $\Delta g^{\alpha\beta}$ the thermodynamical driving force per mol Mg, Ω the molar volume of Mg, γ_e the edge boundary energy per unit of length, δA the newly formed surface area of MgH_2/TiH_2 interface, and $\Delta\gamma_{int}$ the difference in interface energy between the newly formed MgH_2/TiH_2 interface and the removed Mg/TiH_2-interface. By using the relations $\delta l = {}^{l\delta r}/_{r}$, $\delta A = l\delta r$ and $\delta V = lh\delta r$ (the latter two are valid for small values of δr), with $h = h_{Mg}$, we find:

$$\delta G = lh\delta r \left[-\frac{\Delta g^{\alpha\beta}}{\Omega} + \frac{\gamma_e}{rh} + \frac{2\Delta\gamma_{int}}{h} \right] \tag{3.2}$$

Now with:

$$\delta N = \frac{\delta V}{\Omega} = \frac{lh\delta r}{\Omega}$$

we find:

$$\frac{\delta G}{\delta N} = \frac{\delta G}{\delta r}\frac{\delta r}{\delta N} = \Omega \left[-\frac{\Delta g^{\alpha\beta}}{\Omega} + \frac{\gamma_e}{rh} + \frac{2\Delta\gamma_{int}}{h} \right]$$

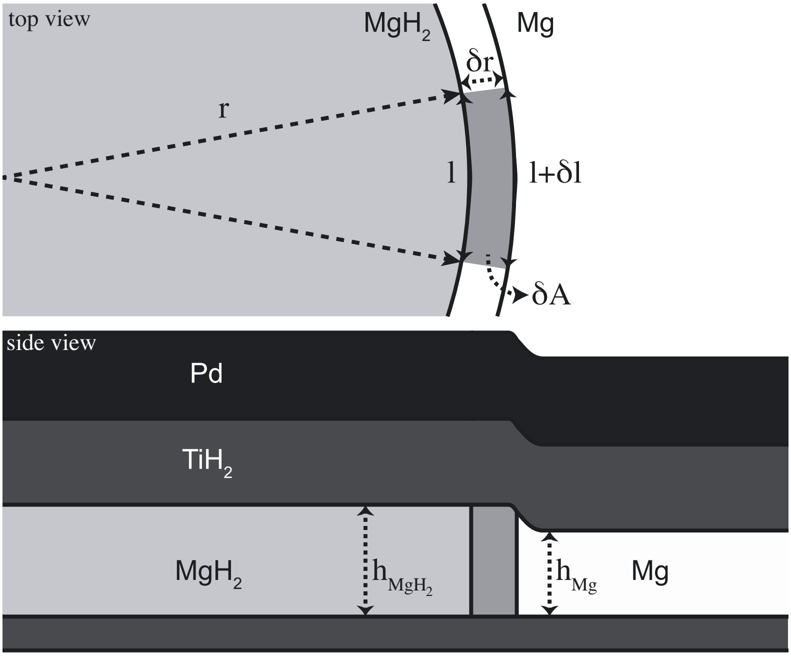
top view
MgH$_2$
Mg
δr
r
l
l+δl
δA
side view
Pd
TiH$_2$
MgH$_2$
h$_{MgH_2}$
h$_{Mg}$
Mg

Figure 3.12 Schematic of the growth process with a top view and cross section side view. A length l along the hydride edge with radius of curvature r moves by a distance δr, thus increasing the length of l by δl. The area δA now gives the area of Mg/TiH$_2$ interface replaced by a MgH$_2$/TiH$_2$ interface, counted twice because the Mg layer is sandwiched by two TiH$_2$ layers.

and inserting this result into Eq. 3.1:

$$v = -M^B\Omega\left[-\frac{\Delta g^{\alpha\beta}}{\Omega} + \frac{\gamma_e}{rh} + \frac{2\Delta\gamma_{int}}{h}\right] \tag{3.3}$$

The three terms within the brackets represent the driving force (with unit $^{\mathrm{J}}/_{\mathrm{m}^3}$). In the first term, $\Delta g^{\alpha\beta}$ is the free energy that is gained due to the phase transition per mole Mg. In the 2D nanosystem we are modelling, however, the free energy gain is reduced due to the limited available space for the hydride phase to form in. The gain in free energy is reduced by the positive edge boundary energy γ_e. Furthermore, given that the change in interface energy $\Delta\gamma_{int}$ is positive for our Mg/MgH$_2$ system in contact with TiH$_2$, the free energy change is further reduced by the $\Delta\gamma_{int}$ term. The combined unit of $M^B\Omega$ is $^{\mathrm{m}^4}/_{\mathrm{Js}}$, which is the same as the typical unit for grain boundary mobilities.[96]

3.4.2 Absorption plateau pressure

In principle, $\Delta g^{\alpha\beta}$ contains a strain energy term because of the 30% expansion of the β-phase compared to the α-phase. However, we assume this term to be negligible because in our case the hydrogenated phase is fully relaxed: The complete volume expansion is accommodated by a 30% thickness expansion.[56] Hence, assuming the hydrogen gas is in equilibrium with both the α and the β phase, we may say that $\Delta g^{\alpha\beta}$ is equal to $\Delta\mu$, the chemical potential difference between the applied hydrogen pressure and the absorption pressure [89]:

$$\Delta\mu = \mu_H^{appl} - \overrightarrow{\mu_{H,b}} = {}^1\!/_2 RT\ln\left(\frac{p^{appl}}{\overrightarrow{p_b}}\right) \tag{3.4}$$

where $\overrightarrow{p_b}$ is the absorption plateau pressure for bulk MgH$_2$, which we may use because $\Delta g^{\alpha\beta}$ is not affected by size. We find $\overrightarrow{p_b}$ by measuring the interface velocities while varying the applied pressure. If the domain radius r is large enough, the interface velocity is constant and the $\frac{\gamma_e}{rh}$-term in Equation 3.3 is zero. The value of $\Delta\gamma_{int} = 0.33$ $^{\mathrm{J}}/_{\mathrm{m}^2}$ was obtained previously.[84] After combining Equation 3.3 with $r \gg$ and Equation 3.4 we find:

$$\overrightarrow{p_b} = \frac{\overrightarrow{p}}{\exp\left[\dfrac{4\Delta\gamma_{int}\Omega}{RTh}\right]} \tag{3.5}$$

where $\overrightarrow{p}$ is the absorption pressure for 10 nm Mg, the pressure where the growth velocity $v = 0$. Figure 3.13 shows the measured interface velocities versus $\log\left(p^{appl}\right)$. The intercept with the x-axis is equal to $\overrightarrow{p} = 45.7 \pm 2.4$ Pa. This value of the equilibrium hydrogenation pressure is in accordance with the pressure needed to rehydrogenate a sample in a sub-hysteresis scan as shown in Fig. 3.5. In a bulk sample the

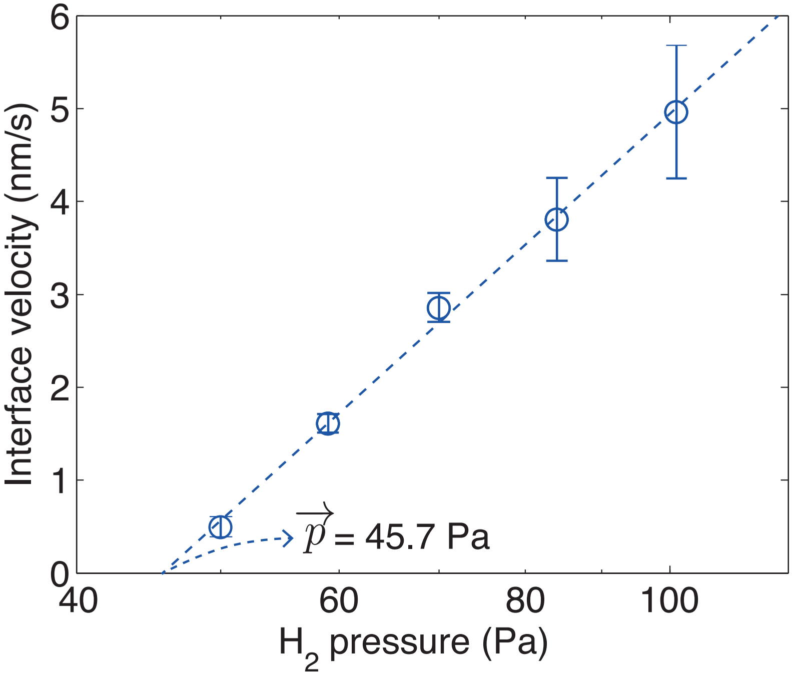

Figure 3.13 Average interface velocity from multiple linescans versus the applied hydrogen pressure (log axis) at 90 °C. The intercept gives the pressure where the growth velocity is zero, which is the pressure where the driving force is zero. The error bars indicate the standard deviation of the averaging of the velocities.

interface term due to the multilayer structure is absent. Correcting for the presence of this term (using $\Delta\gamma_{int} = 0.33$ J/m^2), we find for the bulk hydrogenation equilibrium pressure a value of $\overrightarrow{p_b} = 25$ Pa.

The absorption pressure of 25 Pa agrees with literature data derived from bulk data. We calculate that Mg would hydrogenate at 22 Pa at 90 °C with ΔH and ΔS values from Stampfer *et al.*[14], based on measurements at high temperature ($440 < T < 560$ °C). Although their results are based on hydrogen desorption measurements, hysteresis is usually small at high temperature. Absorption bulk data were measured by Pedersen *et al.*[97], from which we extrapolate an absorption pressure of 32 Pa. An advantage of comparing our result to high temperature data is that a nucleation barrier is probably absent at high temperatures. Hence, although obtained from 10 nm Mg layers, the found pressure for bulk hydrogenation of Mg agrees well with the literature.

3.4.3 Deforming multiple layers: the edge boundary energy

The edge boundary energy contains the energy needed to create a curved α/β-interface as is drawn in Fig. 3.12. Since the hydrogenation involves an expansion of the lattice, we have to include the deformation of the TiH_2 and Pd layers on top of the Mg layer in our consideration. Hence the value of γ_e provides insight into how much energy is needed to create this curved and higly deformed three layer structure.

We will derive the edge boundary energy from the radial dependence of the interface velocity. Although in principle γ_e may be derived from Equation 3.3, the phase boundary velocities of the nuclei do not appear to depend on the radius. This implies that the radius is large enough for the $\frac{\gamma_e}{rh}$-term to be negligible. Therefore, in an alternative approach, we measured the velocity of the cusp that is formed when two hydride domains grow into each other (Fig. 3.14). Such a cusp will have a radius of curvature that is negative, and its velocity can be related to the velocity of large single domains through the value for the critical nucleus radius r_c. This is the radius where the hydride domain would neither grow or shrink, hence this is the radius where:

$$\frac{\delta G}{\delta r} = \frac{\delta G}{\delta N} = 0$$

From Equation 3.3 we find the following expression for the critical nucleus:

$$r_c = \frac{\gamma_e}{\frac{h\Delta\mu}{\Omega} - 2\Delta\gamma_{int}} \tag{3.6}$$

With the velocity of large domains ($\frac{\gamma_e}{rh} = 0$) proportional to:

$$v_\infty \propto \Omega\left[-\frac{\Delta\mu}{\Omega} + \frac{2\Delta\gamma_{int}}{h}\right],$$

we derive:

$$\frac{v(r)}{v_\infty} = 1 - \frac{r_c}{\rho} \tag{3.7}$$

Here, ρ is the radius of curvature. This equation is the same as the one found for the velocity of crystal steps on a flat surface; the growth velocity of such steps are limited by an edge boundary energy as well.[98, 99]

The cusp position versus time of two domains of roughly equal size is extracted from the linescan shown in Fig. 3.14. We analyze the data such that we may directly use Equation 3.7 to obtain r_c and then via Equation 3.6 we obtain γ_e. As a first step we derive the cusp velocity from the slope of Fig. 3.14 at several times t. From the image of the sample at time t, we then estimate the radius of curvature of the cusp. We do so by drawing a circle that fits the curvature best by eye. The obtained data are shown in Fig. 3.15, which reveals a linear behavior of the cusp velocity

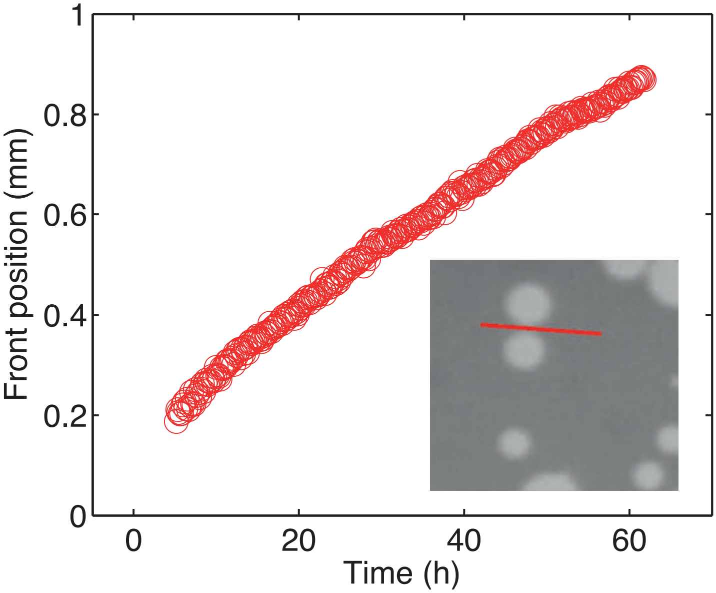

Figure 3.14 The inset (visible area 3.1x3.1 mm) shows the linescan (red) at the cusps of two hydride domains of like size growing into each other at t = 38 h. The edge position of the cusp on the right side is then taken from separate linescans at different time steps.

versus $1/\rho$. From Equation 3.7, we know that the slope of this line should be equal to $-v_\infty \cdot r_c$, while the intercept at $1/\rho = 0$ ($\rho = \infty$) should be equal to v_∞. From a linear fit we find $v_\infty = 2.7\ \mathrm{nm}/\mathrm{s}$ and $r_c = 31\ \mu\mathrm{m}$. The value for v_∞—the velocity independent of the radius of curvature—is in good agreement with the growth velocity we found for a single domain: $2.8\ \mathrm{nm}/\mathrm{s}$.

With $r_c = 31\ \mu\mathrm{m}$ put into Equation 3.6 we find for γ_e:

$$\gamma_e = r_c \left(\frac{h \Delta\mu}{\Omega} - 2\Delta\gamma_{int} \right) = 14 \cdot 10^{-6}\ \mathrm{J}/\mathrm{m}$$

with $\Delta\mu = 1.55$ kJ/mol (Eq. 3.4 with $p^{appl} = 70$ Pa, $\overrightarrow{p_b} = 25$ Pa, $T = 363$ K), $h = 10$ nm and $\Omega = 14 \cdot 10^{-6}$ m^3/mol Mg, $\Delta\gamma_{int} = 0.33$ J/m^2.

Once we calculate the equivalent surface energy from γ_e, it becomes clear that $\gamma_e = 14 \cdot 10^{-6}$ J/m represents a formidable energy. If we assume for the sake of argument that the edge can be described as sharp, we are then dealing with a 3 nm increase in height (Mg expands 30%). Hence, the edge term then represents a surface energy of $\frac{\gamma_e}{3\ \mathrm{nm}} = 0.5 \cdot 10^4\ \mathrm{J}/\mathrm{m}^2$, which is about 4 orders of magnitude larger than a typical surface or interface energy. This unphysical result can only be understood if we take into account the plastic deformation which is involved in the formation of this edge. We propose that the plastic deformation—needed to accommodate the expan-

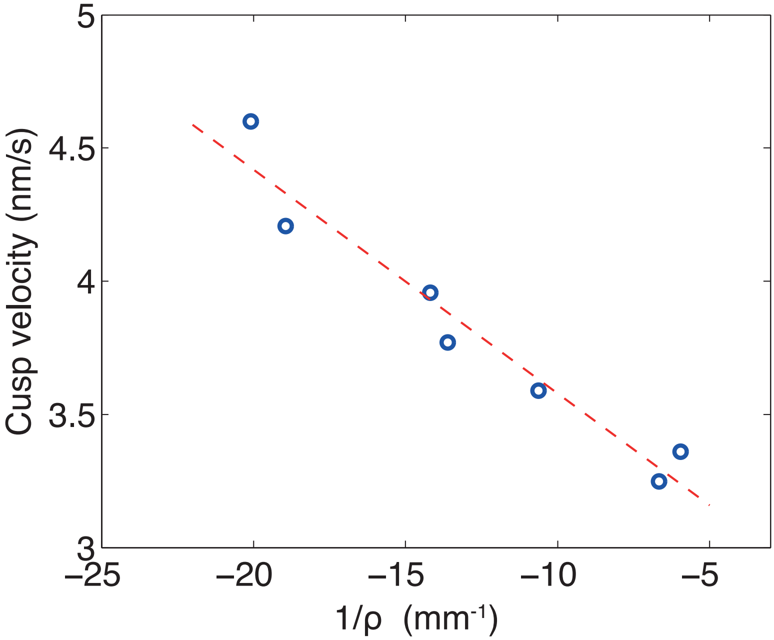

Figure 3.15 The cusp velocity estimated from Fig. 3.14 is plotted against the inverse oscullating circle radius, ρ^{-1}. The dashed line is a least squares fit using Equation 3.7.

sion of the Mg lattice—extends over a large volume surrounding the step edge. If we assume that the deformation of the three layers takes place along 300 nm (having a 1% slope, thus less steep than presented in the model in Fig. 3.12), we may divide γ_e over this area which contains the MgH_2, the top TiH_2, and Pd layers:

$$\begin{aligned} \gamma_e^{vol} &= \frac{\gamma_e}{300 \cdot 10^{-9} \cdot (h_{MgH_2} + h_{Pd} + h_{TiH_2})} \\ &\simeq 1.9 \cdot 10^9 \ \mathrm{J}/\mathrm{m}^3 \end{aligned} \tag{3.8}$$

The γ_e^{vol} can be seen as the total energy to create an edge including the plastic deformation involved. The 1.9 GPa value we find is in agreement with the stresses estimated from hysteresis broadening of 50 nm Mg layers.[60] The value of γ_e depends strongly on the volume of the interface, which we now only estimate. In the future, we hope to observe the interface at the micro or nanoscale with, for instance, atomic force microscopy.

3.4.4 Mg thickness dependence

Part of the reason that we performed the hysteresis scans was to investigate the nature of the increased hysteresis when decreasing the Mg layer thickness from 10 to 2 nm.[84] Since the 10 nm layer may be hydrogenated at much lower pressures than expected from a normal PTI experiment, the difference in hysteresis appears to be even larger than we thought before. This raises the question whether the difference in interface energy $\Delta\gamma$ we determined to be 0.33 $\mathrm{J/m^2}$ is valid.

The desorption pressure of the 3 nm Mg layer sample is not significantly higher than the one for 10 nm Mg. This, combined with the observed difference in the hydrogenation dynamics for ab- and desorption, suggests that the nucleation (and growth) mechanism may differ from the one in absorption. If we follow Flanagan *et al.*,[89] however, and assume that $\widetilde{p}$ represents the equilibrium pressure, we may conclude that the 3.1 nm layer ($\widetilde{p} \approx 47\ \mathrm{Pa}$) is indeed destabilized compared to the 10 nm layer ($\widetilde{p} \approx 20\ \mathrm{Pa}$). From these two values, we can calculate $\Delta\gamma$ through:[84]

$$\Delta\gamma = \frac{\ln\left(\frac{\widetilde{p}_2}{\widetilde{p}_1}\right)}{\left(\frac{1}{h_2} - \frac{1}{h_1}\right)} \frac{RT}{2\Omega_{Mg}} = 0.4\ \mathrm{J/m^2}$$

with $\widetilde{p}_1$ the pressure for 10 nm Mg, $\widetilde{p}_2$ for 3.1 nm Mg, h_1 and h_2 the respective thicknesses of Mg. Thus, our hypothesis—thin MgH_2 is destabilized compared to bulk due to the interface energy difference between metal and hydride phase—still holds. A more thorough investigation with more Mg layer thicknesses is planned for the future.

The absence of visible 2D-growth of the hydride phase in 3.1 nm layers may be caused by the interface roughness. Possibly, at 3 nm, the Mg layer looses its 2D character, which could limit the extent by which lateral growth may occur.

Another factor that may be involved, is the way plastic deformations propagate. This might be different for different thicknesses. Huang *et al.*[100] have for instance shown the propagation of defects can occur in Cu thin films with grain size of ∼12 nm, while in Ta with grains of 3 nm this was impossible. According to Carlton *et al.*,[101] materials with grains $< 10\ \mathrm{nm}$ have a highly increased chance for grain boundaries to absorb defects. The grain size of the Mg layers studied here is approximately equal to the thickness of the layer. Hence, if the chance of absorbing propagating defects is higher for the 3 nm layers than for the 10 nm layers, lateral growth of the hydride phase is indeed hampered in the 3 nm layers.

3.5 Conclusion

We observe 2D-nucleation and growth of MgH_2 in 10 nm Mg layers at moderate hydrogen over-pressures. The nuclei form across the Mg layer and then extend laterally. The low nucleation density suggests the presence of preferential nucleation sites, probably defects or secondary phases.

We derived a growth model which takes both the edge and the interface energy into account. The expansion rate of the nuclei then allows us to deduce the bulk hydrogen absorption pressure of Mg from data of 10 nm Mg layers, which is indeed consistent with literature. We deduce the edge boundary energy from the velocity and osculating circle radius of the cusp which is formed when two hydride domains grow into each other. The value of the edge boundary energy is extremely large ($14 \cdot 10^{-6}$ $^{\mathrm{J}}/_{\mathrm{m}}$). We attribute this to the plastic deformation of the Mg, TiH_2 and Pd layers which is needed to accomodate the large volume expansion of Mg on hydrogenation.

In contrast to the 10 nm Mg layers, we observe no 2D-growth of the hydride phase in 3 nm Mg layers. This size effect may be due to the increased relative roughness of the 3 nm layer or due to the annihilation of propagating defects at grain boundaries.

We furthermore observe that, while we see no lateral growth during desorption, fast resorption at low overpressure is possible if performed within several hours of dehydrogenation. We attribute this behavior to the asymmetry of the phase transformations: when hydrogen is absorbed, the Mg layer has to expand and deform during the actual hydrogen uptake. During desorption, however, the deformation process may be uncoupled in time from the hydrogen release.

The possibility to detect single magnesium hydride nucleation sites and the easily observed growth in Mg thin film multilayer system are uncommon for a solid state phase transformation. This makes Mg-based multilayers ideal to study the fundamentals of nucleation and growth in general, and in particular to investigate the effects on nucleation and growth by nanoconfinement. Our first results show that in nano-structured materials the effect of nucleation and growth on hydrogenation can be substantial. In order to conclude that a thermodynamic destabilization is obtained, a detailed analysis of the hysteresis of the process is needed.

3.6 Appendix

In this appendix we discuss additional, preliminary results that further elaborate on the lateral growth mechanism of the MgH_2 domains. The activation energy for the edge boundary movement is estimated from the boundary mobilities obtained at two temperatures. Furthermore, we have found direct evidence that indeed the plastic deformation of the surrounding TiH_2 and Pd layers plays a large role in the hydrogenation thermodynamics, because we find that the lateral growth velocity of the hydride domains directly depends on the thickness of the Pd capping layer.

3.6.1 Edge boundary movement activation energy

Measuring the lateral growth velocity as a function of temperature allows us to determine the activation energy for the boundary to migrate. We begin by extracting the mobility M^B from lateral growth velocity versus hydrogen pressure data. If we take Equation 3.3 and combine it with Equation 3.4, we obtain that the slope $\frac{dv}{d\ln p^*}$ (with $p^* = \frac{p^{appl}}{\overrightarrow{p^b}}$) of the lateral growth velocity v versus the applied pressure is:

$$\frac{dv}{d\ln p^*} = -M^B\Omega\left[-\frac{RT}{2\Omega}\right] = \frac{RT}{2}M^B$$

This is valid when assuming that γ_e and γ_{int} are pressure independent. From the slope of the line in Figure 3.13 and the equation above, we obtain a edge boundary mobility of 4.19×10^{-12} $^{\mathrm{mol \cdot s}}/_{\mathrm{m \cdot kg}}$ at 363 K. Figure 3.16 shows the measured lateral growth velocities at 393 K. From the slope and using the equation above we again obtain the edge boundary mobility, which is now equal to 1.19×10^{-12} $^{\mathrm{mol \cdot s}}/_{\mathrm{m \cdot kg}}$. Both mobilities are shown in Table 3.1 and furthermore the data are converted to unit $^{\mathrm{m}^4}/_{\mathrm{J \cdot s}}$, which is generally used when describing grain boundary mobilities.

From the difference between these two mobilities, we obtain an estimate of the involved activation energy for the migration of the edge boundary. We assume that the mobility follows a general Arrhenius behavior:

$$M^B = M_0^B \exp\left(-\frac{\Delta^a G}{RT}\right)$$

From the two mobilities we find $\Delta^a G = 41$ $^{\mathrm{kJ}}/_{\mathrm{mol\,Mg}}$ (21 $^{\mathrm{kJ}}/_{\mathrm{mol\,H}}$). Again, this activation energy is obtained from only two data points, hence its value is highly tentative. Typical values for the activation energy of H-diffusion in MgH_2 are approximately 80 $^{\mathrm{kJ}}/_{\mathrm{mol\,H}}$, much larger than the activation energy we find.[102, 103] Hence, this provides further evidence that the observed lateral growth is indeed not related to hydrogen diffusion. We believe the activation energy is related to movement of the edge due to the hydrogenation of Mg. This includes the mechanical deformation of the Mg layer, as well as of the top TiH_2 and Pd layers.

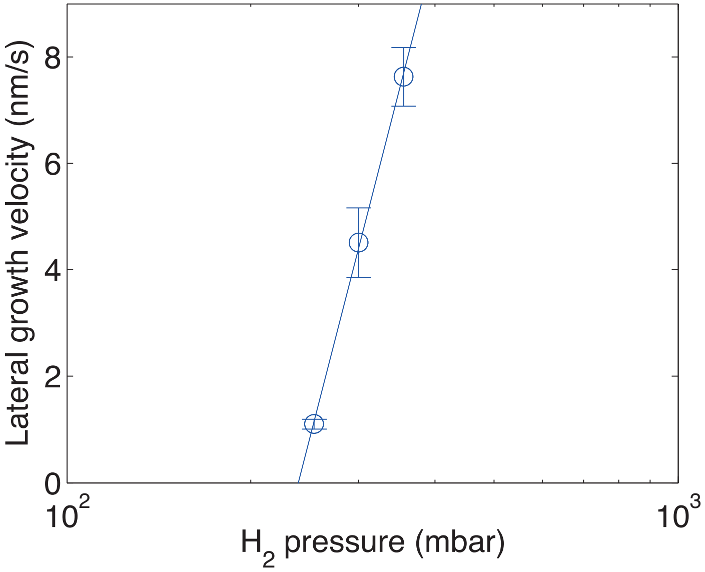

Figure 3.16 Average interface velocity from multiple linescans versus the applied hydrogen pressure (log axis) at 120 °C. The intercept where the growth velocity is zero is at 239 Pa. The error bars indicate the standard deviation of the averaging of the velocities.

T (K)	M^B $\left(\mathrm{mol\cdot s}/\mathrm{m\cdot kg}\right)$	$M^B \cdot \Omega$ $\left(\mathrm{m^4}/\mathrm{J\cdot s}\right)$
363	$4.19 \cdot 10^{-12}$	$5.87 \cdot 10^{-17}$
393	$1.19 \cdot 10^{-11}$	$1.67 \cdot 10^{-16}$

Table 3.1 Mobilities obtained from the slopes of Figures 3.13 and 3.16.

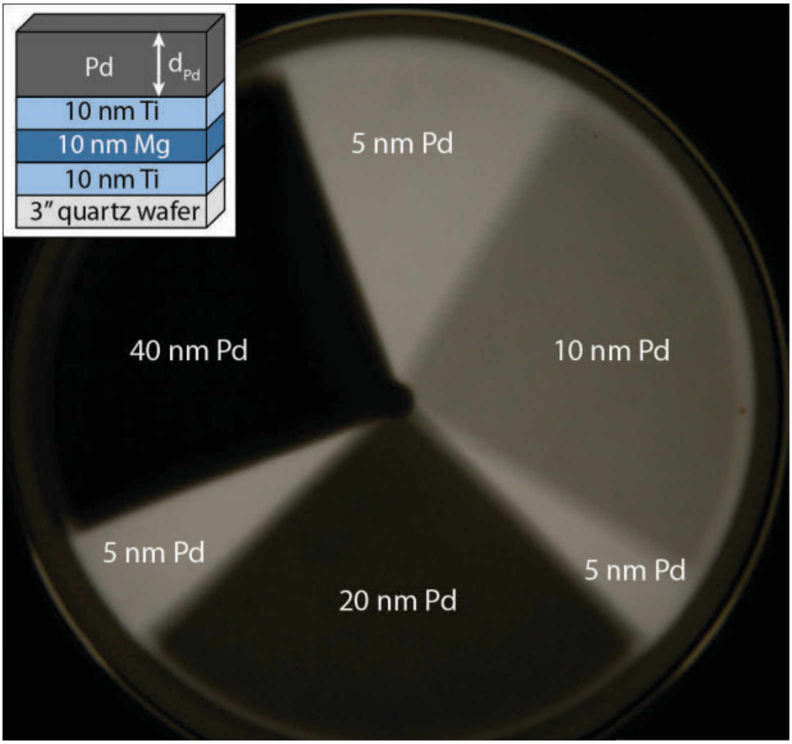

Figure 3.17 Photo in transmission of the 3" quartz wafer sample with 10 nm Ti, 10 nm Mg, 10 nm Ti and a Pd layer with varying thickness, as indicated in sample. In the top left a scheme of the cross section is given. The shape of the sections with different Pd thickness are so due to the mask used during the sputter process.

3.6.2 Pd thickness dependence of the lateral growth velocity

To prove that the mechanical deformation of the top layers is indeed contained in the the edge boundary energy, we change the Pd thickness while the rest of the multilayer stack remains the same (*i.e.* 10 nm Ti/ 10 nm Mg / 10 nm Mg / X nm Pd). We used a 3" quartz wafer substrate on which we deposited the multilayer with several Pd thicknesses. Figure 3.17 shows a photo of the sample in transmission, with the Pd thickness—which range from 5 to 40 nm—indicated within.

Figure 3.18 shows an image of the sample after being exposed for 68 hours to hydrogen at a pressure of 70 Pa. The 40 nm Pd region is optically enhanced to show the MgH_2 domains. We first qualitatively observe that the nucleation rate appears to be affected by the Pd thickness. In this first hydrogenation cycle, there number of MgH_2 nuclei in the 5 nm Pd region is larger than in the 10 nm region, which in turn has more nuclei than in the 20 nm Pd region. In the 40 nm Pd region the trend is not

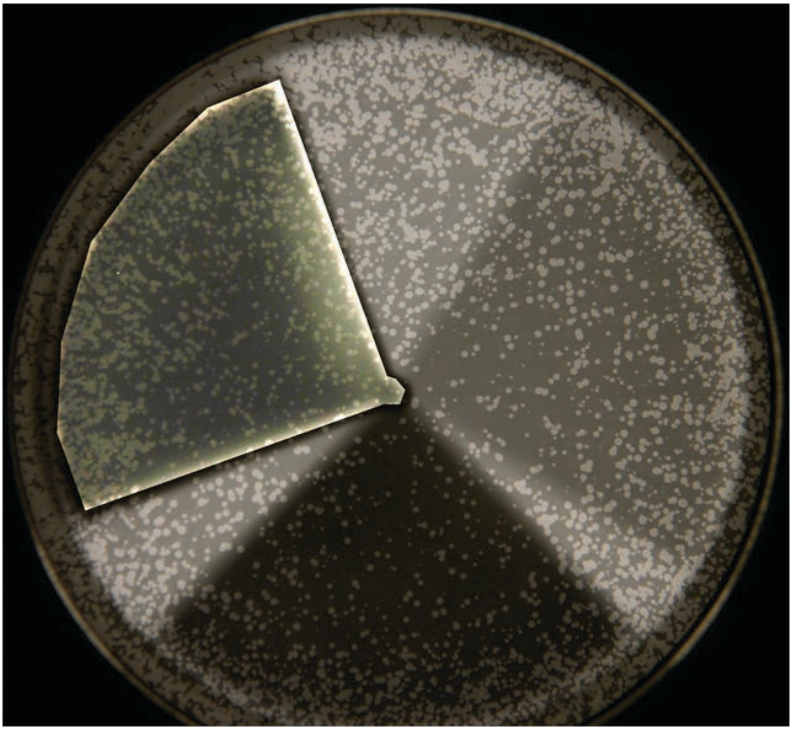

Figure 3.18 Photo in transmission of the 3” wafer sample after being exposed to 70 Pa H_2 for 68 hours. The 40 nm Pd region (top left) has been optically enhanced to show the MgH_2 domains.

continued, for reasons unknown at this time. On the edge of the sample there are many more MgH_2 domains, which is possibly the result of the different stress state of the multilayer in this region. Another explanation for this larger nucleation rate at the edge could be the sawing and polishing of the substrate, which may result in more defects on the edge than in the center.

We again analyze the lateral growth velocity of MgH_2, now as function of the Pd layer thickness. Figure 3.19 shows the lateral growth velocities as a function of the Pd thickness. The velocities are the average of the measured velocities of six different MgH_2 domains, with the error bars indicating the standard deviation. At 40 nm Pd, the growth velocity is 1.3 nm/s, which increases via 1.45 nm/s (20 nm Pd), 1.55 nm/s (10 nm Pd) to 1.85 nm/s (5 nm Pd). Indeed, an increasing growth velocity with decreasing Pd thickness is what we would expect, because less volume has to be deformed by the moving MgH_2/Mg edge boundary for thinner Pd. Although in principle the volume of Pd scales linearly with the Pd thickness, in this case the velocity does not decrease linearly with d_{Pd}. This is so because the mechanical properties

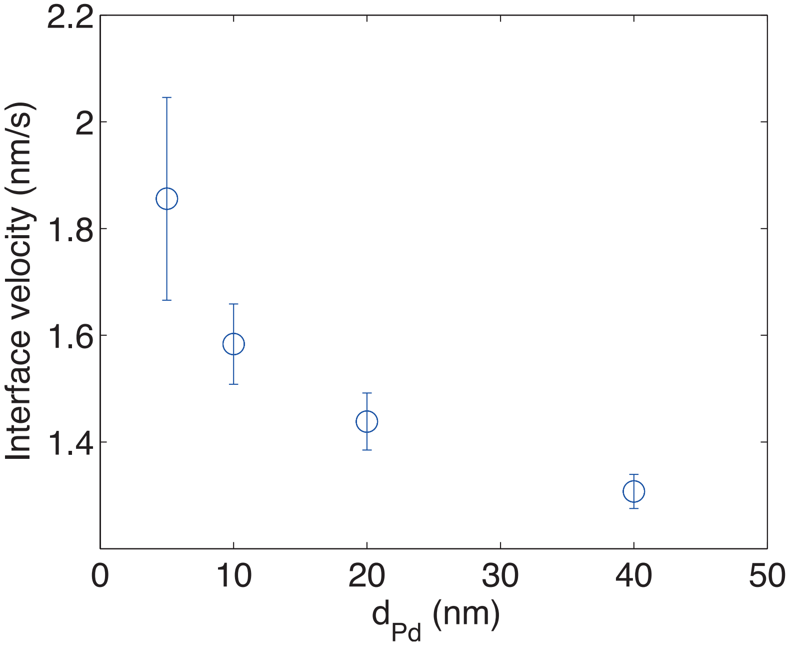

Figure 3.19 Lateral growth velocity of MgH_2 domains within a 10 nm Mg layer as a function of the Pd layer thickness.

of the Pd layer also change with changing thickness. Furthermore, presumably the thermodynamical driving force for hydrogenation (i.e. $\frac{1}{2}RT\ln\frac{p^{appl}}{\overrightarrow{p}}$) may change with d_{Pd}, because $\overrightarrow{p}$ (the hydrogen pressure where the lateral growth velocity $v = 0$) changes. We predict that $\overrightarrow{p}$ increases with increasing Pd thickness, however more elaborate experiments would have to be performed. Note that the growth velocity for 10 nm Pd is inconsistent with the earlier measured 2.9 nm/s (Figure 3.13). For now, we assign this difference to these experiments being of the first hydrogenation cycle and furthermore to the different in quartz substrate. Internally, however, the data indeed shows a real change in the magnesium hydride growth velocity versus the Pd thickness.

Chapter 4

Nucleation and growth mechanisms from JMAK analyzed hydrogenation kinetics

4.1 Introduction

Magnesium hydride is a hydrogen storage material with a large gravimetric hydrogen density (7.6 wt%) and volumetric density (110 kg/m^3)—both larger than high pressure hydrogen.[9] The succesful application of magnesium hydride remains a challenge mostly because it is very stable; hydrogen is only released from the material at 1 bar H_2 pressure at about 300 °C.[14, 97] Nanostructuring and nanoconfinement are considered promising ways to destabilize the magnesium hydride, thereby decreasing the desorption temperature.[33, 74, 78, 70, 104] To enable good control over nanosize and nanoconfinement, we investigate the hydrogenation of Mg thin films.[84] In particular, we study the 1-dimensional nanoconfiment of Mg and MgH_2.

In the previous chapter, we found that the hydrogenation of 10 nm layers of Mg (Figure 4.1a) occurs via a nucleation and growth mechanism.[105] The TiH_2 layers serve to protect Mg from chemical interactions with the substrate and Pd-capping layer. The Pd protects the multilayer from oxidation and catalyzes the hydrogen dissociation reaction. When applying a relatively low pressure of hydrogen to these multilayers, MgH_2 islands are observed optically. Because of the low density of nuclei, we are able to directly observe the 2-dimensional, in-plane growth (Figure 4.1b). Before merging with other magnesium hydride islands, the individual islands may grow up to millimeters in size. In Figure 4.1b the individual MgH_2 domains, which grow isotropically with time, are clearly visible. The bright MgH_2 domains are highly visible due to the large change in optical transmission when the metal Mg transforms to the

---

This chapter is based on: Lennard Mooij and Bernard Dam, Phys. Chem. Chem. Phys. 15, 2013, 11501

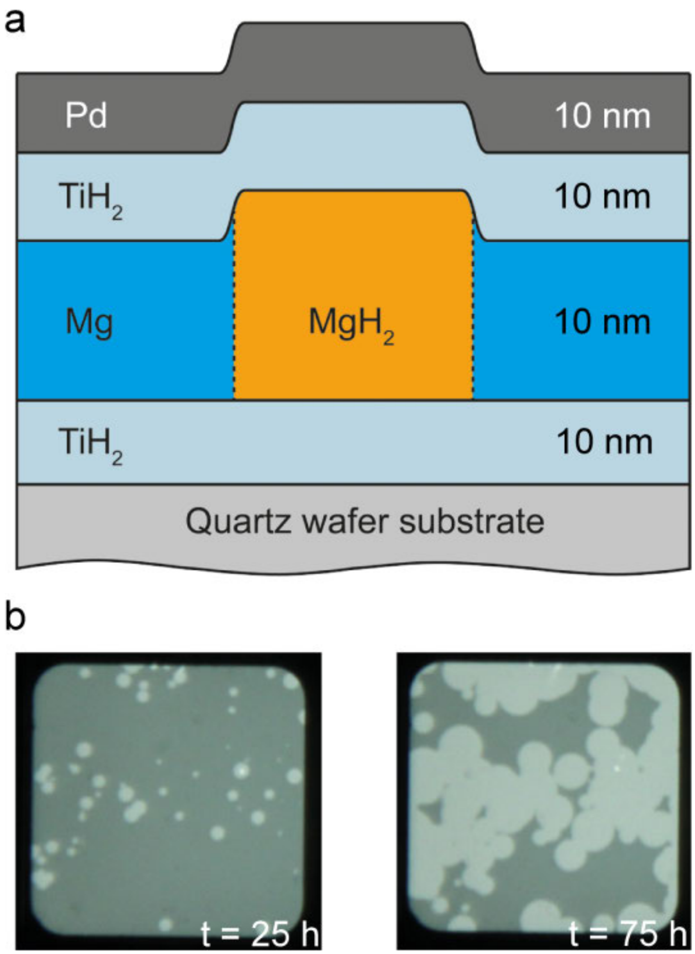
a
Pd
10 nm
TiH$_2$
10 nm
Mg
MgH$_2$
10 nm
TiH$_2$
10 nm
Quartz wafer substrate
b
t = 25 h
t = 75 h

Figure 4.1 The side view (a) represents the TiH$_2$/Mg/TiH$_2$/Pd multilayer with a nucleated MgH$_2$ domain in the middle. As MgH$_2$ is expanded about 30% compared to Mg, the domain pushes the top TiH$_2$ and Pd layers upwards, thereby deforming these layers. The top view (b) is given by images of the 10x10 mm samples in transmission after multiple hours of exposure to hydrogen ($p_{H_2} = 70$ Pa, $T = 363$ K). The MgH$_2$ domains transmit more light and are brighter. Over time, both nucleation and growth occur.

insulator MgH_2.

We observed that in subsequent hydrogenations at low driving force, the nuclei appear at similar spots in the sample. This indicates the nucleation occurs at preferential sites.

The magnesium hydride domains are, however, only visible at relatively low pressure ("low-pressure", 70 Pa H_2, $T = 363$ K), when only a small amount of nuclei are formed. At a somewhat higher pressure ("high-pressure", 100 Pa H_2), separate magnesium hydride domains can not be distinguished. In this case—with a resolution of 20 μm/pixel—we see a gradual increase in the optical transmission.[105] The question then arises whether our observations of the growth mechanism can be generalized to high overpressures.

Furthermore, when desorbing the hydrogen, we did not observe nucleation and growth of Mg. Instead, we see a gradual decrease in transmission until the transformation is complete. Again the question is whether the difference between ab- and desorption is caused by a different growth mechanism or simply because the abundance of nuclei prevent the optical system to detect them.

To answer these questions, we analyze the hydrogen ab- and desorption of the 10 nm Mg layers using the Johnson-Mehl-Avrami-Kolmogorov (JMAK) kinetical model.[106, 107] The kinetics of nanosize metal hydride materials are often analyzed using this model, probably owing to the relatively simple relation between the phase fraction f and time:

$$f = 1 - \exp(-kt^n) \tag{4.1}$$

Here, k is the rate constant and n the growth dimension. The growth dimension can be linked to the nucleation and growth mechanism of the transformation process. The equation's simplicity is perhaps a double-edged sword: It is easy to use and suggests a simple relation between the growth dimension and the growth mechanism. The interpretation of this equation, however, is prone to errors because different growth mechanisms may provide similar values for n. Hence, care must be taken when interpreting data solely on the basis of n.[95]

From the derivation of the JMAK equation it is clear that the growth dimension may be split up into two componenents; one for the nucleation process (n_n) and one for the growth process (n_g). The sum of these two is equal to n.[95, 108]

We will apply a JMAK analysis to the optical transmission data obtained when hydrogenating thin Mg films. At low pressure (70 Pa H_2) we can directly relate this analysis to our visual observation of the nucleation and growth process and thus verify our interpretation. We then apply the JMAK analysis to the nucleation and growth behavior under conditions which do not allow for the optical observation of growth islands (high-pressure—*i.e.* 100 Pa H_2—and dehydrogenation). We find evidence that at high pressure a similar 2D-growth mechanism applies as at low overpressures. For the dehydrogenation, we propose that Mg grows in a 1-dimensional fashion, due to a decoupling between the plastic deformation and the nucleation of Mg.

4.2 Experimental

Multilayers of 10 nm Ti, 3.1 or 10 nm Mg, 10 nm Ti and 10 nm Pd are deposited on 10x10 mm quartz wafer substrates by magnetron sputter deposition. The ultrahigh vacuum chamber has a base pressure of 10^{-9} mbar (AJA Int.). Sputter rates are typically 0.08 $\mathrm{nm/s}$ for Ti (200 W DC), 0.23 $\mathrm{nm/s}$ for Mg (150 W RF) and 0.12 $\mathrm{nm/s}$ for Pd (50 W DC). All the deposited layers are polycrystalline and textured, with the closest packed planes (Mg hcp-(0001), Ti hcp-(0001) and Pd fcc-(111)) parallel to the substrate.[56]

After a change in hydrogen pressure, the change in optical transmission of the multilayer sample is recorded as a function of time at constant temperature (here 90 $^{\circ}$C) with Hydrogenography: We place multiple samples in a stainless steel hydrogenation cell (10^2 to 10^6 pa absolute pressure), which in turn is placed in a furnace. Both cell and furnace have windows to allow light to pass through the thin films. The transmitted light—which comes from a 150 W quartz-tungsten-halogen lamp—is recorded either with a 3-CCD camera or a Canon EOS 550-D.

With the 3-CCD camera we record the average transmission of the samples per time-step (5 s or longer). After a change in hydrogen pressure is applied, we record the dynamics of the hydrogen ab- or desorption. These data are then converted to a new phase (hydride or metal) phase fraction (see results). Thereafter the data are analyzed using the JMAK equation.

Three different types of data are analyzed, which we call ‘low-pressure’, ‘high-pressure’ and ‘desorption’ data. The low-pressure, high-pressure and desorption data are measured at respectively a hydrogen pressure of 70 Pa, 100 Pa and 8 Pa. These pressures relate to our previous experiments, where at 70 Pa we optically observed the 2D growth of a low number of MgH_2 domains. At 100 Pa we did not observe separate MgH_2 domains, but a gradual increase in optical transmission of the entire sample. For further details readers are referred to Ref. 10.

All the sample images are recorded with a Canon EOS 550-D, at a resolution of 20 $\mu\mathrm{m}/\mathrm{pixel}$. For the JMAK analyses only the data from the 3-CCD camera is used.

4.3 The JMAK equation for 2D nuleation and growth

Here we will derive the JMAK equation for a thin film (2D) system, in which α-phase Mg converts to β-phase MgH_2 through a nucleation and growth process. The derivation is based on Christian[95], but adapted to our thin film system.

In general, the phase transformation process follows an S-shaped curve (such as the one shown in Figure 4.2b), because at time $t = 0$ there are very few nuclei and their surface area is small. Therefore, initially the rate of transformation is low and steadily increases with time. Once the transformation is almost complete at larger times, the rate of transformation again decreases because most of the α-phase has been consumed. Hence, the growing β-phase domains compete for left over bits of untransformed volume and limit each other's growth.

Our treatment is based on the assumption that nucleation and growth occur across the whole Mg layer thickness. This is supported by the observation that the growth of MgH_2 domains occurs in a binary way; either a region has low light transmission (Mg) or high light transmission (MgH_2), with nothing in between. Hence, in accordance with our observations, we disregard processes that occur in a direction perpendicular to the thin film surface.

We furthermore know that, when magnesium hydride forms, the 30% lattice expansion is accomodated by a 30% layer thickness expansion. Therefore, the volume fraction of MgH_2 is proportional to the fraction of sample surface area it covers. This allows us to ignore the volume expansion and treat the phase transformation using the area of β-phase instead of its volume.

If the rate at which nuclei form per unit area is equal to I_a, then between time $t = \tau$ and $t = \tau + d\tau$ a number of $I_a \cdot A^\alpha \cdot d\tau$ nuclei will have formed. Assuming that the growth rate Υ is isotropic, in all in-plane directions, all β-phase nuclei will grow as circular islands. Consequently, a single β-phase domain that nucleats at time $t = \tau$ extends over an area:

$$\begin{array}{rclr} a_\tau & = & \pi\Upsilon^2 \cdot (t-\tau)^2 & \quad (t \geq \tau) \\ a_\tau & = & 0 & \quad (t < \tau) \end{array}$$

During the same time $d\tau$ not only have β-domains grown, but also $I_a A^\alpha d\tau$ have nucleated. In the limit of $A^\beta \ll A^\alpha$, the nuclei are widely spaced and won't impinge on each other. In this case the transformed area is:

$$dA^\beta = a_\tau I_a A^\alpha d\tau$$

Because during this short time A^α is approximately equal to the total area A, the transformed area at time t is:

$$A^\beta = \pi A \int_{\tau=0}^{t} I_a \Upsilon^2 (t-\tau)^2 d\tau$$

We know from our previous experiments that the growth rate Υ is constant,[105] at least for domains with a size larger than about $100\ \mu\mathrm{m}$ (equal to 5 pixels in our experiment). The simplest way to solve the integral is to further assume the nucleation rate I_a is constant:

$$f = \frac{A^\beta}{A} = \frac{\pi}{3} I_a \Upsilon^2 t^3$$

with f the fraction of transformed material. The above only holds for small volumes of β-phase, in the early stages of the phase transformation. At later stages we have to account for the merging of growing regions with other regions. The solution to this problem was developed by Kolmogorov, Johnson and Mehl and Avrami. They introduce so called phantom nuclei that form in the so called extended volume (here extended area).

If during time $d\tau$, $I_a A^\alpha d\tau$ nuclei are formed, $I_a A^\beta d\tau$ nuclei would have formed if the transformation had not already completed in that area. These (non existing) nuclei are the phantom nuclei. These phantom nuclei are included to describe what is called the extended area. The extended area is virtual, in the sense that β-phase regions grow as if they don't impinge on each other. They are free to grow as they please, also through each other. The extended area A_e^β then can be described by:

$$\begin{aligned} dA_e^\beta &= a_\tau I_a (A^\alpha + A^\beta) d\tau \\ A_e^\beta &= \pi A \int_{\tau=0}^{t} I_a \Upsilon^2 (t-\tau)^2 d\tau \end{aligned} \tag{4.2}$$

According to Christian:[95] "The significance of A_e^β is that it is simply related to the kinetic laws of growth, which may thus be separated from the geometrical problem of impingement." What is left is to find a relation between A_e^β and A^β.

In a random small area element, a fraction $(1 - {}^{A^\beta}\!/_{A})$ is untransformed at time t. If we let this region transform over time dt, the extended area will grow by dA_e^β and the true area by dA^β. A fraction $(1 - {}^{A^\beta}\!/_{A})$ of dA_e^β will lie in previously untransformed material, and will therefore contribute to dA^β. The remainder of dA_e^β has already been transformed and does not contribute to dA^β. Put into the form of an equation, the above becomes:

$$\begin{aligned} dA^\beta &= \left(1 - \frac{A^\beta}{A}\right) dA_e^\beta \\ A_e^\beta &= -A \ln\left(1 - \frac{A^\beta}{A}\right) \end{aligned} \tag{4.3}$$

The above is based on the assumption that nucleation occurs with equal probability over the transforming area. This condition is not met in some of our experiments, we observe very few nuclei which are not always nicely distributed (as in Figure 4.1). Therefore, this may limit the applicability of the JMAK model to our experiments with a low number of nuclei, specifically at times when impingement of domains is dominant.

If we are allowed to use Equation 4.3, we can insert it into Equation 4.2 and thereby find (with $f = {}^{A^\beta}\!/_{A}$):

$$-\ln(1-f) = \pi \Upsilon^2 \int_{\tau=0}^{t} I_a (t-\tau)^2 d\tau \tag{4.4}$$

To integrate this equation we must specify how I_a varies with time. Again, the most simple case is to assume I_a is constant, then the integral yields:

$$f = 1 - \exp\left(-\frac{\pi}{3}\Upsilon^2 I_a t^3\right) \tag{4.5}$$

One may already recognize the general form of the JMAK equation of $1-\exp(-kt^n)$.

It is likely, however, that I_a is some function of time. Therefore, we must integrate Equation 4.4 accordingly. We observed that the nucleation of the MgH$_2$ domains occurs at preferential sites. Hence, there must be a limit to the number of sites available for nucleation. Such a nucleation process is called Avrami nucleation. For now we assume it occurs in our thin film samples and we find evidence for the validity of this assumption in Section 4.4.1.

The nucleation rate per unit area I_a is derived as follows. If the initial number of sites is N_0 per unit area of α-phase, with N remaining after time t, then the number of sites being consumed during time dt is dN:

$$\begin{array}{rcl} dN & = & -N\nu_1 dt \\ N & = & N_0 \exp(-\nu_1 t) \end{array} \tag{4.6}$$

with ν_1 is the frequency with which individual sites become a nucleus. Then the nucleation rate per unit area is:

$$I_a = -\frac{dN}{dt} = N_0 \nu_1 \exp(-\nu_1 t)$$

Note that the nucleation rate is not limited by the available volume of parent phase, *i.e.* this is the nucleation rate including phantom nuclei. Substitution of the previous equation, evaluated at $t = \tau$, into Equation 4.4 will again correct for the phantom nuclei and phantom growth:

$$-\ln(1-f) = \pi\Upsilon^2 N_0 \nu_1 \int\limits_{\tau=0}^{t} \exp(-\nu_1 t)(t-\tau)^2 d\tau$$

Integration yields:

$$\begin{array}{rcl} f & = & 1 - \exp\left(\frac{2\pi N_0 \Upsilon^2}{\nu_1^2}\left[Z(t)\right]\right) \\ Z(t) & = & \exp\left(-\nu_1 t\right) - 1 + \nu_1 t - \frac{\nu_1^2 t^2}{2} \end{array} \tag{4.7}$$

The actual numbers of ν, N_0 and Υ do not matter for the discussion here. What is most important is to realize the effect on the growth dimension n when changing the value for the nucleation frequency ν_1. A small value of ν_1 implies that I_a is approximately constant, thus the equation converges to Equation 4.5 with $n = 3$. A large value of ν_1 implies that all the available nucleation sites are consumed in the beginning of the transformation (instant nucleation). In that case, Equation 4.7 converges to:

$$f = 1 - \exp\left(-\pi N_0 \Upsilon^2 t^2\right)$$

In this case $n = 2$ because there is only (2-dimensional) growth and no nucleation. If ν_1 has a value in between those of constant and instant nucleation, the nucleation rate decreases with time but the available sites are not depleted during the transformation. As a consequence, $2 \leq n \leq 3$, contrary to the common assertion that n is an integer. Note that we derive these values for n for the case of a constant growth velocity and 2-dimensional growth.

From the above, it becomes clear that the growth dimension n is simply the sum of a nucleation component and a growth component. When there is instant nucleation at time zero, no nucleation will occur during the transformation. Therefore in this case $n = 2$, and $n_g = 2$ as well. If the nucleation rate is constant in time, then $n = 3$. Knowing $n_g = 2$, makes $n_n = 1$. A way to look at it is that a constant nucleation rate may be seen as one-dimensional growth, because single small volume (or area) elements are transformed to the beta phase at a constant rate. The total n is simply the sum of n_g and n_n:

$$n = n_g + n_n \tag{4.8}$$

To allow for the practical use of the JMAK model, a generalized version of Equation 4.7 is used because values for N_0, ν and Υ are unknown. All these constants are combined into one rate constant k:

$$f = 1 - \exp(-kt^n) \tag{4.9}$$

If we plot $\ln(-\ln(1-f))$ versus $\log(t)$, the slope will reveal n through:

$$\ln(-\ln(1-f)) = \ln k + n \ln t \tag{4.10}$$

An example of data with a non-integer value for n is shown in Figure 4.2. These data are obtained from a simple simulation of a 2D-β-phase (red) nucleating and growing in the α-phase (blue). Figure 4.2a shows the simulated sample at several stages in time. The red domains in the first image grow with constant growth rate (1 pixel/step), while new red domains nucleate during growth.

If we plot the area of red phase verus time we find the typical S-shape (Figure 4.2b). From a plot of the new phase fraction versus time according to Equation 4.10, we obtain $n = 2.7$, as shown in Figure 4.2c.

From this example, we observe that n need not be an integer value and depends on how the nucleation and growth rates vary with time. The above derivation of the JMAK equation allows us to interpret the kinetics of the transformation of Mg to MgH_2 in thin films. Here we take explicitely Christian's warning into account that:[95] "...a kinetic investigation which is limited to the establishment of the value of n...does not give sufficient information for the growth habit to be deduced."

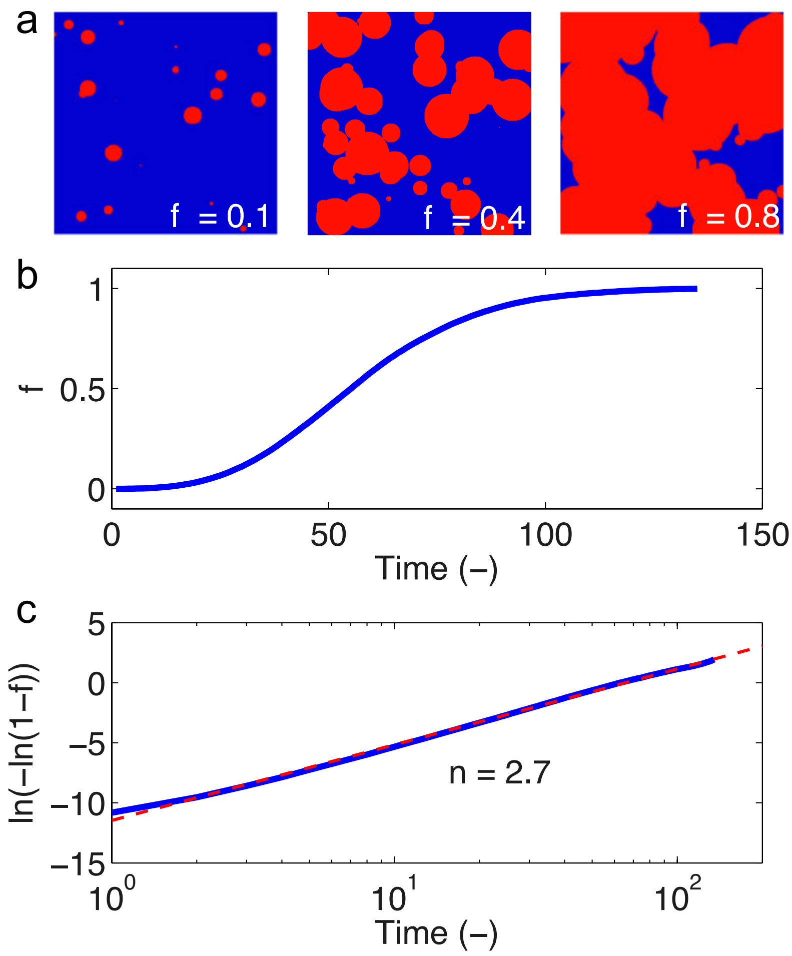

Figure 4.2 A simple nucleation and growth simulation that shows a non integer n, with (a) the simulation at $t = 30$, $t = 40$ and $t = 80$ respectively, (b) the new (β-phase) fraction f versus time and (c) the phase fraction f plotted to obtain n as the slope using Equation 4.10.

4.4 JMAK analysis of hydrogen ab- and desorption

Using the JMAK model, we now investigate the kinetics of hydrogen absorption in a thin Mg film at the two experimental conditions: one at “low” hydrogen pressure (70 Pa, small number of nuclei) and one at “high” pressure (100 Pa, large number of nuclei). Furthermore, we will investigate the kinetics of desorption and try to obtain an indication of the nucleation and growth mechanism involved in that process.

We first analyze the MgH_2 nucleation rate in the low-pressure absorption experiment to see whether the use of Avrami nucleation—*i.e.* a decreasing nucleation rate (Equation 4.6)—in the JMAK model is indeed a fair assumption.

4.4.1 Absorption

Nucleation rate

The derivation of the JMAK model for thin films is based on the assumption that the nucleation rate is a decreasing function of time because there is a limited amount of available nucleation sites. Because we have already observed that nucleation occurs at preferential sites,[105] such a behavior is expected. In order to find whether the nucleation rate indeed follows this mechanism—*i.e.* Avrami nucleation—we have manually counted the number of nuclei versus time in the low-pressure hydrogenation experiment. Images of a 10 nm Mg sample were recorded every 10 minutes for the total duration of 140 hours at a hydrogen pressure of 70 Pa—a movie of this hydrogenation can be found online.[105]

Figure 4.3 shows that the nucleation rate indeed decreases with time until finally 89 nuclei have appeared. The dashed line is a least-squares fit using the equation for Avrami nucleation (Equation 4.6). We have to realize, however, that here we (logically) can not count phantom nuclei. Therefore, the fit does not give the actual values of the Avrami nucleation parameters (ν and N_0) that are in the JMAK model, but lower values. The derivative of the data in Figure 4.3 is therefore the nucleation rate that is lowered by impingement.

What we do observe, however, is that the nucleate rate decreases much quicker than we would expect from impingement. The black line in Figure 4.3 is a line to guide the eye; after about 10 hours the nucleation rate is already dropping. This drop in nucleation rate is unlikely to come from impingement alone: The fraction of MgH_2 in Figure 4.1b is still rather low after 25 hours ($f < 0.1$), while the nucleation rate has decreased by about 50%.

We believe that the above gives sufficient evidence to allow us to say that Avrami nucleation is the governing mechanism for our thin Mg layers. Hence, we expect $0 < n_n < 1$.

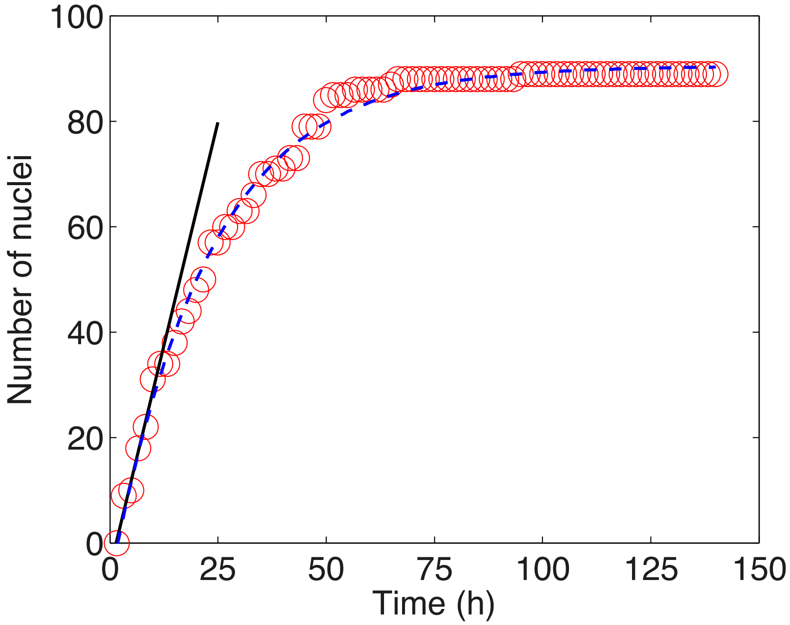

Figure 4.3 Number of nuclei versus time at low hydrogen pressure ($p_{H_2} = 70$ Pa). The nuclei are hand counted. The blue dashed line is a least squares fit with the equation for Avrami nucleation (Equation 4.6), with $R^2 = 0.99$. The black line is a line to indicate that the nucleation rate quickly declines.

Low H_2 pressure: small number of nuclei

Figure 4.1b shows the optical transmission of a thin film sample after 25 h and 75 h at 70 Pa H_2 (low-pressure), where it is clear that the hydride domains (high transmission) grow 2-dimensionally. Hence, given that the growth velocity is constant,[105] we know *a priori* that the growth component n_g of the growth dimension n is equal to 2. We now analyze the transmission data of this sample with the JMAK model to see whether we find the expected value for n, $2 < n < 3$.

To measure the kinetics of the phase transformation process, we calculate the fraction of hydride phase from the average transmission data, shown in Figure 4.4a. The hydride fraction is then converted to $\ln(-\ln(1-f))$ to obtain growth dimension n (Equation 4.10), as is shown in Figure 4.4b. This plot reveals that there are three regimes with different growth dimensions. In region A, up to $t = 2.8$ h, we find a low value of $n = 0.3$. We believe that this period represents an incubation time. Indeed, it takes 6.7 h before we can distinguish four nuclei. Moreover, the spread in the data at these low hydride phase fractions is quite large, hence the fit contains a large error.

More interestingly, in region B we find $n = 2.2$. With $n = n_g + n_n$, this can be related to the observed 2-dimensional growth (making $n_g = 2$), plus a nucleation component ($n_n = 0.2$). Indeed, we observe that during this period many nuclei are still being formed with a decreasing rate with time (as concluded from Figure 4.3), which explains that $0 < n_n < 1$.

In region C, which starts at $t = 72$ h, the growth dimension lowers somewhat ($n = 1.6$). In fact, the occurence of two slopes in the JMAK analysis is expected from theory when site saturation occurs.[95] Site saturation indicates the moment when all the available nucleation sites have nucleated. Hence, after this point the transformation occurs only via growth.

Indeed, the start of region C coincides with the point where hardly any nucleus appears anymore (only 1 nucleus appears after 72 hours), which can be seen in Figure 4.3. Therefore, from theory, we should ascribe the growth dimension in region C ($n = 1.6$) solely to the growth process, which makes $n_g = 1.6$. This of course raises the question why n_g is not equal to 2 in region C, as we would expect for 2D-growth.

We believe the answer lies in a change in the growth dimensionality. In Figure 4.1b, after 75 h many hydride domains that were separately growing are now fusing into roughly three large domains. In our previous study we found that when two (or more) domains grow into each other, the cusp (region with a negative curvature) that is formed between the two domains grows with a larger velocity. This increase in growth velocity scales with the inverse curvature and originates from the edge boundary energy. To minimize the total edge energy, the system minimizes its total edge length. In the three large domains, many smaller domains have fused and are thereafter minimizing their edge length by blunting the formed cusps. Hence, the growth becomes more 1-dimensional in nature because the circular shape of the

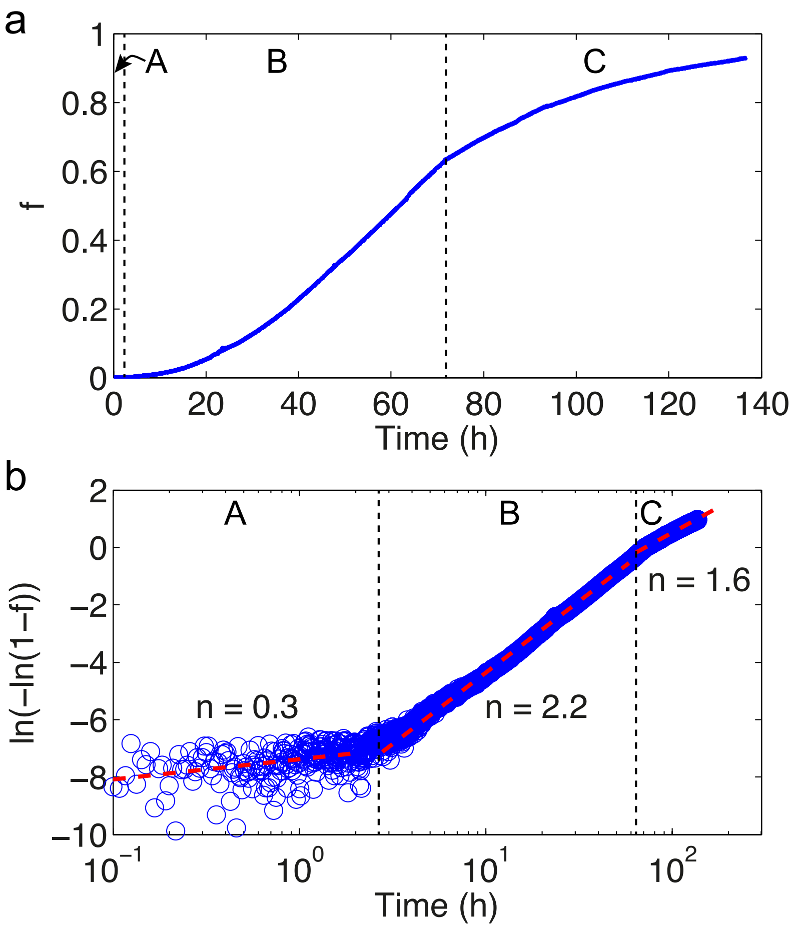

Figure 4.4 (a) Transmission data converted to fraction versus time and (b) the JMAK analysis. Least-squares fits are indicated with red dashed lines. Three regions can be distinguished, (A) with a low growth dimension, (B) a growth dimension indicating 2D-growth and (C) a leveling off to lower growth dimension because of non-random impingement.

domains is lost.

Hence, in summary, even though in this experiment the nucleation sites are not randomly distributed across the sample volume, we may still use the JMAK analysis to obtain the growth mechanism—at least when the fraction of transformed phase is smaller than about 0.5. At larger fractions, the effects of the low number of nuclei become dominant. The non-random distribution of nuclei causes a lowering of the growth dimension due to (non-random) impingement and blunting of the domain edges.

High H_2 pressure: large number of nuclei

We now apply the analysis of the low-pressure (low number of nuclei) data to the high-pressure data. In this case, the transition to MgH_2 is much faster and is completed within two hours. Here we could not identify nucleation and growth features such as in Figure 4.1b. To deduce whether still the same 2D-growth mechanism is responsible for the hydride formation, we measured the change in optical transmission of the 10 nm Mg layer exposed to hydrogen with $p_{H_2} = 100$ Pa.

Figure 4.5a shows the hydride phase fraction versus time. The fraction is again converted to $\ln(-\ln(1-f))$ to obtain the growth dimension n, shown in Figure 4.5b. Again we discover three different slopes. In region A ($t < 200$ s) only three datapoints are obtained, too little for a meaningful discussion. After approximately 200 s, the slope quickly converges to $n = 2.0$ (region B, $t > 200$ s). In region C, the transformation is complete at $f = 1$ and therefore $n = 0$.

Hence, given that $n = 2$, it is likely that also at this higher pressure (larger driving force), the hydride phase domains again grow 2-dimensionally. This implies, however, that $n_n = 0$—with Equation 4.8: $n_n = n - n_g = 2 - 2 = 0$. For n_n to be zero, the nucleation must occur instantly after the hydrogen pressure is applied and thereafter the nucleation rate is zero. Then, during the transformation, there is only growth of these (now more numerous) nuclei.

The large difference in nucleation rate between the low- and high-pressure experiment can be understood in terms of an energy landscape for nucleation.[109] The illustration in Figure 4.6 is an artist impression of the hypothetical energy of preferential nucleation sites (energy minima) in the low-pressure (red) and high-pressure (blue) experiment. In the low-pressure experiment, few sites are available—in the illustration there are a total of three sites. There furthermore is an activation barrier for nucleation—not drawn in Figure 4.6—which lowers the nucleation rate.

When a high pressure is applied, all of the sites have a low enough energy to allow for nucleation. Furthermore, the large driving force ensures a high nucleation rate. In general, the nucleation rate N is proportional to:[110]

$$N \propto \exp\left(-\frac{E_a}{RT}\right)\exp\left(-\frac{\Delta E}{RT}\right)$$

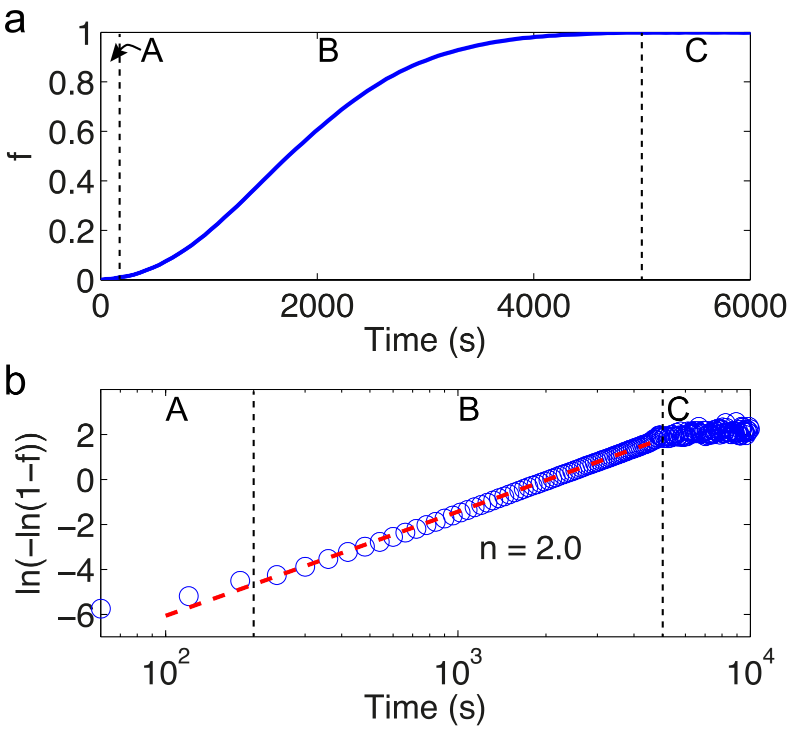

Figure 4.5 Hydrogen absorption data at high pressure ($p_{H_2} = 100$ Pa, $T = 363$ K) converted to (a) the β-phase fraction versus time and (b) the JMAK analysis with $\ln(-\ln(1-f))$ (Equation 4.10). Three regions are distinguished, with region A having too few data points to determine n, while in region B n converges to 2.0. In region C the transformation is complete, hence $f = 1$ and $n = 0$.

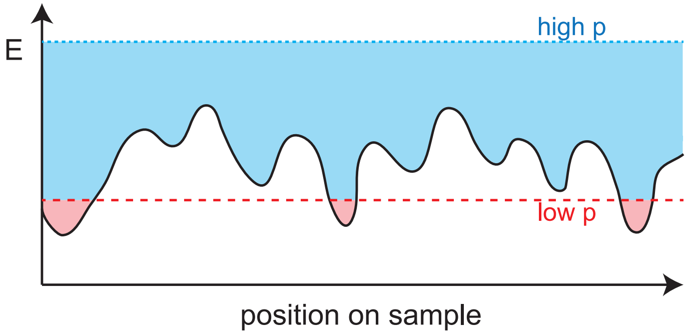

Figure 4.6 The hypothetical energy landscape for nucleation. The minima are the sites where nucleation is possible. At low pressure (red) only few sites are available, while at high pressure (blue) all of the sites are available for nucleation. In both cases there is an activation energy for nucleation that is not taken into account in the drawing.

where E_a is the activation energy for nucleation and ΔE the driving force. In these experiments, ΔE is proportional to $\ln \frac{p^{appl}}{\overrightarrow{p}}$, with p^{appl} the applied hydrogen pressure and $\overrightarrow{p}$ the absorption plateau pressure (*i.e.* the pressure where the hydrogenation rate is zero, for further details see ref. 10).

A variation in nucleation energy between sites commonly occurs in solid state phase transformations. For example, nucleation at grain boundaries (or interphase boundary) is easier than nucleation at a stacking fault, which is in turn easier than nucleation at a vacancy.[110] Moreover, the nucleation rate is highly sensitive to the driving force. Given the large driving force for nucleation at high pressure and the observed 2D-growth at low pressure, we infer that a combination of instant nucleation and subsequent 2D-growth represents the growth mechanism at high pressure.

4.4.2 Desorption

We did not observe any visual evidence for nucleation of Mg in MgH_2 at any undersaturation. In the 10 nm Mg layers the desorption always takes place at the same pressure and we never observed individual Mg islands nucleating in MgH_2. Combining our optical measurements with a JMAK analysis, we hope to find an explanation for the asymmetry in the behaviour of Mg during hydrogen absorption and desorption.

From the optical transmission data recorded during a typical desorption experiment performed at $p_{H_2} = 8$ Pa, we obtain the fraction of the new phase as a function of time. In this case, f is the fraction of the Mg α-phase (Figure 4.7a). From the fraction we calculate $\ln(-\ln(1-f))$ to obtain n from the slope versus $\ln t$, as shown in Figure 4.7b. This reveals three regimes.

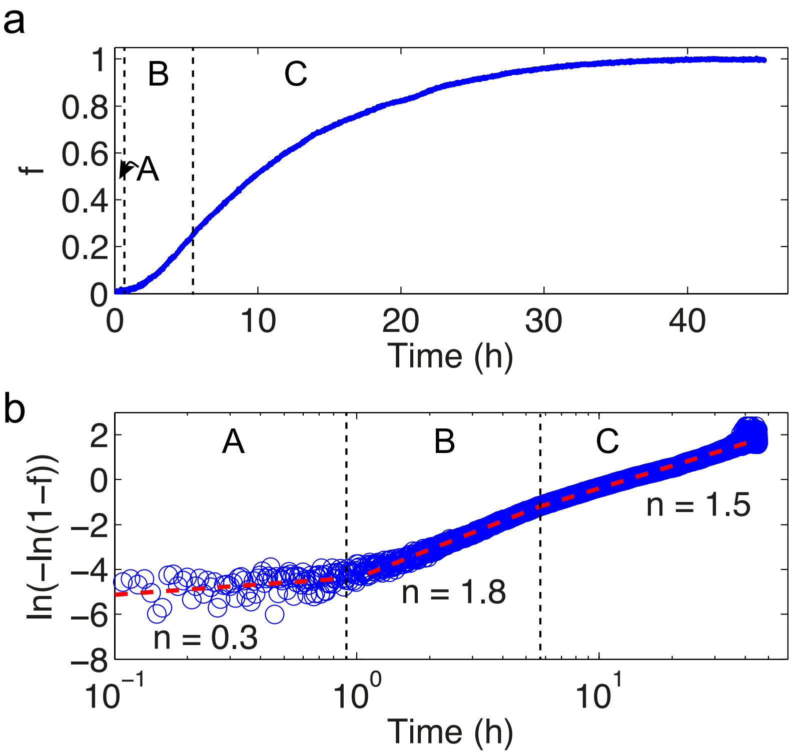

Figure 4.7 Hydrogen desorption data at high pressure ($p_{H_2} = 8$ Pa, $T = 363$ K) converted to (a) the α-phase fraction versus time and (b) the JMAK analysis with $\ln(-\ln(1-f))$ (Equation 4.10). Three regions can be distinguished. In region A $n = 0.3$. In region B n is to 1.8 and finally, in region C, $n = 1.5$.

Region A covers the very first fraction of the total transformation, with an n of 0.3. Similar to the absorption at low pressure, we do not conclude anything about the mechanism in this region, given the spread in the data. Region B has a roughly constant growth dimension of 1.8, while in region C it lowers to 1.5. Hence, as in the absorption experiments we again find three distinct growth regimes (Figure 4.4). However, the exponents of region B and C are clearly below 2, suggesting a 1-dimensional component in the growth of the Mg phase in the MgH_2 matrix. In order to understand this we revert to our optical observations, in particular on the hysteresis.

The investigation of the hysteresis, is schematically summarized in Figure 4.8. The full isotherm (blue) starts at low pressure (bottom-left). After a gradual increase in hydrogen pressure, the hydrogenation starts at point 1. The full hydrogenation is then completed at point 2. Now, to start the desorption, the pressure is lowered. At point 3 the dehydrogenation (Mg formation) begins, which completes at point 4.

In contrast to the full isotherm, a hysteresis scan (red) reveals that the hydrogenation proceeds at lower pressure if MgH_2 nuclei are already present. The hysteresis scan is performed as follows: At point a, the hydrogen pressure is quickly lowered, preventing the sample to fully hydrogenate to MgH_2. When point b is reached the desorption starts, at roughly the same pressure as point 3 (the desorption pressure of the full isotherm). At point c, the desorption is not allowed to continue and the pressure is again increased. We observe that the rehydrogenation now begins at point d, at a much lower pressure than in the full isotherm. Moreover, the hydrogenation proceeds very quickly (within 10 minutes) between d and e, while it takes approximately 11 hours to complete the full hydrogenation at point f.

The above behaviour is in accordance with our observation that in the region between $\overrightarrow{p}$ and p^{nucl} the observation of growth nuclei can be induced. Nucleation occurs at an appreciable rate at p^{nucl}, below this pressure, the rate quickly drops. The growth of individual nuclei is most easily observed at (or slightly above) $\overrightarrow{p}$. In desorption, however, we find no evidence for such a nucleation behavior. Just above $\overleftarrow{p}$, no dehydrogenation is observed, even after waiting for several days. Only at a hydrogen pressure lower than or equal to about 10 Pa, the dehydrogenation process begins. No indication for the formation of metallic Mg islands was ever observed. The dehydrogenation proceeds via a gradual decrease in the optical transmission of the Mg thin film, whatever the underpressure.

We do, however, observe a memory effect: the nucleation and growth image, which fades away on desorption from b onwards, is quickly recovered on hydrogenation, even after desorption to point 4.[105] This fast recovery is in accordance with the fast overall increase in transmission between d and e. The recovery of the nucleation and growth image is only possible on immediate rehydrogenation and points to a slow component in the desorption process which is not optically visible.

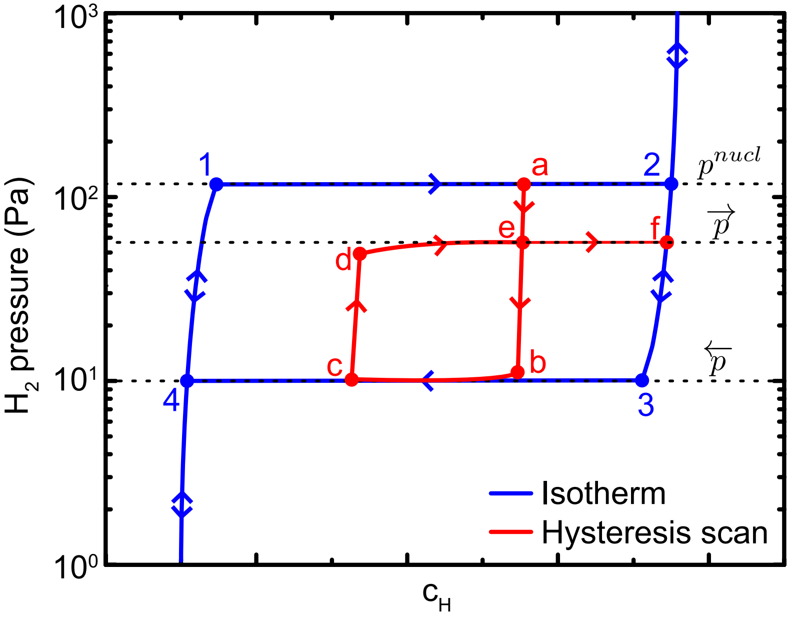

Figure 4.8 Schematic summary of our previous findings on the hysteresis of 10 nm Mg layers. The full isotherm (blue) shows the hydrogenation process starting from 100% Mg to 100% MgH_2. The hysteresis scan (red) is started at a partial transformation to MgH_2 (point a). Desorption starts at the same pressure as in the full isotherm (point b), while (re-)hydrogenation now begins at a lower pressure (point d). Finally at the same pressure the sample can be completely hydrogenated (point f). The pressure at point 1 is labeled p^{nucl}, because at this pressure the nucleation rate is large enough to achieve an appreciable rate of transformation to MgH_2. If nuclei are already present, the hydrogenation occurs at the lower pressure labeled $\overrightarrow{p}$, the absorption plateau pressure. The desorption always starts at about 10 Pa, hence this desorption plateau pressure is labeled $\overleftarrow{p}$.

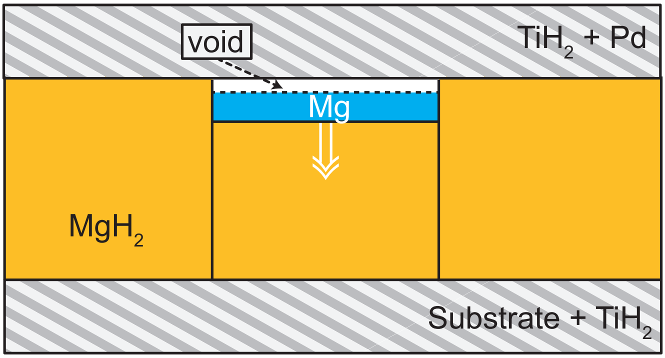

Figure 4.9 Magnesium nucleation and growth likely occurs with the formation of voids, because it contracts compared to the surrounding MgH_2. The initial stages might proceed via the formation of thin Mg discs. Such a mechanism limits the strain while also limiting the surface area exposed to voids. The vertical lines represent the grain boundaries in MgH_2.

We propose that this asymmetry in the nucleation and growth is related to the asymmetry of the plastic deformation process. During hydrogen absorption, the expanded MgH_2 can only form by plastic deformation of the TiH_2 and Pd layers (as in Figure 4.1a). During desorption, however, the Mg volume is reduced compared to MgH_2 and therefore (as an alternative to plastic deformation) the Mg may disengage from its surroundings at the expense of creating more surface area. This suggests that, at least temporarily, porous Mg is formed upon hydrogen desorption. A drawing of what a partially desorbed MgH_2 layer may look like is shown in Figure 4.9. The formation of porous Mg after dehydrogenation has indeed been observed in the literature.[91]

The memory effect described above suggests that the structural relaxation is a seperate process that occurs on a larger timescale than the desorption of hydrogen. If one rehydrogenates quickly enough, the film would still be porous and experience a much smaller barier for the nucleation of MgH_2 since the required amount of plastic deformation would be much less. This would explain the fast recovery of the MgH_2 growth islands.

To further analyse the desorption we followed the dissolution of the growth nuclei upon reducing the hydrogen pressure. Figure 4.10 shows the optical transmission profile of an MgH_2 island as a function of time, where the position indicates the number of pixels from the middle of the island. We observe that the size of the island is reduced, while simultaneously the overal transmission decreases on dehydrogenation. We conclude that the transformation to the Mg phase proceeds both from the edges as well as from within the growth island. This suggests that the nucleation barrier for the Mg formation is much smaller than for MgH_2. Indeed, in the absence

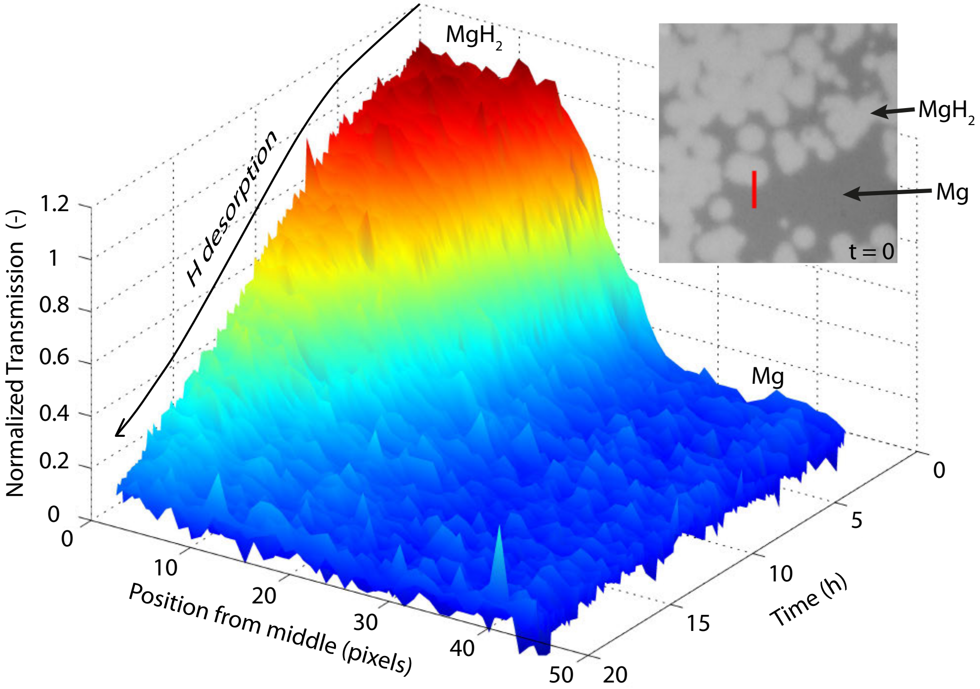

Figure 4.10 A 3D representation of the optical transmission along the red linescan indicated in the inset. Desorption of hydrogen occurs along the whole linescan. The hydrogen desorption of the middle of the MgH_2 domain (position = 0) is indicated by the curved, black arrow.

of plastic deformation the critical nucleus size is expected to be orders of magnitude smaller. As we have shown in ref. 10, the plastic deformation energy term is several orders of magnitude larger than a typical surface energy.

Let us now consider the relation between these observations and the JMAK analysis of Figure 4.7. Since the MgH_2 films are nanocrystalline with crystallite sizes of the order of the film thickness (10nm), we propose that these crystallites nucleate independently. Due to their preferential orientation the volume change is mainly perpendicular to the substrate and the largest barrier will be the breaking of the bonds with the surrounding TiH_2 layers, creating a small void.

The critical nucleus for the formation of Mg will depend on the energy of the interface bonds, which allows for a much smaller critical nucleus size. Once the interface bonds are broken, the growth may proceed vertically. The grain boundaries provide a natural limitation for the lateral extend of the nucleus. They allow for an easy rearrangement to accomodate the mismatch between Mg and a neighbouring

MgH_2. Thus, the nucleation may proceed largely independently, without the need for the existence of preferential nucleation sites. Nevertheless, we expect an increased change for neighbouring crystallites to nucleate, since some of the bonds with the Mg had to be broken in orde to form the void. In addition the void will exert some stress to neighbouring islands.

From a JMAK point of view, growth of Mg perpendicular to the substrate translates to a one-dimensional growth process, which means that $n_g = 1$. Should the nucleation events again follow Avrami nucleation (decreasing nucleation rate with time), then $n_n < 1$. Hence, with $n = n_g + n_n$, in this case $1 < n < 2$, which is what we observe in Figure 4.7. The real mechanism is, however, likely to be more complex. For example, we do not take diffusion problems into account, which may perhaps be expected to play a role in the case of out-of-plane (1D) growth of Mg from MgH_2. In addition, because in-plane neighbours will always influence each other, we should expect 2D-growth to some extent. Taking all these possibilities into account is beyond the scope of the JMAK analysis performed in this work.

In summary, the interpretion of the JMAK analysis in Figure 4.7 is not straightforward. However, combining all our observations, we conclude that (at least temporarily) porous Mg is formed upon desorption. This is possible because plastic deformation involves a large amount of energy as compared to bond breaking. The nucleation and growth behavior on hydrogenation and dehydrogenation is asymmetric, because only on desorption void formation provides an alternative pathway.

4.5 Conclusion

From the low-pressure hydrogenation of 10 nm Mg layers with a low nucleus density we conclude that JMAK can be succesfully used to analyze the nucleation and growth mechanism. The mechanism, which we observed optically *a priori*, begins with nucleation at preferential sites with a decreasing rate. After having nucleated, the magnesium hydride domains grow two-dimensionally. A JMAK analysis of the hydrogenation at higher pressure—where we are unable to optically verify the nucleation and growth mechanism—reveals that the growth of the MgH_2 domains is again of two dimensional nature, albeit with a much higher nucleation rate.

The dehydrogenation is not simply the reverse of the absorption mechanism. In this case, we find evidence that the nucleation of Mg is a fast process. Based on the observation that previously hydrogenated regions of the Mg film can be rehydrogenated very quickly, we propose that the formation of Mg within MgH_2 occurs along with the formation of voids. Creating a new surface/interface (~ 1 J/m^2) is an energetically more favorable process than mechanical deformation of the multilayer ($\sim 10^3$ J/m^2). Without providing a detailed analysis, we note that hydrogen actually favours the creation of seperate interfaces because hydrogen acts as a defactant.[111] The

JMAK analysis is not easily interpreted, but suggests that the initial stages of Mg formation occurs via thin discs with a minimum size equal to the crystallite width.

The asymmetry between the ab- and desorption processes is important to consider in all nanoconfined metalhydride systems with a large volume contraction during desorption of hydrogen. Hence, also when analyzing the phase transition in a 3D confined nanoparticle system, the large asymmetry in the mechanics of expansion and contraction processes should be taken into consideration.

Chapter 5

Hydrogenation of Mg/Pd alloys and multilayers

5.1 Introduction

Thin film metal hydrides are interesting platforms to study the interaction of hydrogen in metals, and formation of metal hydride phases.[112] In many metals, there is a large change in the optical properties upon hydrogen absorption. The optical technique Hydrogenography uses the changing optical properties of thin film metals and multilayers to study hydrogen storage and sensor materials.[47] This combinatorial technique allows one to scan, for instance, ternary alloys for metal hydrides for compositions with suitable thermodynamic properties. To be able to extrapolate the results of thin film and multilayer studies to the bulk or nanoparticle equivalents, it is important to take into account the effect of the substrate and interfacing materials on the hydrogenation thermodynamics and kinetics.[62, 61]

These effects are potentially large, especially in palladium-capped magnesium thin films. Such films were shown by Baldi *et al.*[58] to have an increased hydrogen absorption pressure with decreasing thickness. The logarithm of the absorption plateau pressure increases proportionally to $1/d_{Mg}$, with d_{Mg} the Mg layer thickness. The authors (some of whom are involved in the making of this chapter) explained this behavior by the effect of elastic clamping of the magnesium by a Mg-Pd interface alloy. Elastic clamping would result in higher absorption pressures because of the H-H interaction, which effectively causes a compressive stress in case the host lattice is not free to expand. In magnesium films without a Mg/Pd interface, but with a protective Ti layer in between, there is no interface alloy. In this case, the hydrogen absorption pressure increase is negligible for the same Mg thickness range.

Recently, however, Chung *et al.* [64] argued that in Pd-capped Mg films the elastic clamping model does not explain the large absorption pressure increase. They do however, confirm the presence of an interfacial alloy layer of about 2 nm in thickness. The authors propose a new model for the increase in absorption pressure (or MgH_2 destabilization) by considering the enthalpy of Mg-Pd alloy formation. Simply put, Chung *et al.* claim that Mg in the MgPd alloy is stabilized with respect to its elemen-

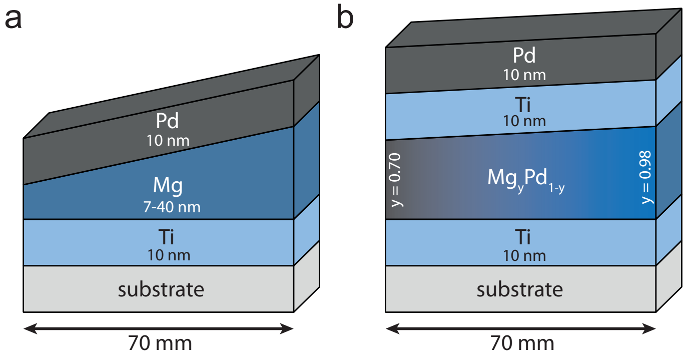

Figure 5.1 Sample geometries

tal form. Therefore the transformation of this alloy to the MgH_2 phase has a lower enthalpy of formation. To explain the plateau pressure dependence on $1/d_{Mg}$, they average the enthalpy of interface alloy formation over the total Mg layer thickness. Hence, in their model, the average ΔH for the hydrogenation of the whole layer will change proportional to $1/d_{Mg}$. They propose the reversible concomitant reaction pathway:

$$\left(\frac{1}{1-y}\right)\mathrm{Mg}_{1-y}\mathrm{Pd}_y + \mathrm{H}_2 \leftrightarrow \mathrm{MgH}_2 + \left(\frac{y}{1-y}\right)\mathrm{Pd} \tag{5.1}$$

with y the atomic fraction of Pd within a single layer. However, the model of Chung *et al*. is not consistent. There is no reason why the presence of an interface alloy of 2-3 nm on top would destabilize the whole, say, 40 nm pure Mg layer that lies below. The hydride formation enthalpy of the pure Mg remains the same. Furthermore, the reversibility of the reaction pathway implies that the effect on the plateau pressures should also hold for hydrogen desorption. The same argument holds for the elastic clamping model. Both models are symmetric regarding ab- and desorption.

The elastic clamping model furthermore predicts that a change in the Pd layer thickness would affect the hydrogen sorption thermodynamics of Mg. In turn, the Pd layer itself should be affected by the clamping of the Mg layer. We find no evidence for these two effects from experiments (not shown in this chapter), thereby making it unlikely that the elastic clamping model provides a proper description of the hydrogen sorption characteristics of Pd-capped Mg layers.

In this chapter, we study the hydrogenation of Pd-capped Mg layers in more detail, including a detailed investigation of the crystal structure and microstructure of these films and an analysis of the desorption behavior. We use thin film Mg gradients to minimize the sample-to-sample variability, as shown in Figure 5.1a. We find a remarkable similarity when we compare the Pd-capped Mg data with those obtained from $Mg_{1-y}Pd_y$-alloy layers, prepared by co-sputtering of Mg and Pd (Figure 5.1b).

While both models discussed so far imply a symmetry between loading and unloading, the dehydrogenation appears to be unaffected by the thickness of the Magnesium layers. Hence, both the elastic clamping and the model of Chung *et al.*[64] (the enthalpy model) can not explain the hydrogen sorption thermodynamics. We find that the relation between the microstructure and hydrogen sorption characteristics of both types of samples is very complex. Although we do not fully understand the implications for the Pd-capped Mg and Mg-Pd alloy systems, we propose a qualitative model that takes the effects of nucleation and plastic deformation into account.

5.2 Experimental

Both the multilayer and alloy multilayer samples are deposited in an ultra-high vacuum dc/rf magnetron sputtering system (base pressure 10^{-7} Pa) using Mg (99.95%), Ti (99.999%), and Pd (99.98%) targets in an argon atmosphere (6N purity, pressure 3 Pa), with all substrates kept at room temperature. In all samples, first a 10 nm Ti layer is deposited that serves as a sticking layer and furthermore results in the deposition of flat Mg layers. The Pd-capped, gradient Mg samples are sputtered with a gradient in the Mg thickness along the long edge of 70x5 mm quartz wafer substrates. The resulting Mg wedge has a thickness that ranges from 7 to 40 nm. The Mg_yPd_{1-y} alloy layers ($y = 1.7 - 30\%$) were deposited on the same substrates, but now Mg and Pd are co-sputtered. The resulting alloy layer has a variable thickness because of the difference in total deposition rate along the 70 mm sample, due to the difference in molar volumes of Mg ($V_{Mg} = 13.97\ ^{\mathrm{cm}^3}/_{\mathrm{mol}}$) and Pd ($V_{Pd} = 8.85\ ^{\mathrm{cm}^3}/_{\mathrm{mol}}$). The alloy layer is capped by a 10 nm Ti layer to avoid an additional alloying effect with the 10 nm Pd-capping layer.

Samples for TEM analysis (JEOL 2010F) are deposited on silicon nitride windows (10 nm, 3x3 window array, TEMwindows.com) and all contain uniform layers, *i.e.* a 50 nm Mg layer in the Pd-capped sample and a single Mg_yPd_{1-y} alloy (thickness 50 nm) composition $y = 0.90$ in the alloy sample. In this case the Ti and Pd capping layers are all 3 nm thick, to make sure that the Mg(Pd) layer are primarily visible in the images.

The hydrogen sorption thermodynamics are measured with Hydrogenography, which records the change in optical transmission as a function of the hydrogen pressure and temperature.[113] The technique consists of a stainless steel hydrogenation cell ($p_{H_2} = 10^1 - 10^6$ Pa, 20 sccm), which is placed in a furnace (here 333 K and 363 K). Hydrogen-argon mixtures (0.1% H_2, 4% H_2) and 100% hydrogen are used. The transmission data are recorded with a 3-CCD camera (Sony).

X-ray diffraction (XRD) is measured in a θ-2θ configuration with a Bruker D8 Discover diffractometer (Cu Kα, $\lambda = 1.5418$ Å). A two-dimensional detector collects real-time data over a large area with high sensitivity and low background. A beryllium dome allows *in situ* diffraction measurements during hydrogenation/dehydrogenation of the films in hydrogen pressures up to 10^5 Pa and temperatures between room temperature and 473 K. The source is equipped with a collimator that results in an illuminated sample area of about 10x1 mm, depending on angle θ.

5.3 Results

5.3.1 Pd-capped Mg-wedge multilayers

In our previous experiments, five different Mg thicknesses were studied in the Pd-capped Mg samples. In this chapter, Mg-wedge samples (Figure 5.1a) provide multiple Mg thicknesses on one sample, which allows us to measure XRD and the hydrogen sorption thermodynamics as a function of the magnesium layer thickness. We furthermore analyze uniform Mg layers deposited on silicon nitride windows with TEM, with the samples both in the as-deposited state and cycled with hydrogen.

X-ray diffraction

XRD-spectra of several thicknesses of as-deposited Pd-capped Mg are shown in Figure 5.2. The hcp-Ti (002) and fcc-Pd (111) reflections are found at $2\theta \approx 38.2^\circ$ and 40.0° respectively. There is a slight shift to lower angles compared to the 2θ values expected for the equivalent bulk materials ($\theta_{Ti}^{002} = 38.4^\circ$ and $\theta_{Pd}^{111} = 40.17^\circ$), which we ascribe to residual tensile strain in the out-of-plane direction due to deposition. The Ti and Pd reflections perfectly overlap for the different Mg thicknesses.

The hcp-Mg (002) plane diffracts around $2\theta = 34.4$. In the figure, the vertical dashed line indicates the peak position of bulk hcp Mg (002) at $2\theta = 34.43^\circ$. All the diffractograms are asymmetric because of a shoulder at $2\theta = 35^\circ$, although the intensity of this shoulder is very low compared to the main peak for thick Mg. With decreasing thickness, however, the main peak intensity decreases and the relative size of the shoulder thereby increases. The intensity of the shoulder is constant with Mg thickness, which indicates that this shoulder originates from the interface MgPd alloy, which has a constant thickness (~ 6 nm)[58]. However, the measured intensities are too low to properly fit the position of the interface alloy.

TEM

We deposited several multilayers on Si_3N_4 windows to look at the multilayers in planar view with TEM. In these samples, the Ti thickness is 2 nm and the Pd thickness is either 3 or 5 nm. These thicknesses are lower than in the samples used for hydrogenation experiments to make sure that the Ti and Pd have only a small effect

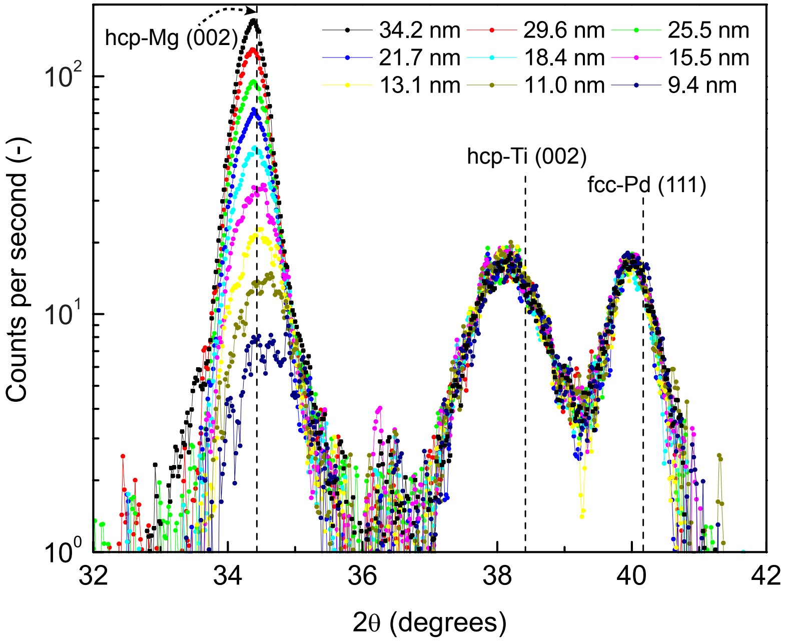

Figure 5.2 XRD spectra of several thickness along the 7 cm long Pd-capped Mg-wedge. The two peaks on the right are reflections of the Pd (111) and Ti (002) planes. The interface alloy causes the peak to shift to higher angles at lower thicknesses, because its contribution becomes larger compared to the contribution of the non-alloyed Mg.

on the diffraction image as compared to Mg. Two Pd-capped Mg samples (20 nm Mg and 50 nm Mg) are compared to Ti-sandwiched Mg (*i.e.* Mg not in contact with Pd). We know from earlier work that Ti-sandwiched Mg is very stable and can be cycled with hydrogen many times. Figure 5.3a shows a typical image of deposited Ti-sandwiched 50 nm Mg (Ti/Mg), which reveals its polycrystalline hexagonal nature and an average grain size of around 50 nm (grain size $\approx$ layer thickness). Upon cycling with hydrogen five times (Figure 5.3b), the grains have grown slightly but with an intact grain structure remaining. The Selected Area Electron Diffraction (SAED) patterns (Figure 5.4a and b) confirm this interpretation. In both the as-deposited and cycled states, three diffraction rings are observed at the same positions, as indicated by the dashed lines. We assign the diffraction rings to hcp-Mg (010), (110) and (020) respectively from large to small d-spacing.

We now compare the Ti/Mg sample to Pd-capped 20 nm Mg (Pd/Mg 20 nm), which is shown in the as-deposited state in Figure 5.3c. The grain size is again roughly equal to the layer thickness. Upon hydrogenation, however, the grains appear to become smaller, as can be seen in Figure 5.3d. Even at an increased magnification (Figure 5.3e), it is difficult to observe the grains. Furthermore, the SAED patterns (Figure 5.4c and d) reveal that in both the as-deposited and cycled samples there is a diffraction ring which is not present in the Ti/Mg sample. The d-spacing of this diffraction ring is 0.225 nm, which is not readily assigned to any present phase. Hence, the MgPd alloy at the interface may be the origin of this diffraction ring. The d-spacing is not the same as for the shoulder found in the XRD patterns at $2\theta = 35°$, which has a d-spacing of 0.25(6) nm.Upon cycling with hydrogen, the 20 nm Mg sample becomes (electron) amorphous, with only the single amorphous ring remaining.

This behavior depends on the Mg thickness. A 50 nm Pd-capped Mg layer is still crystalline after cycling (Figure 5.3f). The SAED pattern in Figure 5.4e clearly shows crystalline Mg. Compared to Ti/Mg, however, now there are many more diffraction rings, which indicates that the hcp-Mg (002) texture of the as-deposited state is lost upon cycling with hydrogen.

Remarkably, in both TEM images in Figure 5.3e and f of the Pd-capped 20 and 50 nm samples, we observe the formation of voids after cycling with hydrogen. The red arrows point at some of these voids. In the 20 nm Mg sample, the voids are roughly spherical in shape, and smaller than 5 nm in diameter. The voids in the 50 nm Mg, however, are roughly the size of grains (up to 100 nm in diameter). It is unclear whether these voids span the whole thickness of the Mg layer or just a fraction. Dura *et al.* [91] observe a porous Mg layer after dehydrogenation of 100 nm Pd-capped epitaxial Mg layers. Hence, we now confirm this observation with this TEM investigation.

We conclude that the hydrogenation/dehydrogenation of Pd-capped Mg films re-

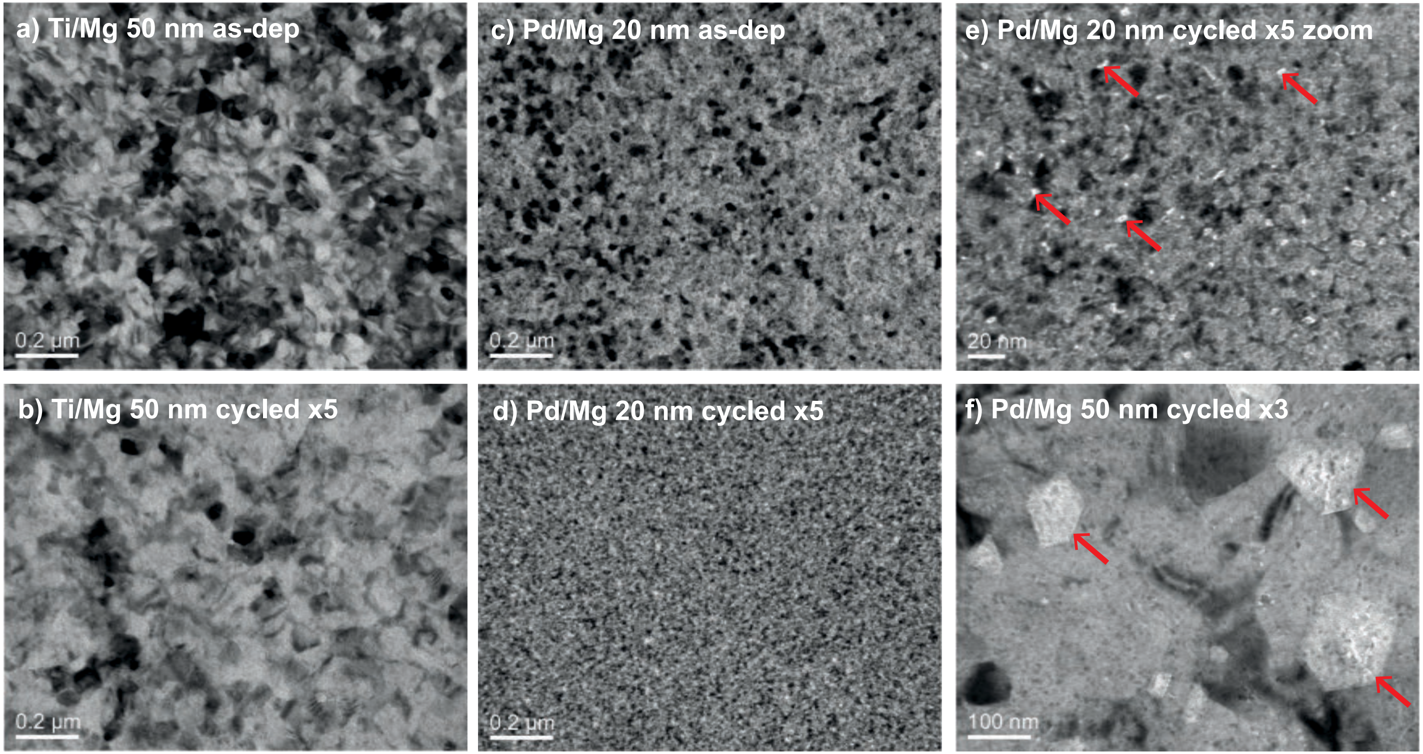
a) Ti/Mg 50 nm as-dep
0.2 µm
c) Pd/Mg 20 nm as-dep
0.2 µm
e) Pd/Mg 20 nm cycled x5 zoom
20 nm
b) Ti/Mg 50 nm cycled x5
0.2 µm
d) Pd/Mg 20 nm cycled x5
0.2 µm
f) Pd/Mg 50 nm cycled x3
100 nm

Figure 5.3 Planar view TEM images of (a) as-deposited Ti-sandwiched Mg (Si_3N_4 / Ti 2 nm / Mg 50 nm / Ti 2 nm / Pd 3 nm), (b) same cycled five times with hydrogen, (c) as-deposited Pd-capped Mg (Si_3N_4 / Ti 2 nm / Mg 20 nm / Pd 5 nm), (d) same cycled five times with hydrogen, (e) same zoomed in and (f) Pd-capped 50 nm Mg cycled x5. The Pd-capped 20 nm sample loses its crystallinity, while the Ti-sandwiched Mg stays crystalline. In (e) and (f), the bright white spots are voids in the film, some of which are pointed at by the red arrows. The voids in the Pd-capped 20 nm Mg appear to be spherical, while in the 50 nm version they are grain-shaped.

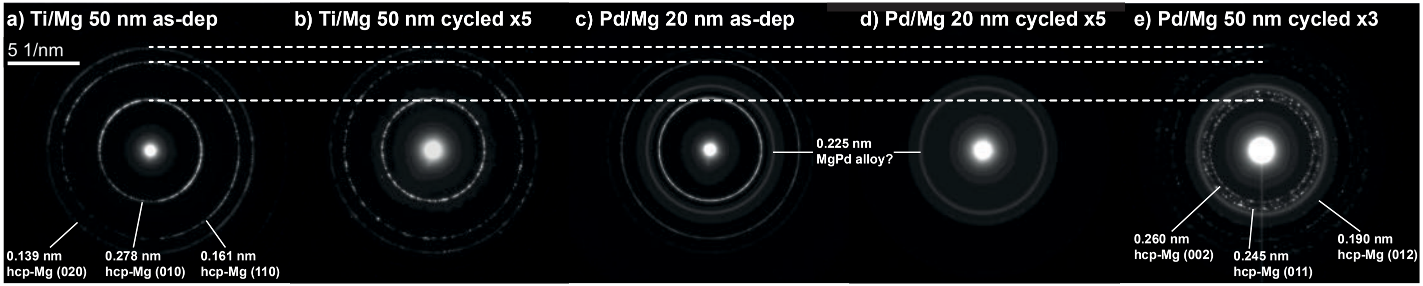

Figure 5.4 SAED patterns for (a) as-deposited Ti-sandwiched Mg (Si_3N_4 / Ti 2 nm / Mg 50 nm / Ti 2 nm / Pd 3 nm), (b) the same sample cycled five times with hydrogen, (c) Pd-capped Mg 20 nm (Si_3N_4 / Ti 2 nm / Mg 20 nm / Pd 5 nm), (d) same sample cycled with hydrogen five times and (e) Pd-capped Mg 50 nm cycled with hydrogen three times (Si_3N_4 / Ti 2 nm / Mg 50 nm / Pd 5 nm). The cycled Pd-capped Mg 20 nm sample becomes amorphous, while the Pd-capped 50 nm Mg shows much more reflections from Mg, indicating that the sample is losing the (002)-texture it had after deposition and yet remains crystalline.

sult in thickness dependent changes in the crystallinity, the preferential orientation and the density of the Mg films.

Hydrogenography

We measure the hydrogenation thermodynamics of multiple Mg thicknesses within a Mg-wedge sample under exactly the same conditions ('Hydrogengraphy'). The so-called pressure-transmission-isotherms of several Mg layer thicknesses recorded at 363 K are shown in Figure 5.5a. The optical transmission is normalized to T_0, the transmission at the start of the absorption experiment at low hydrogen pressure. Upon increasing the pressure, the Mg layer hydrogenates, resulting in a drastic increase in the transmission. These pressure plateaus are identical to the pressure-composition plateaus observed in *e.g.* a Sieverts measurement. The thickest part of the Mg-wedge ($d_{Mg} = 39$ nm) hydrogenates first at ~300 Pa, while the thinner the Mg layer the higher the plateau pressure. Below 20 nm, no plateau is observed because the maximum H_2 pressure in the hydrogenation cell is lower than the required value.

After the pressure plateau reaches its end—when MgH_2 has formed—the isotherm turns upwards. The optical transmission increases with several step-like features (or "wobbles"), as indicated in Figure 5.5a for $d_{Mg} = 39$ nm. This was never observed in Ti-sandwiched Mg, which shows a much more steep increase in the optical transmission (*i.e.* the isotherm turns vertical at the end of the plateau).[84] These wobbles are tentatively assigned to the hydrogenation of the (amorphous) interface alloy. It is well described that amorphous phases do not show pressure plateaus but sloped isotherms.[114]

The thickness dependence is not at all present in hydrogen desorption. The isotherms of the 2nd desorption cycle recorded at 363 K are shown in Figure 5.5b. The isotherms start at the top right of the figure, and all the data is normalized to the hydrogenated state. Hence, upon hydrogen desorption the values for $\ln {}^{T}\!/_{T_0}$ become negative. Now, instead of a variation in the plateau pressure with thickness as is the case in absorption, the plateau pressures are roughly equal for all thicknesses. Remarkably, the desorption pressure (3 Pa) is almost an order of magnitude lower than the ones found for Ti-sanwiched Mg layers (10 Pa at 363 K).[105]

Figure 5.6 shows an overview of the ab- (open symbols) and desorption (closed symbols) plateau pressures as a function of $1/d_{Mg}$. From both the elastic clamping model and the enthalpy model, the desorption plateau pressures are expected to have the same linear behavior as the one for the absorption data. The linear fit of the absorption pressures with $1/d_{Mg}$ is roughly equivalent to the previously reported values for 333 K.[58] Hence, we observe an asymmetric widening of the hysteresis in the Mg/Pd films. Clearly, this cannot be understood on the basis of thermodynamics alone. A component related to the plastic deformation must be active as well. We

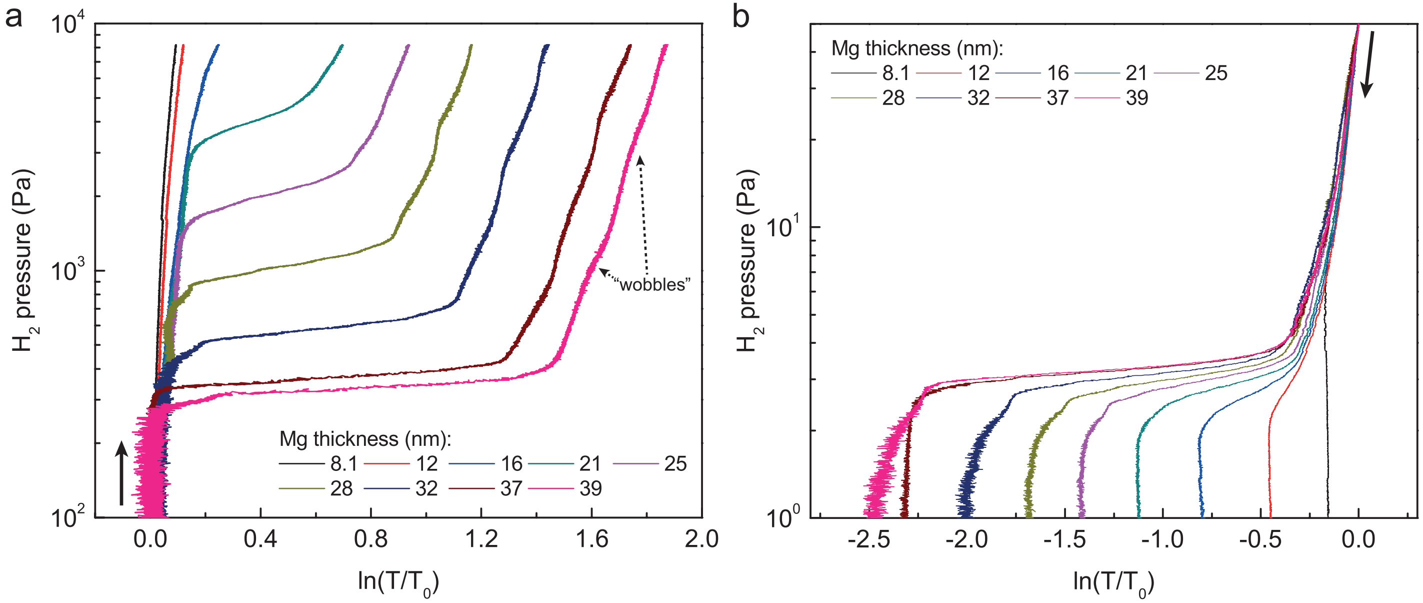

Figure 5.5 (a) Third absorption cycle of the Pd-capped Mg-wedge layer. (b)Second desorption cycle of Pd-capped Mg wedge at 363 K. For all thicknesses the sample unloads at the same hydrogen pressure of 3 Pa.

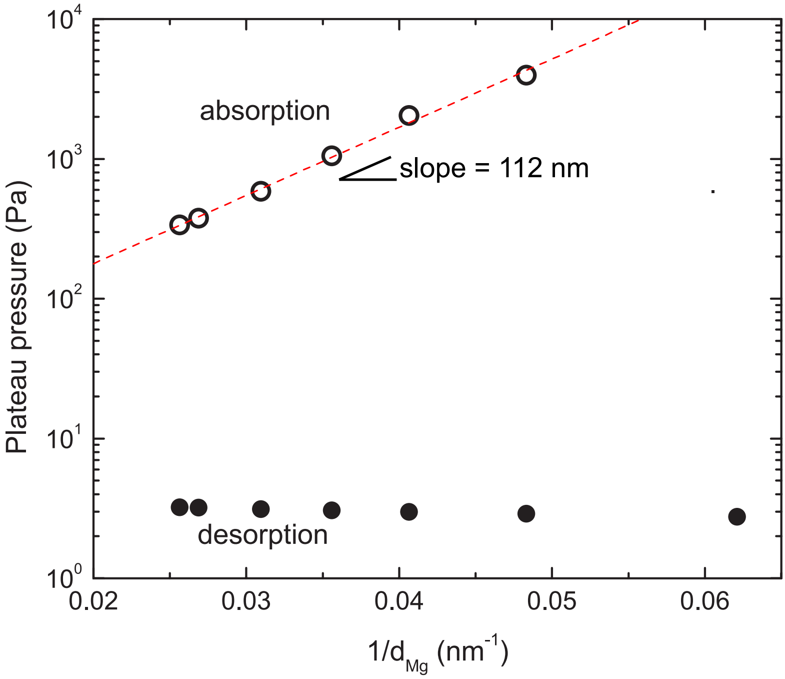

Figure 5.6 Plateau pressures versus $1/d_{Mg}$ of the 3rd absorption and the 2nd desorption. In absorption the data is comparable to the data of Baldi *et al.* and Chung *et al.* The desorption data shows no observable trend with $1/d_{Mg}$, while the same trend as in absorption is expected from both the earlier proposed models.

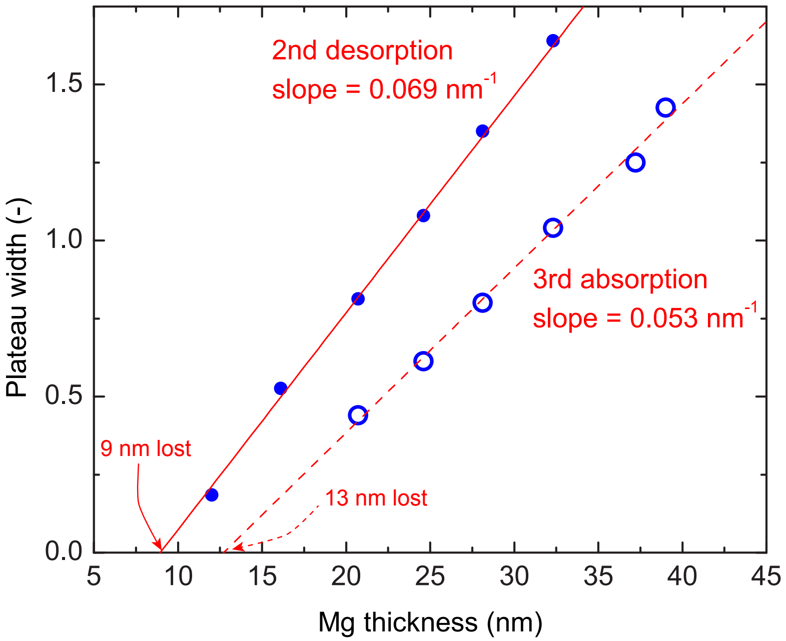

Figure 5.7 Plateau widths of 3rd absorption and the 2nd desorption. The intercepts with the x-axis (d_0) are respectively 13 nm and 9.0 nm.

will further discuss the origin of this asymmetry in ab- and desorption pressures in the Discussion section.

The plateau widths—*i.e.* the change in optical contrast $\ln T/T_0$ of the plateau—of both the ab- and desorption isotherms decrease with Mg thickness, which is expected because the optical contrast scales with the Mg thickness. As shown in Figure 5.7, both ab- and desorption datasets show a linear relation of the plateau width versus the Mg layer thickness. In both datasets, the intercept with the x-axis gives the equivalent thickness of 'lost' Mg for hydrogenation, *i.e.* the amount of Mg that does not hydrogenate. Earlier, for the 1st absorption cycle, this was shown to be equal to 6 nm.[63] In these wedge samples, from the intercept with the x-axis we find a loss of 9.0 nm in 2nd desorption cycle and a loss of 13 nm in the 3rd absorption cycle. This decrease in available Mg for hydrogenation can be due to increased alloying with Pd, the increased fraction of amorphous phase, or incomplete hydrogen desorption. From the desorption experiments we find no evidence for the latter possibility (not shown here).

Cycling behavior

We investigated the cycling behavior in hydrogen absorption of Pd-capped Mg wedges at T = 333 K. Figure 5.8 shows the first three cycles of several Mg thicknesses, ranging from 12 to 32 nm. With cycling, the plateau pressures change and also the plateau width decreases. The plateau pressures for samples with thicknesses from 17 to 32 nm all decrease upon cycling, while they increase for the Mg layers thinner than 16 nm. The 16 nm sample has roughly the same plateau pressure for all three cycles.

Hence, given these changes upon cycling, as a first guess one could say that this is the result of increased alloying with the Pd capping layer. This is, however, too simplistic considering the complex relation between the Mg layer thickness and change in microstructure and crystallinity as a function of cycling we found from the TEM results. These result showed that, after cycling, the final state of 20 nm Mg was amorphous, while for 50 nm Mg it was (at least for a large part) crystalline. It is plausible that with every hydrogenation cycle the fraction of amorphous phase varies depending on the Mg thickness, which in turn may affect the found pressure plateaus. How exactly the structure influences the pressure plateaus of the Mg layer is at this time unclear.

5.3.2 $Mg_{1-y}Pd_y$ alloys

Given the formation of Mg-Pd alloys in the multilayers, we decided to study the these alloys separately. Using thin film $Mg_{1-y}Pd_y$ gradient samples we investigated the crystal structure, microstructure and hydrogen sorption properties of $Mg_{1-y}Pd_y$ over a wide compositional range ($y = 1.7 - 30\%$).

XRD

The diffractograms belonging to several Pd concentrations y are shown as a waterfall plot in Figure 5.9. For all concentrations there are three prominent diffraction peaks, which change in 2θ position and peak area. The hcp-Mg (002) peak is indicated by "Main peak" in the figure. There is a large shoulder at $2\theta = 35^\circ$, which we refer to as "Side peak". Finally, there is a reflection of the Pd (111) peak at $2\theta = 40^\circ$. This peak is the combined signal from the pure Pd cap layer and any Pd phase that is formed within the $Mg_{1-y}Pd_y$ alloy layer. Several minor peaks can be seen at larger Pd concentrations (*i.e.* at $2\theta = 33.4^\circ$), however a meaningful discussion of their origin is difficult because they are not easily assigned to any phase.

We deconvolute the main and side peak positions as a function of y_{Pd} by a fit with a double Gaussian, which also gives the areas of both peaks. The resulting 2θ values for the main peak versus y_{Pd} are shown in Figure 5.10 as the open black circles, of

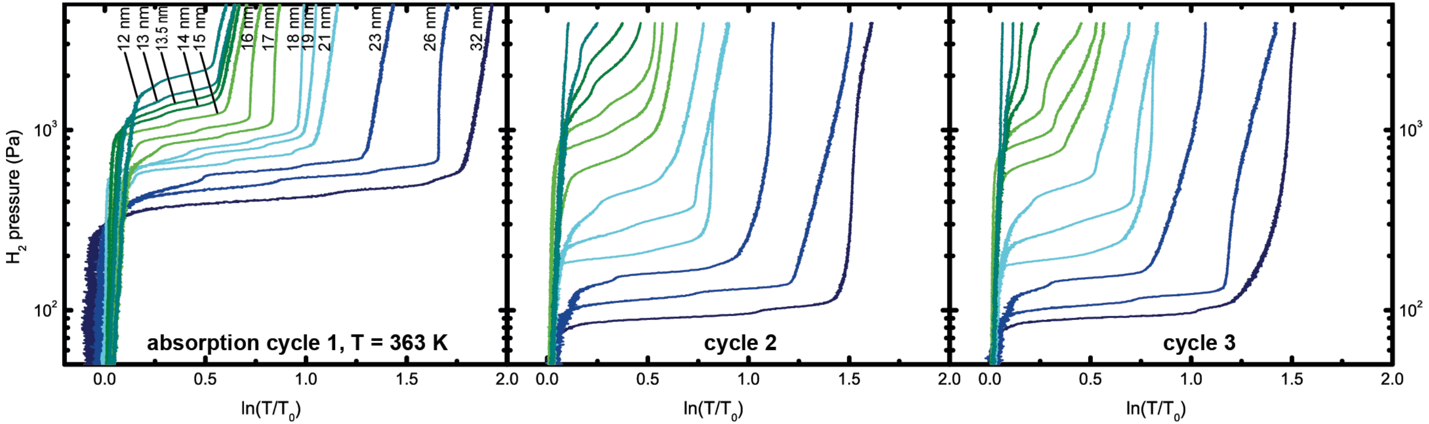

Figure 5.8 Cycling behavior of several Mg thicknesses (Pd-capped) at T = 333 K, with from left to right cycle 1, 2 and 3.

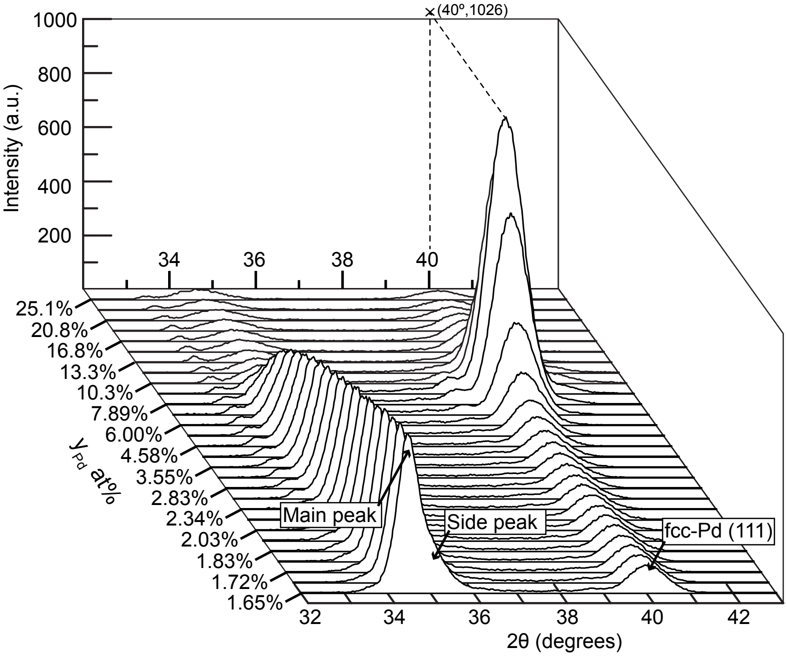

Figure 5.9 XRD patterns as a function of y_{Pd} of as-deposited $\mathrm{Mg}_{1-y}\mathrm{Pd}_y$ layers. The hcp Mg (002) peak is referred to by “Main peak”, while an extra peak at 35° is referred to as the “Side peak”. The peak at $2\theta = 40°$ is the fcc-Pd (111) peak, which varies in intensity.

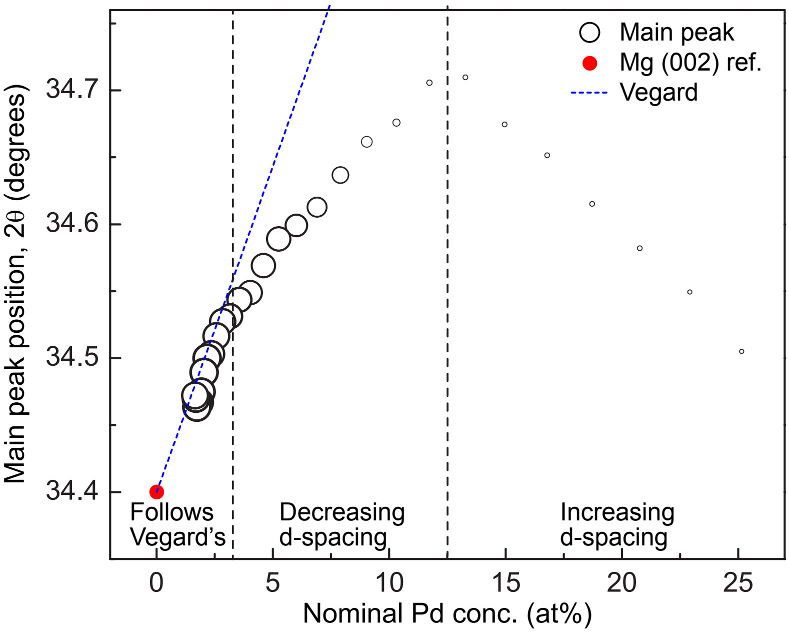

Figure 5.10 Peak position of the main peak—*i.e.* hcp-Mg (002)—versus the nominal Pd concentration. The main peak area is indicated by the size of the symbols. Below $y = 3\%$, the peak position follows Vegard's law (blue dashed line) for a mixture of Mg and Pd. Between $y = 3\%$ and 12.5%, the trend deviates from Vegard's law, with apparently less Pd entering the observed hcp-phase. The d-spacing, however, is still decreasing together with the main peak area. Above $y = 12.5\%$ the d-spacing again increases and the peak area decreases drastically.

which the size indicates the peak area. The peak position follows Vegard's law for a mixture of Mg and Pd (blue dashed line) when $y < 3\%$. Above this concentration, the amount of Pd in the hcp-Mg lattice is less than expected from Vegard's. However, up to the nominal concentration $y \approx 12.5\%$, the decrease in lattice spacing indicates that the Pd concentration still increases within the hcp-Mg phase. The observed lattice contraction is expected given the smaller molar volume of Pd as compared to Mg (respectively 8.85 cm^3/mol and 13.97 cm^3/mol). For y¿3%, the main peak area (symbol size in Figure 5.10 decreases significantly, which suggests a decrease in the Mg$_{1-y}$Pd$_y$ crystallinity. This may indicate that, with increasing y, an increasing fraction of the Mg$_{1-y}$Pd$_y$ layer is amorphous.

Above $y = 12.5\%$, the peak position returns to smaller 2θ angles, thus increasing the lattice spacing. In this region, however, the main peak area remains very small. Thus, in this region, either the crystalline hcp-MgPd phase is only a minor constituent of the sample, or the grains are highly refined. This could be caused by a grainrefinement effect during the deposition, when Mg and Pd are co-sputtered.

A peculiar feature of the diffractograms in Figure 5.9 is the huge increase in intensity of (presumably) the fcc-Pd (111) peak ($2\theta = 40^\circ$) around $y = 9\%$. Within the Mg-Pd phase diagram[ref], the first phase to form beyond the hcp-Mg phase is the Mg_6Pd phase, for which $y = 14.3\%$. At this concentration, however, the peak intensity has decreased again to values similar to lower y (*i.e.* $y < 6\%$). Furthermore, the reported crystal structure of Mg_6Pd has no diffraction peaks at $2\theta \approx 40^\circ$, while this phase furthermore has a very large unit cell ($V = 8.14$ nm^3).[115] The only Mg-Pd phase to which we can assign this peak is the bcc-MgPd phase ($y = 50\%$), which has a diffraction peak of the (110) plane at $2\theta = 40.4^\circ$. This angle is, however, too high to to allow us to assign the drastic increase in peak intensity to the formation of the MgPd phase. Hence, we propose that (for unknown reasons) the Pd-phase can grow or nucleate efficiently around $y = 9\%$.

The origin of the side peak at $2\theta \approx 35^\circ$—which we also find with lower intensity for Pd-capped Mg—is another open question. A Mg-Pd phase that possibly is the origin is the Mg_5Pd_2 phase, with the (013) plane having a diffraction peak at $2\theta = 34.95^\circ$.[115] It is possible that this phase is formed, as the crystal structure is hexagonal like pure Mg. To form this phase the Mg atoms only move a limited distance from their positions in the hcp-Mg (002) plane. In this case we would expect, however, to find a diffraction peak of the (002)-plane of this phase, as the growth of Mg is textured with the (002) plane parallel to the substrate.

In summary, it is likely that phases other than hcp-Mg are formed within the studied range of Pd concentration. Furthermore a fraction of the sample—which increases with y_{Pd}—may be amorphous.

TEM

The microstructure of the $Mg_{90}Pd_{10}$ layer is completely different from the Pd-capped Mg. The as-deposited state is shown in Figure 5.11a, where highly refined grains are visible. The SAED pattern for the same sample (Figure 5.12a) reveals reflections of an hcp-Mg phase. The resolution of the image is too small to to detect a shift in lattice reflections due to dissolved Pd as seen in XRD. Upon cycling with hydrogen ten times the microstructure changes drastically (Figure 5.11b). Grains have grown to 10-20 nm in size, while also a large number of voids (the bright white spots) have formed. . While the grain growth can be understood from an enhanced hydrogen induced mobility during cycling, the voids are rather surprising. It appears as if the expansion of the film on hydrogenation, is not fully relaxed on dehydrogenation. The formation of free surfaces (voids) is apparently more favorable than the plastic deformation needed to revert the film back to the initial (condensed) state.

The SAED pattern of the cycled film (Figure 5.12b) does not reveal large changes compared to the as-deposited state, although the increased crystallite size can be

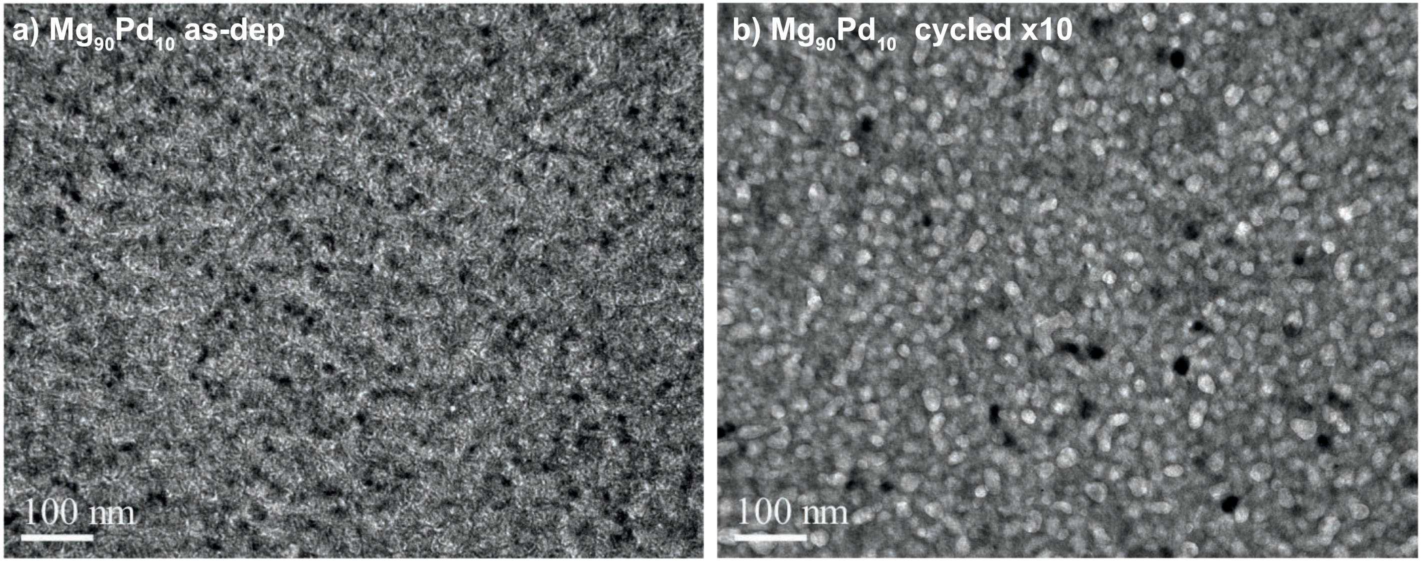
a) $Mg_{90}Pd_{10}$ as-dep
100 nm
b) $Mg_{90}Pd_{10}$ cycled x10
100 nm

Figure 5.11 (a) As deposited $Mg_{90}Pd_{10}$ (Si_3N_4 / Ti 2 nm / $Mg_{90}Pd_{10}$ 50 nm / Ti 2 nm / Pd 3 nm) and (b) the same alloy cycled with hydrogen ten times. The bright white spots in the cycled layer are voids.

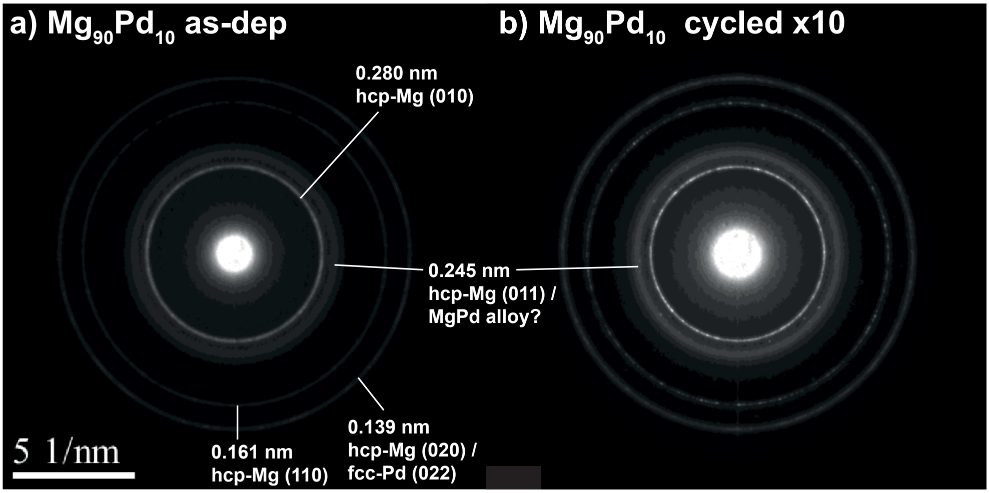

Figure 5.12 SAED patterns for (a) as-deposited $\mathrm{Mg_{90}Pd_{10}}$ ($\mathrm{Si_3N_4}$ / Ti 2 nm / $\mathrm{Mg_{90}Pd_{10}}$ 50 nm / Ti 2 nm / Pd 3 nm), (b) the same sample cycled ten times with hydrogen.

observed from the increased spot intensity within the diffraction circles. A vague amorphous diffraction ring with a d-spacing of 0.245 nm is present in both the as-deposited and cycled state. In the cycled state, this ring has an increased intensity compared to the as-deposited state. The origin is not a diffracting plane visible in the XRD data. A good match is the hcp-Mg (011) plane, but given the many crystalline reflections of the Mg phase also present in the SAED pattern we believe that this is an unlikely origin. Therefore, we ascribe the diffraction ring to a reflection of an (amorphous) Mg-Pd phase, similar to the Pd-capped Mg layers.

Hydrogenography

Hydrogenation isotherms of the MgPd alloy recorded at $T = 363$ K are shown in Figure 5.13. The range of compositions is limited to $y = 1.7 - 16\%$, because above 16% hydrogen absorption was either not observed or at a higher pressure than the experiment allowed for. Figure 5.13a shows the first hydrogen absorption cycle. The main features of the isotherms are again a change in plateau pressure and plateau width with Pd concentration y and with cycle number.

The plateau pressures increase with increasing y_{Pd}, which leads to an absorption plateau pressure at $y = 16\%$ two orders of magnitude higher than at $y = 1.7\%$. This ratio remains roughly the same in the 2nd absorption cycle (Figure 5.13b), where all the plateau pressures are lowered compared to the 1st cycle. Above $y = 12\%$, however, the slope of the pressure plateaus increases, resulting in a partial hydrogen

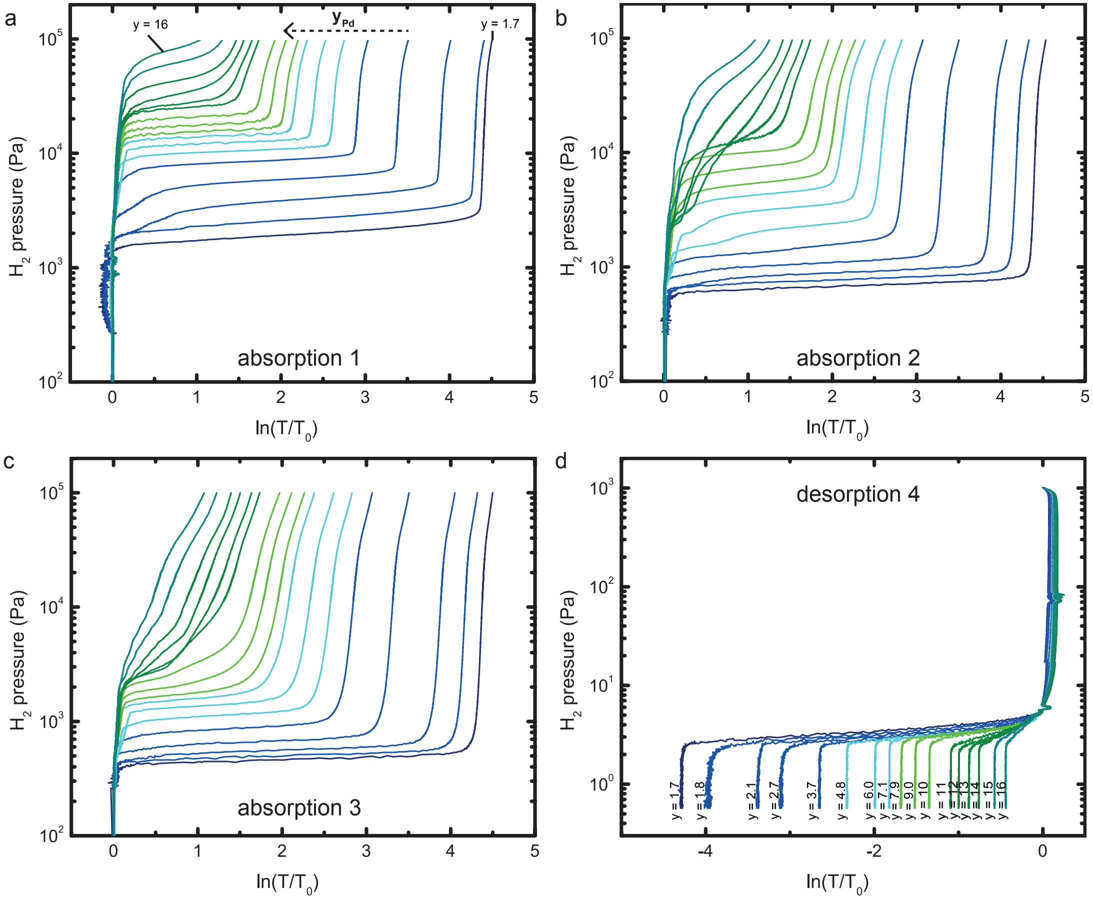

Figure 5.13 Hydrogenography PTI's ($T = 363$ K) of several $Mg_{1-y}Pd_y$ with (a) absorption cycle 1, (b) absorption cycle 2, (c) absorption cycle 3 and (d) desorption cycle 4. The Pd concentration y (in percent) of the isotherms is given in the desorption isotherms (d).

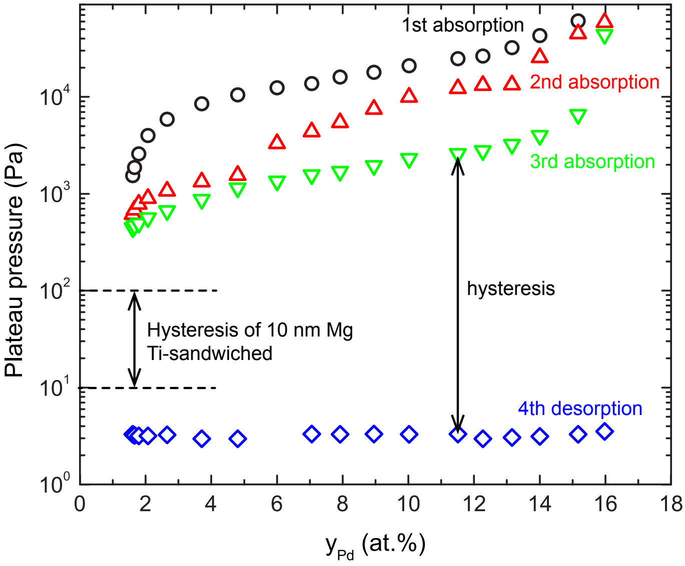

Figure 5.14 Plateau pressures as a function of y_{Pd} for the isotherms shown in Figure 5.13. At larger y-values the point with the lowest slope is taken as the "plateau" pressure. The ab- and desorption pressure and resulting hysteresis of Ti-sandwiched, 10 nm Mg layers are added as a reference.

absorption at low pressure ($\sim 3 \times 10^3$ Pa), while the rest is absorbed between 10^4 and 10^5 Pa. In the third cycle (Figure 5.13c), the plateau pressures are again lower for all isotherms. Now, the slope of the pressure plateaus for Pd concentrations below $y = 9\%$ have all increased. Similar to the Pd-capped Mg layers, we again ascribe this behavior to the hydrogenation of an amorphous Mg-Pd alloy.

Similar to the Pd-capped Mg, the desorption isotherms are not affected by the Pd concentration (Figure 5.13d). All the isotherms show that hydrogen desorbs at the same pressure, here equal to about 3 Pa.

An overview of the pressure plateaus as a function of cycling is shown in Figure 5.14. After the first absorption cycle, the plateau pressures for the isotherms with $y < 12\%$ are all lowered. The same process occurs when comparing absorption cycle 2 to cycle 3, although at low Pd concentrations the plateau pressure reaches a minimum. The hysteresis of all isotherms is very large, ranging from two orders of magnitude in pressure ($y = 1.7\%$) to over three orders of magnitude ($y = 16\%$). Compared to Ti-sandwiched Mg, which has a hysteresis of about one order of magnitude in pressure, the hysteresis has increased drastically.[84]

The widths of the plateaus for all cycles are given as a function of y in Figure 5.15. The total alloy layer thickness varies (it becomes thinner the more Pd is added),

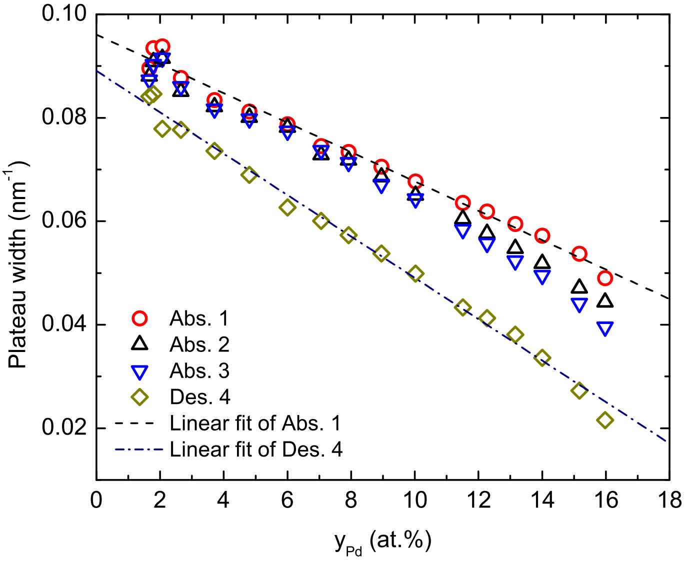

Figure 5.15 Plateau widths for the three absorption cycles (cycles 1-3) and the 4th desorption cycle. Linear fits of both the first absorption and desorption cycles are furthermore shown.

therefore the plateau widths are now normalized to the layer thickness so only the effect of the addition of Pd follows from the plot. Upon cycling, the absorption plateau widths decrease slightly with cycling. The desorption plateau width of the 4th cycle is much lower than the width of the 3rd absorption plateau. In desorption we presumably only measure the dehydrogenation of MgH_2. This indicates that in the absorption cycles the optical change includes the hydrogenation of any other (Mg)PdH_x phase.

From the linear fits of the plateau widths with Pd concentration y, we find how Pd changes the hydrogenation reaction. From the 1st absorption cycle, the intercept with the y-axis ($y_{Pd} = 0\%$) gives 0.096 nm^{-1}, which agrees very well with the value found for pure Ti-sandwiched Mg of 0.1 nm^{-1}.[63] The intercept of the desorption fit is at 0.089 nm^{-1}, which means that some of the Mg is lost for hydrogenation upon cycling.

The slope of the desorption fit gives the lost width per at.% Pd added to the layer. We assume that the desorption width only contains the desorption of MgH_2. If one Pd atom substitutes one Mg atom and does not change the hydrogenation in any other way, the expected slope would be -1%. This is equivalent to one Mg atom lost for hydrogenation per Pd atom added. We find, however, that the slope is -4.2%. This is equivalent to 4.2 Mg atoms lost per Pd atom added. Hence, per Pd atom substituted for Mg, an extra 3.2 Mg atoms do not hydrogenate to MgH_2. These lost Mg atoms may be stuck within a MgPd alloy phase, which possibly does not hydrogenate (or only partially).

Assuming that only MgH_2 is formed and not a sub-stoichiometric phase, the found 4.2 Mg atoms lost per Pd atom would give the following first generalized reaction step for the hydrogenation of the alloy:

$$\mathrm{Mg}_{100-y}\mathrm{Pd}_y + (100 - 4.2y)\mathrm{H}_2 \rightarrow (100 - 4.2y)\mathrm{MgH}_2 + \mathrm{Mg}_{3.2y}\mathrm{Pd}_y$$

Direct evidence for a further hydrogenation step of the remaining $Mg_{3.2y}Pd_y$ is lacking, although the plateau widths in absorption seem to indicate that this indeed happens.

5.4 Discussion

The main question to answer for both the Pd-capped Mg and $Mg_{1-y}Pd_y$ is why in these alloyed and multilayered films the hydrogen absorption pressure increases by up to three orders of magnitude compared to bulk Mg, while the desorption pressures show no dependence on either the Mg thickness or the Pd concentration y. We propose a qualitative model which takes the combined effects of the Mg-Pd alloy, nucleation, mechanical deformation and diffusion (*e.g.* Pd diffusion upon alloy dissociation) into account. Without combining these effects we are unable to explain the observations made in the previous sections.

The hydrogenography data for the wedge and alloy samples are very similar, especially when comparing at Figures 5.6 and 5.14. In these figures, the absorption pressures of thin Pd-capped Mg and the alloy at low Pd concentrations are roughly the same. For both these samples, the absorption pressure is about 10^3 Pa for the 3rd absorption cycle. Furthermore, in the XRD data of both samples we find a peak at $2\theta = 35°$, indicating that a similar phase is present in both sample types. We assign this diffraction peak to a so far unknown Mg-Pd alloy. The peak intensity is much lower in the Pd-capped Mg sample than in the alloy sample, which is the result of the interface alloy being much thinner (6 nm) than the typical thickness of the alloy layer (about 40 nm).

As described in the introduction, such an interfacial alloy of 2-3 nm in thickness will not change the ΔH for hydrogen absorption of the 40 or so nanometers of pure Mg that lies below. Alternatively, Ryden *et al.*[85] find that hydride nucleation occurs preferentially at Mg-Pd interfaces. They show that this is a thermodynamic, and not a kinetic, effect. However, if we apply this nucleation effect to the Pd-capped Mg layers, we see no reason why the absorption plateau pressure would increase with decreasing Mg thickness.

Hence, another ingredient is needed to explain our results. Plastic deformation has been shown to increase the hysteresis of thin films compared to bulk equivalents.[60] Due to the clamping of the thin films to the substrate, plastic deformation is needed to accommodate the volume expansion on hydrogenation, which occurs in the out-of-plane direction. From the model of Pivak *et al.*[60], it follows that the hysteresis should broaden around the same average pressure, *i.e.* the desorption pressures should decrease as much as the absorption pressures increase. In contrast, we recently found evidence for a large asymmetry in ab- and desorption of Ti-sandwiched Mg thin films.[105] In hydrogen absorption, the volume expansion due to hydrogenation can only occur by plastic deformation, there is no other mechanism capable of accommodating a 30% volume expansion. In desorption, however, we found evidence that the desorption is decoupled from the plastic contraction. Instead, we suggested the formation of voids. For Ti/Mg multilayers, we concluded that the creation of inner surfaces is energetically much more favorable than plastic deformation and does not depend on the thickness of the multilayer.[116] This explains that the desorption pressure is similar to bulk and Ti-sandwiched Mg.

The formation of new surfaces agrees very well with the voids observed in both the wedge and alloy Mg/Pd layers. Considering that the Mg/Pd interface alloy is not easily deformed because the Mg and Pd layers are welded together by the formation of an alloy, the energy needed to nucleate MgH_2 (which contains a plastic deformation energy term for the deformation of the top layers) will be higher than for Ti-sandwiched Mg with a flat Ti/Mg interface. This furthermore explains why we find that the absorption plateau pressure increases with decreasing magnesium thickness: Assuming that the interface alloy has a constant thickness for all Mg thicknesses, the relative thickness of the interface alloy increases compared to the unalloyed Mg thickness.

We propose that the absorption plateau pressures of the alloy are increased by a similar effect, but in this case the interface layer is exchanged for an alloy with changed mechanical properties in the whole layer. For sake of simplicity, we assume that the enthalpy of MgH_2 formation is not changed due to the mixing with Pd. The alloy layers have highly refined grains, which means that to nucleate MgH_2 the dissociation of Mg and Pd is required. This dissociation process requires atomic diffusion, which will certainly be slow at for instance 393 K. With increasing hydrogen pressure, however, the driving force for nucleation of MgH_2 increases. From classical nucleation theory, if the driving force for nucleation increases the critical nucleus size decreases. Therefore, the need for long range diffusion of Mg and Pd decreases as well. Hence, in our hydrogenation experiments, the found plateau pressure indicates the pressure where the MgH_2 nucleus radius is small enough to enable large-scale transformation to the hydride phase.

In desorption, we found no difference between the wedge and alloy samples.

This implies that the size of the MgH_2 domains is irrelevant for the energetics of the desorption mechanism. Furthermore, in both cases we find the formation of voids after cycling with hydrogen. Hence, we may say that in both cases the desorption pressure is related to the formation of free surface. In fact, the desorption pressures of Mg sandwiched by Ti, Fe and Pd vary, at 363 K they are respectively 10, 7 and 3 Pa. It is, however, difficult to directly relate these pressures to the interface energies of Mg/MgH_2 with Ti, Fe and Pd because the microstructure and morphology of these systems vary.

We realize that the above reasoning is still highly tentative and would require a more detailed investigation. However, the complexity of these two Mg-Pd systems does not readily allow for a straightforward characterization of the essential physical properties.

In summary, a lowered enthalpy of MgH_2 formation due to an interface Mg-Pd alloy can not explain the observed ab- and desorption pressures by itself. We propose that a combination of plastic deformation and nucleation effects govern the hydrogen sorption thermodynamics and microstructure evolution in both Pd-capped Mg and $Mg_{1-y}Pd_y$ alloys.

5.5 Conclusion

From an analysis of both ab- and desorption isotherms, we conclude that the elastic clamping model proposed by Baldi *et al.*[58] and the interface alloy model proposed by Chung *et al.*[64] do not grasp the underlying nature of the changes in hydrogenation thermodynamics of Pd-capped magnesium layers.

There are indeed many similarities between Pd-capped Mg layers and deliberately made $Mg_{1-y}Pd_y$ alloys, most notably the formation of voids within these thin films upon cycling with hydrogen. The complex relation between the microstructure development and hydrogen sorption characteristics hampers the formulation of a quantitate model. This leads us to propose a qualitative model which emphasizes the effects of mechanical deformation and hydride nucleation. In hydrogen absorption, the volume expansion is only possible via plastic deformation of the multilayer, while in desorption the creation of free surface is the energetically more favorable pathway. The required plastic deformation energy results in a large increase in the absorption plateau pressure, while the formation of voids is independent of the local environment of MgH_2 thereby hardly influencing the desorption plateau pressure.

Thus, we can not stress enough the importance of obtaining a full overview of the hydrogenation thermodynamics by measuring both hydrogen *ab*- and *de*sorption. This is especially important when searching for nano metal hydrides that are destabilized compared to their bulk equivalents.

Chapter 6

Mg/Fe multilayers: The role of microstructure on the hydrogenation of Mg

6.1 Introduction

Many applications of hydrogen storage materials require hydrogen to be released around atmospheric pressure at moderate temperature. This is especially true for mobile applications, where high temperature waste heat is typically unavailable. Although there are materials that match these requirements, such as $LaNi_5H_6$,[11] these are often too heavy and can not compete with conventional high pressure gas storage.

Magnesium hydride is a light-weight metal hydride that can store up to 7.6 wt% of hydrogen.[14, 97] In the bulk form, however, it is very stable and requires temperatures of about 300 °C to release hydrogen at a pressure of 1 bar. Furthermore, it suffers from poor transport of hydrogen through the hydride phase, thereby hampering the hydrogen release rate.[23] The latter problem can be solved by nanostructuring the magnesium hydride,[117] which furthermore has the potential to thermodynamically destabilize magnesium hydride.

In this chapter, we investigate whether the interface energy affects the hydrogenation thermodynamics in a multilayer model system. We place thin Mg layers between two Fe layers, and modify the interface-to-volume ratio by changing the Mg layer thickness.

Destabilization through nanoconfinement requires that the surface-to-volume ratio is large. Only then the surface (or interface) energy starts to play a large role in the phase transformation thermodynamics.[73, 74] Through calculations of the surface energy, Kim *et al.*[41] have shown that nanosized MgH_2 is destabilized compared to bulk. The hydride phase is destabilized because the surface energy of MgH_2 is larger than the surface energy of Mg. Based on the results of Kim *et al.*, a MgH_2 nanoparticle of 1 nm in size will be destabilized by 5 kJ/mol H_2 compared to the bulk enthalpy of formation. Assuming ΔS is unchanged, at 100 °C this destabilization is equivalent to an appreciable fivefold increase in the equilibrium hydrogen pressure. Experimental evidence of this surface energy effect is, however, difficult to obtain. The main reason for this difficulty in (Mg) nanoparticle systems is the loss of surface area due to agglomeration.[33]

Another way to destabilize MgH_2 is by alloying Mg with other elements. It has recently been shown that mixing Fe into Mg thin films during deposition results in a phase separated nanostructure with greatly enhanced kinetics for hydrogen ab- and desorption from magnesium hydride.[118] The authors claim that the enhancement is caused by the phase separation of bcc-Fe. The Fe percolates the Mg layer and envelops the Mg grains, which allows for fast hydrogen diffusion. It is not clear, however, whether the thermodynamics of hydrogen sorption change due to the presence of Fe.[119] In the phase separated structure the Mg-Fe interface-to-volume ratio is very large. In analogy to the surface energy effect, when the MgH_2/Fe *interface* energy is larger than the Mg/Fe interface energy, the MgH_2 phase will be destabilized compared to bulk.

In chapter 2, we have shown that the change in interface energy may indeed play a role in the hydrogenation of thin Mg/TiH_2 multilayers (d_{Mg}¡ 10 nm).[84] With decreasing Mg layer thickness, the interface-to-volume ratio increases and we find that both the ab- and desorption pressures are larger than the bulk MgH_2 pressures. The plateau pressures followed the relation $\ln p \propto {}^1/_{d_{Mg}}$, while we know that for a thin film ${}^1/_d \propto {}^A/_V$. We confirmed this interpretation by calculations of the Mg/TiH_2 and MgH_2/TiH_2 interface energies based on first principles. To confuse matters, however, the destabilization effect is larger on hydrogen absorption than on desorption. This is unexpected because the interface energy effect should act equally during ab- and desorption. Furthermore, the anisotropy is unwanted because the destabilization is smaller for hydrogen desorption—exactly the process in need of destabilizing.

In search for an explanation for this asymmetric behavior, in chapters 3 and 4 we discovered that the nucleation and growth mechanisms during hydrogen ab- and desorption may not be always the same, *i.e.* not each other's reverse.[105, 116] During absorption, the barrier for nucleation is appreciable: the apparent absorption plateau pressure is increased by half an order of magnitude for a 10 nm Mg layer. During desorption, however, the nucleation barrier appears to be negligible. We explain this behavior by the large asymmetry in the (plastic) deformation processes (expansion versus contraction). In absorption, MgH_2 domains were observed to nucleate and then grow 2-dimensionally, *i.e.* in plane. Such a mechanism could not be observed for Mg nucleation and growth (H-desorption).

Here we investigate whether Mg/Fe multilayers show enhanced destabilization of magnesium hydride compared to Mg/Ti(H_2) multilayers, through the interface energy effect. As in Mg/Ti multilayers, the Fe layers have a double function: They

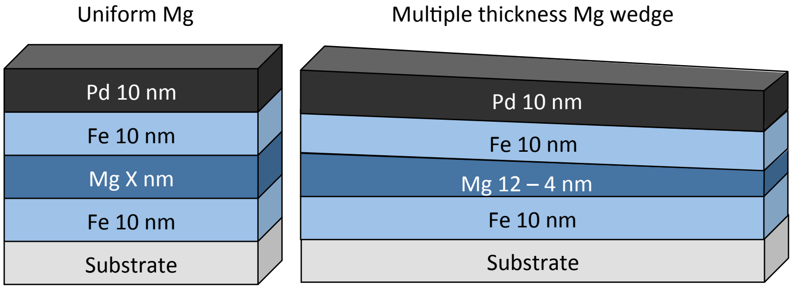

Figure 6.1 As deposited sample geometries with (left) uniform Mg and (right) Mg wedge samples. The varying parameter is the Mg layer thickness X.

should destabilize MgH_2 through the interface energy effect and the top layer should furthermore protect the Mg from oxidation and chemical interactions with the Pd capping layer. It has been shown that Mg and Pd intermix at the interface and greatly increase the absorption plateau pressure of MgH_2 formation.[63, 64] We expect the interface energy effect of Mg/Fe to be different from the previously investigated Mg/Ti system. Unlike Ti, Fe does not readily form a hydride, which may indicate a potential increase in the destabilization of MgH_2 due to the interface.

We measure the hydrogenation isotherms of the thin Mg layers with Hydrogenography, [48] an optical technique that records the change in optical transmission as a function of the hydrogen pressure. This allows us to measure the so called pressure-transmission-isotherms (PTI's) for Mg layers with thicknesses down to 1 nm. Furthermore, with Mg-wedge layers surrounded by Fe (Figure 6.1), we measure many Mg thicknesses under exactly the same conditions. In absorption, we find that the hydrogenation occurs in two, well-defined steps, while in desorption we do not find such a behavior. From a structural analysis with X-ray reflectometry and TEM, we relate the hydrogenation behavior of this multilayer system to the microstructure of the Mg layer.

6.2 Experimental

Layer growth Thin layers of Fe, Mg and Pd were deposited on 10x10x0.4 mm Si (100) substrate wafers (XRR, CS-TEM), and 70x5x0.5 mm fused quartz (Hydrogenography) using sputter deposition in a UHV system (AJA Int.), equipped with an automatic shutter system. The base pressure is of the system is 10^{-9} mbar. Because the sputter gun is at an angle with the 70 mm long quartz wafer substrate, without rotation the sputter rate of Mg will be large on one side and small on the other. This results in Mg wedge-samples with Mg thicknesses ranging from 4 to 12 nm. The layer geometries are shown in Figure 6.1, with X the Mg layer thickness.

X-Ray Reflectometry (XRR) measurements were performed on multilayer samples deposited on approximately 10x10 mm Si (100) using a Bruker D8 Discover x-ray diffractometer equipped with a parallel x-ray beam (Cu $K\alpha_1$ $\lambda = 1.5406$ Å). The data was collected and reduced following the guidelines of Salah *et al.*[120] and with instrumental broadening, over illumination and background corrections built into GENX, the fitting software.

CS-TEM Cross section Transmission Electron Microscopy (CS-TEM) images were recorded on the same multilayers deposited on Si (100) with X = 3.1 and 38 nm. The TEM, STEM and EDX results were all acquired using a FEI Tecnai G2 electron microscope, operating at 200 kV. Preparation of the TEM cross-section samples consists of multiple steps. First the bulk material is sawn into 2 mm by 500 μm blocks using a diamond wire saw (first into 2 mm thick strips, which are then sawn into 500 μm wide blocks in the perpendicular direction). The blocks are then glued together face to face, with the multilayer sides facing each other. Mechanical polishing is used to thin the glued sample in several steps (thinned to subsequently: 6 μm, 3 μm, 1 μm and eventually 0.5 μm). The thinned sample is then glued upon an annular TEM grid. The final thinning is done by ion milling using a Leica RES 101 operating first at 5 kV using and subsequently 1.5 kV with the gun placed at an angle of 8°.

Hydrogenography measurements were performed on the Mg-wedge samples placed in a stainless steel hydrogenation cell. This cell is placed in a furnace and we recorded pressure-transmission-isotherms at several temperatures: 333, 363, 393, 423 and 453 K. The data were recorded using a 3-CCD camera (Sony). The hydrogen gas pressure can be controlled between 0.1 and 10^6 Pa by using diluted H_2 in Ar and pure H_2. Depending on the temperature, 4% H_2 in Ar or 100% H_2were used for measuring absorption isotherms, and 0.1% H_2 or 4% H_2 in Ar for desorption isotherms.

6.3 Hydrogen ab- and desorption

We investigated the hydrogenation behavior of Mg-wedge layers surrounded by two 10 nm Fe layers (Figure 6.1) with Hydrogenography. This optical technique enables us to record about 620 separate hydrogenation isotherms along the 7 cm long wedge sample. Every isotherm thus corresponds to a specific Mg thickness, which ranges from 4 to 14 nm.

Figure 6.2 shows hydrogen absorption isotherms recorded at $T = 333$, 363, 393 and 423 K for several Mg thicknesses. The transition from Mg to MgH_2 is visible at all temperatures through the large change in optical transmission, visible as pressure plateaus. Over a small pressure range (the plateau has a small slope), there is a large change in optical contrast ($\ln {}^{T}/_{T_0}$). The plateau pressure—approximated by the middle of the pressure band—varies with the Mg thickness: The absorption plateau pressure increases with decreasing Mg thickness. Furthermore, the width of the plateau, *i.e.* the total change in $\ln {}^{T}\!/_{T_0}$, decreases with decreasing Mg thickness, because the formed amount of MgH_2 decreases. We found both these trends in the Mg/TiH_2 multilayers as well.[84]

In contrast to the Mg/TiH_2 multilayers, we now find a double plateau below a certain onset Mg thickness. For example, at $T = 333$ K the isotherm for 13 nm Mg shows a single plateau, while for 5 nm Mg the plateau splits into two (one lower and one upper plateau, Figure 6.2a). The thickness where the first hump of the double plateau can be seen is 6 nm. Below that thickness, the plateau is split up into one plateau at low pressure (the lower plateau) and one plateau at high pressure (the upper plateau). The upper plateau always has a larger slope than the lower plateau. At $T = 363$ K, the double plateau presents itself when the Mg thickness is lower than 8.1 nm, while at $T = 393$ K the thickness is 9.0 nm. At 423 K, the onset thickness is 9.8 nm. Hence, the onset thickness is increasing with temperature.

We now investigate the plateaus in more detail—both as a function of the Mg layer thickness and the temperature—through an analysis of the plateau width and plateau pressure.

6.3.1 Plateau width analysis

The plateau width, *i.e.* the optical contrast change, upon hydrogenation of Mg is proportional to the amount of MgH_2 formed.[84] Hence, we expect that with decreasing Mg layer thickness, the plateau width decreases proportionally. In Figure 6.3 this proportionality is confirmed by the linear relation between the full plateau data (black circles) and the Mg layer thickness, based on the absorption isotherms recorded at 333 K. A least squares linear fit (red dashed line) fits the data well. We would, however, expect that the x-axis is intercepted at $d_{Mg} = 0$ nm. The linear fit instead intercepts the x-axis at $d_{Mg} = 1$ nm. This means that, for all Mg thicknesses, 1 nm of Mg does not contribute the MgH_2 formation. A similar effect was observed earlier in the work of Baldi *et al.* for Mg/Ti multilayers,[63] where a loss of 3.2 nm of Mg was observed. Hence, in case Mg is surrounded by Fe, the loss of Mg capable of hydrogenating is significantly reduced.

Figure 6.3 furthermore shows the relative widths of the lower and upper plateaus at 333 K. The upper plateau first appears at $d_{Mg} = 6$ nm and its width increases with decreasing Mg layer thickness. The growth in width of the upper plateau occurs at the expense of the width of the lower plateau. The sum of the two widths follows the same linear relation as does the single plateau in the region $d_{Mg} > 6$ nm. Therefore, we attribute both the plateaus to the hydrogenation of Mg to MgH_2.

The stability of the Mg layer is tested by following the plateau widths as a function

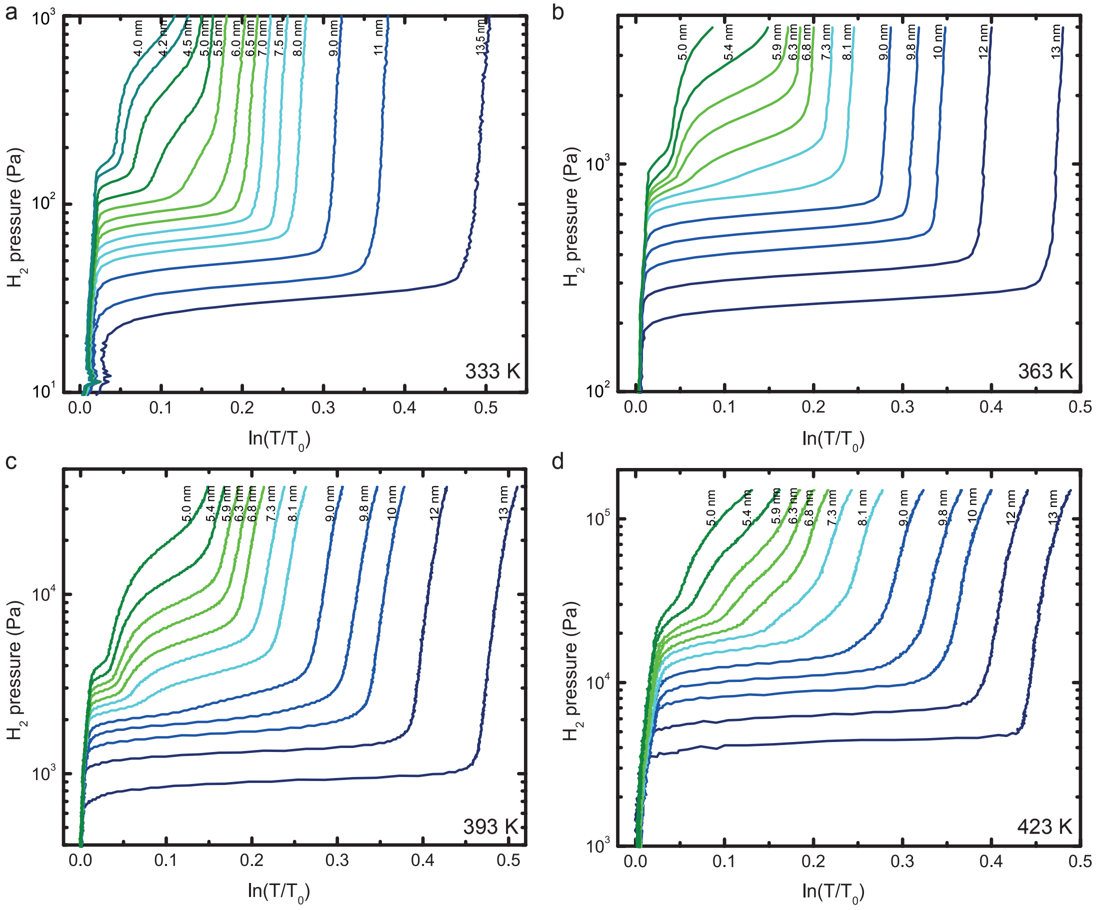

Figure 6.2 Absorption isotherms of Mg-wedge multilayers with (a) absorption isotherms of several Mg thicknesses recorded at $T = 333$ K, (b) ab- and desorption isotherms recorded at 363 K, (c) ab- and desorption isotherms recorded at 393 K and (d) ab- and desorption isotherms recorded at 423 K.

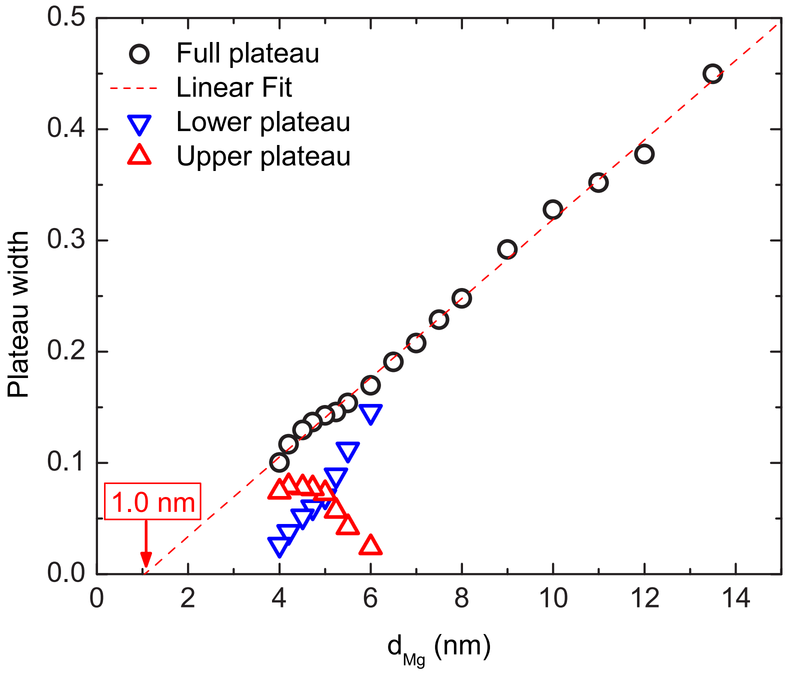

Figure 6.3 Total plateau width and the widths of the lower and upper plateaus

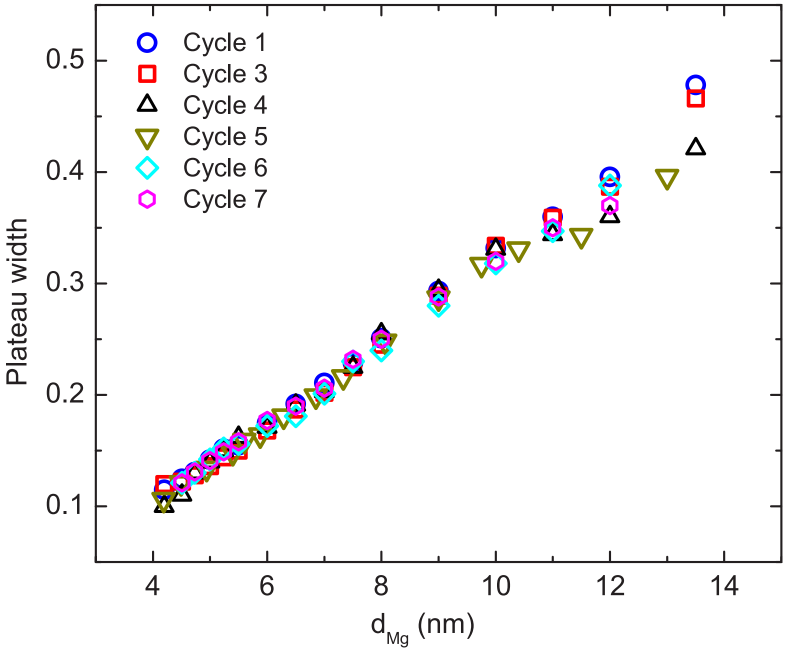

Figure 6.4 Plateau widths of absorption isotherms recorded at 60 °C as a function of cycle number. The width remains constant with cycling indicating the Mg layer is remains stable.

of repeated hydrogenation at $T = 333$ K. The resulting plateau width versus thickness is plotted in Figure 6.4. Up to a Mg thickness of 11 nm, there is no detectable change in the plateau width with cycling. Larger thicknesses show more spread in the plateau width, but there is no clear trend with cycle number (*e.g.* the plateau width at $d_{Mg} = 12$ nm is lower in cycle 4 than in cycle 7). Although no similar cycling data is available for higher temperatures, in Figure 6.2b, c and d, we observe that the plateau width of 13 nm Mg remains roughly constant with $\ln {}^{T}/_{T_0} \approx 0.47$ (Figure 6.2b, c and d are respectively the 2nd absorption at 363 K, 3rd absorption at 393 K and the 4th absorption at 423 K).

At a temperature of 453 K, however, the hydrogenation of the Mg layer is not at all stable. From a cycling experiment (Figure 6.5), repeated hydrogenation shows a large change in the plateau width as well as a large change in the shape of the isotherm. Figure 6.5 shows isotherms for three Mg layer thicknesses (11, 8 and 6 nm) recorded at $T = 453$ K. The open symbols represent the first absorption, while the closed symbols represent the second absorption. After cycling, the plateau widths are greatly reduced, which indicates that less MgH_2 is formed.

Hence, given the non-linear temperature dependence of the hydriding stability

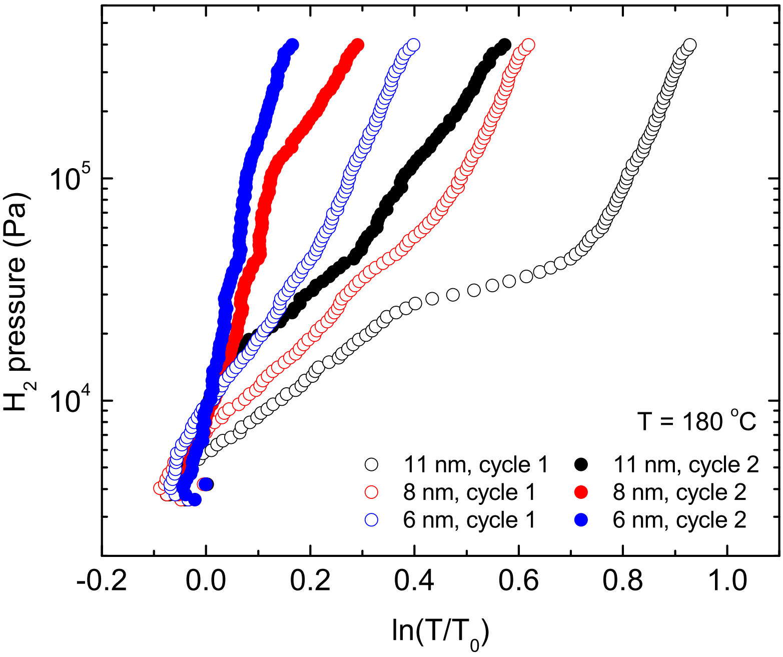

Figure 6.5 Cycling is detrimental for the Mg layers at high temperature: Isotherms recorded at 180 °C of three thicknesses in a Mg-wedge multilayer, with data of X = 11 nm (black), X = 8 nm (red) and X = 6 nm (blue) and 11 (black) nm. Open and closed symbols represent cycle 1 and 2 respectively.

of the Mg layers, we expect that the Mg is somehow contaminated through, for instance, a diffusion or phase transformation process. We imagine that a $MgFe_x H_y$ phase forms, or that Pd diffuses through the Fe layer to alloy with Mg at the Mg-Fe interface—an effect shown to occur at room temperature for Pd-capped Mg (in the absence of a protecting layer between Mg and Pd).[64] A further discussion should include the origin of the double plateau. Here we first investigate the plateau pressures and the structure and morphology of the Mg/Fe multilayers.

6.3.2 Plateau pressure analysis

In our previous experiments on Mg/TiH_2 multilayers, we found that the plateau pressure increases with, and is proportional to, $1/d_{Mg}$.[84] This relation is expected when the interface energy difference between MgH_2/M and Mg/M is positive and non-zero, with M the interfacing material. For a thin film, $1/d_{Mg}$ is equivalent to the surface-to-volume ratio A/V. From theory, we found that for a thin film the interface energy difference $\Delta\gamma$ can be obtained from:[84]

$$\ln p_{nano} = \ln p_{\infty} + \frac{2V_{Mg}\Delta\gamma}{RT} \times \frac{1}{d_{Mg}} \tag{6.1}$$

where p_{nano} is the plateau pressure at Mg layer thickness d_{Mg}, and p_{∞} the pressure at infinite thickness (*i.e.* bulk Mg). V_{Mg} is the molar volume of Mg and R the gas constant. The factor 2 is there to account for the two interfaces of Mg with the surrounding material. For M = TiH_2 we found that $\Delta\gamma$ is 0.35 J/m^2 for hydrogen absorption at 333 K.

The presence of the double plateau complicates a similar analysis on the Mg/Fe data. We extracted the plateau pressures of the single, lower and upper plateaus for all the isotherms from Figure 6.2, and we plot the plateau pressures versus $1/d_{Mg}$ in Figure 6.6. For all four temperatures, we performed two least squares fits: One on a combination of the single plateau data and the upper plateau data (dashed lines), and the other on the lower plateau data (dotted lines). The single and upper plateau pressures seem to follow the same trend with $1/d_{Mg}$, although at $T = 333$ K and $T = 423$ K one may argue whether that is correct. The lower plateau pressures, on the other hand, are all fitted perfectly by the dotted lines.

Here we compare the found values internally (*i.e.* with temperature) and with Mg/TiH_2 data. Using Equation 6.1, we calculate $\Delta\gamma$ from the slopes of the eight linear fits. The values are shown in Figure 6.6.

The slopes of the upper and single plateau data give varying values for $\Delta\gamma$, which ranges from 1.9 J/m^2 at $T = 333$ K to 2.8 J/m^2 at $T = 423$ K. In absolute terms, interface energy differences of up to 1 J/m^2 are expected,[41] but here we find values in excess of 2 J/m^2. Hence, we must conclude that there is an effect on the plateau

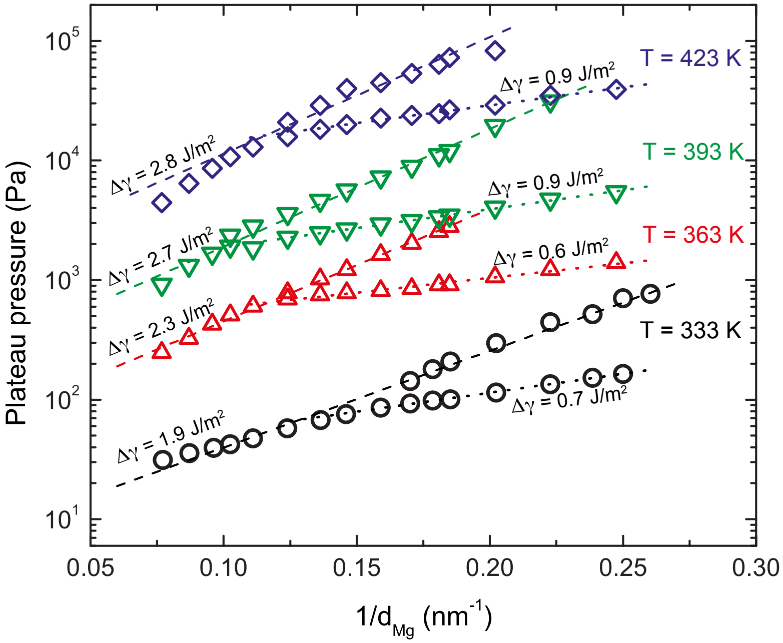

Figure 6.6 Total plateau width and the widths of the lower and upper plateaus

pressures other than the interface energy effect. This additional effect is still a function of the Mg layer thickness, with $\ln p \propto {}^{1}/_{d_{Mg}}$.

The separate linear fits of the lower plateau pressures (dotted lines in Figure 6.6) agree well with the data. In this case, the values for $\Delta\gamma$ are roughly constant with temperature, with an average value of 0.78 J/m^2. This value qualitatively agrees more with what we would expect—*i.e.* the value is larger than that for Mg/TiH$_2$ multilayers and not too large. The value is, however, difficult to interpret in terms of an interface energy effect because the lower plateau only presents itself at low Mg thicknesses.

From both sets of linear fits (single plus upper plateau fits and lower plateau fits), the intercept with the y-axis at $1/d_{Mg} = 0$ nm^{-1} gives p_∞ (Equation 6.1). This is the hydrogenation pressure extrapolated to infinite Mg thickness, *i.e.* bulk-like magnesium. For each of the two sets of linear fits, we obtain four pressures for four temperatures. Hence, we can construct a Van't Hoff plot from p_∞ versus $1/T$ and obtain ΔH and ΔS. From the single and upper plateau fits we find $\Delta H = -66.9$ kJ/mol H$_2$ and $\Delta S = -118$ J/Kmol H$_2$. For the lower plateaus we find $\Delta H = -69.6$ kJ/mol H$_2$ and $\Delta S = -141$ J/Kmol H$_2$. Hence, the enthalpy changes are not too different for both datasets. Furthermore, both values for ΔH are somewhat lower than those found in the literature, *i.e.* $\Delta H = -74.4$ kJ/mol H$_2$.[14] It is not uncommon, however, that the enthalpy values for hydrogen absorption are somewhat higher than the desorption values, due to hysteresis.

As mentioned in the introduction, a change in ΔH of 5 kJ/mol H$_2$ already gives significant changes in the plateau pressure. Practically, however, what matters is pressure at which hydrogen desorbs, and not the ΔH values. Hence, we also investigated the desorption of hydrogen from the Mg/Fe multilayers.

6.3.3 Desorption

The desorption isotherms of the Mg multilayer samples are shown in Figure 6.7. Hydrogen desorption from the Mg/Fe wedges is different from absorption in two ways: There is no double plateau and the desorption pressure is roughly the same for all Mg thicknesses.

At 333 K (Figure 6.7a) the thinnest Mg layer desorbs hydrogen at a higher pressure than the thickest Mg layer, but the pressures are much closer together than in absorption. The plateau pressure ranges from 0.7 Pa (13 nm) to 1.3 Pa (4 nm), with an average of 0.91 Pa.

At 363 K (Figure 6.7b), we find the same plateau pressure of 7.1 Pa for all thicknesses. At 393 K (Figure 6.7c), however, the order is (partially) reversed: The thickest, 13 nm Mg desorbs hydrogen at the highest pressure of 43 Pa. Around 9 nm a minimum in the plateau pressure of 34 Pa is reached, after which the plateau pres-

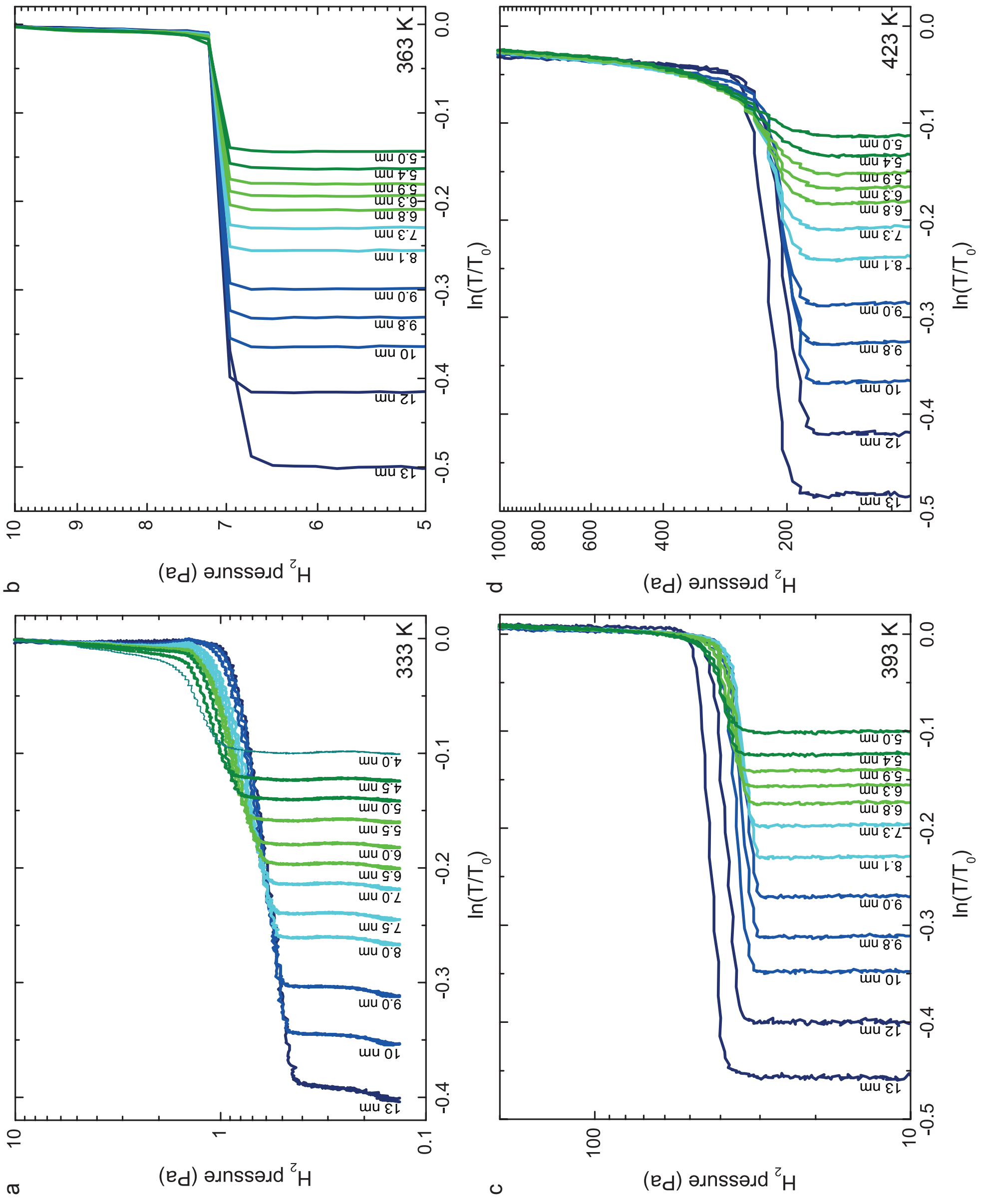

Figure 6.7 Desorption isotherms of several thicknesses in Mg-wedge multilayers recorded at (a) $T = 333$ K, (b) 363 K, (c) 393 K and (d) 423 K.

sure again increases to ~ 40 Pa when going down to 4 nm. At 423 K (Figure 6.7d), the plateau pressures are all roughly equal to 218 Pa. Hence, on the whole there indeed is some variation of the plateau pressures with the Mg thickness, but the spread is very small.

In contrast, in our previous experiments on Mg/TiH_2 multilayers, we found that the desorption pressures followed the same trend as the absorption pressures. The spread in the plateau pressures versus d_{Mg} was, however, less profound in desorption than it was in absorption. Given the poor H-diffusion in MgH_2, at 333 K the desorption plateau pressure may be influenced by diffusion limitations. This explains why the thinnest Mg desorbs first—*i.e.* at higher pressure—than the thickest Mg. At 393 K, however, the order of desorption is partially reversed, suggesting an additional effect other than diffusion. Note that in absolute terms the differences between the plateau pressures are very small.

As the desorption pressures are roughly equal for all Mg thicknesses, we take the average value in pressure at all four temperatures and again construct the Van 't Hoff plot, which is shown in Figure 6.8. We now obtain $\Delta H = -71.4$ kJ/mol H_2 and $\Delta S = -118$ J/Kmol H_2. Hence, in spite of the discrepancies between the hydrogen ab- and desorption process, we find that the change in entropy of the desorption process is the same as that of the absorption process. The enthalpy of MgH_2 formation, however, is 4.5 kJ/mol H_2 lower in desorption than in absorption (*i.e.* closer to the bulk-MgH_2 value, $\Delta H = -74.4$ kJ/mol H_2).

We added literature data to Figure 6.8. For comparison, Tan *et al.*[119] report the desorption pressures at $T = 403$, 413 and 423 K of thick Mg films (600 nm) doped with 4% Fe. At these temperatures, they report respectively 44, 75 and 113 Pa for the desorption plateau pressures (solid triangles). At 423 K we find a slightly higher value of 218 Pa for the average desorption plateau pressure. Krozer and Kasemo[121] reported desorption pressures for 1000 nm thin films at (among others) 334 K and 363 K of respectively 2.4 Pa and 16 Pa (solid diamonds), which are higher than our 0.9 Pa (333 K) and 7.1 Pa (363 K). Thus, from the desorption pressures alone, we conclude that the MgH_2 in the Mg/Fe multilayers is not destabilized compared to thick (bulk) MgH_2. The desorption pressures are, however, slightly higher than for the 600 nm Mg-4 at% Fe films of Tan *et al.*[119]

The absorption plateau pressures have furthermore been added (open symbols and arrows). The blue arrows indicate the plateau pressures as a function of the Mg layer thickness, while the blue circles are the plateau pressures extrapolated to $d_{Mg} = \infty$. Both in our Fe-sandwiched Mg layers and the Mg-4% Fe films the hysteresis is one to two orders of magnitude larger than for the thick films of Krozer and Kasemo. The increase in hysteresis is mostly due to a large increase in the absorption plateau pressures.

In order to investigate the reason for the hydrogenation behavior, we now study

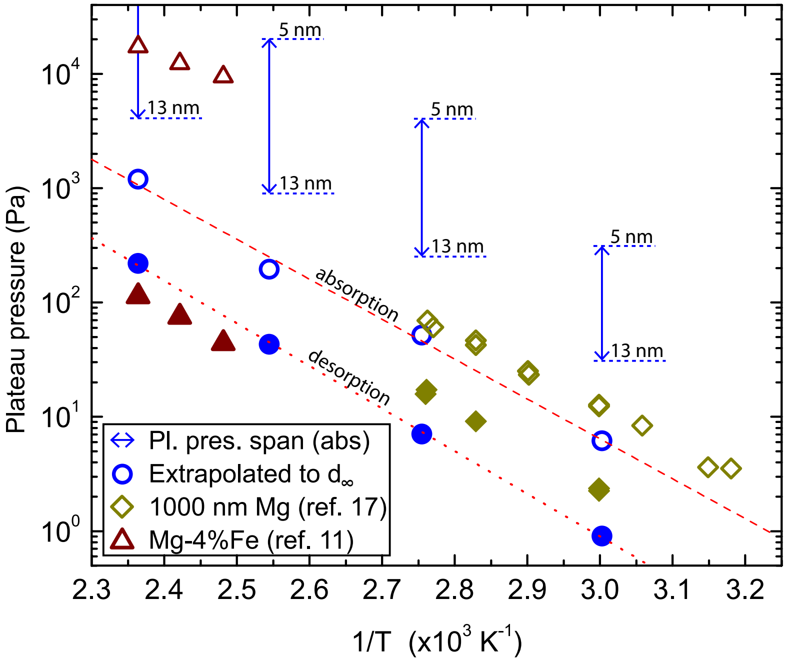

Figure 6.8 Van 't Hoff plot of the extrapolated bulk plateau pressures (from an extrapolation of the plateau pressures to $1/d_{\mathrm{Mg}}$ = 0) for absorption (open circles) and desorption (filled circles). The slopes of the respective least squares fits (red dashed lines) give ΔH, while the intercept with 1/T = 0 gives ΔS. For absorption, we find $\Delta H = -66.9$ kJ/mol H_2 and $\Delta S = -120$ J/Kmol H_2, while for desorption $\Delta H = -71.4$ kJ/mol H_2 and $\Delta S = -118$ J/Kmol H_2. Data from the literature are furthermore indicated, where the dark-yellow diamonds are data of ¿1000 nm Mg films from Krozer and Kasemo[121], and the dark-red triangles are data of 600 nm Mg-4 at% Fe from Tan *et al.*[119]

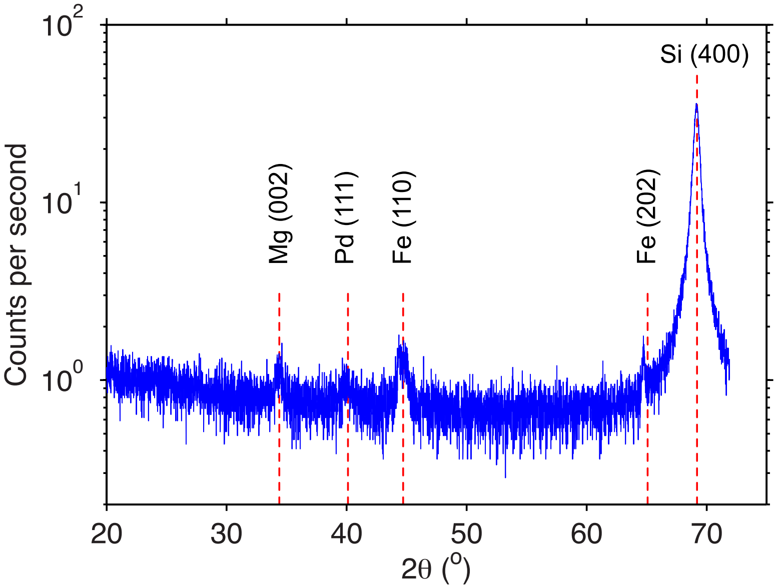

Figure 6.9 XRD spectrum of the 10 nm Fe, X =20 nm Mg, 10 nm Fe and 10 nm Pd multilayer. The peaks are assigned as indicated in the graph at the dashed red lines. The Si (100) substrate serves as an internal reference.

the structure and morphology of the Mg/Fe multilayers.

6.4 Structure and morphology

The crystal structure of the as-deposited multilayers is studied with X-ray diffraction (XRD) and shown in Figure 6.9. All the layers appear to be textured, with (110)-Fe (bcc) // (002)-Mg (hcp) // (111)-Pd (fcc) (the texture is further investigated in the TEM analysis). We ascribe the small peak at high angle ($\theta \approx 65^\circ$) to Fe-(002). The presence of this diffraction peak suggests that the texturing of the Fe layers varies to some degree.

To confirm whether the intended layer thicknesses of Fe, Mg, Fe and Pd agree with the actually deposited thicknesses, we performed X-ray reflectometry (XRR) measurements. With this technique we also obtain an indication of the roughness at the interface between the various layers. The interpretation is, however, somewhat ambiguous because it is difficult to distinguish true roughness from (atomic) intermixing at the interface.

We analyzed three Mg/Fe multilayers (deposited on (100)-Si) with varying Mg thicknesses ($X = 20$, 7.2 and 2.4 nm) with XRR. In all samples the intended thick-

Table 6.1 Nominal and fitted structural parameters of the Fe 10 nm / Mg X nm / Fe 10 nm / Pd 10 nm samples, with X the intended as grown thickness of Mg. Thickness d and roughness σ for the deposited layers (Fe, Mg, Fe, Pd) are all given in nanometer.

X (nm)	20	7.2	2.4
$d_{Fe,1}$	10.5	10.5	10.7
d_{Mg}	20.1	7.1	2.5
$d_{Fe,2}$	10.3	9.9	10.1
d_{Pd}	9.5	10.6	9.7
$\sigma_{Fe,1}$	0.5	0.6	0.5
σ_{Mg}	2.2	1.5	2.6
$\sigma_{Fe,2}$	2.4	2.6	1.2
σ_{Pd}	2.4	1.8	1.2

ness of the two Fe and top Pd layers is 10 nm. The data are fitted using GENX,[122] which uses a genetic algorithm to fit the parameters in a model of the sample to the XRR data. The data and best fit of a sample with $X = 20$ nm are shown in Figure 6.10a.

A plot of the scattering length density (SLD) as a function of position along the multilayer (Figure 6.9b) gives an overview of the sample. Because there is a large contrast between the (real part of the) SLD's of Mg (SLD$_{\mathrm{Mg}} = 1.48 \times 10^{-5}$ Å^{-2}) and Fe (SLD$_{Fe} = 5.94 \times 10^{-5}$ Å^{-2}), both the Fe and the Mg layer can be clearly distinguished. The roughness σ of a certain layer indicates its roughness at the interface with the next layer. For example, the roughness of the first Fe layer, $\sigma_{Fe,1}$, indicates the roughness at the Fe/Mg interface. Thus, σ_{Mg} indicates the roughness at the Mg/Fe (2nd Fe layer) interface. From the SLD plot, we can already qualitatively observe that the roughness of the first Fe layer is much smaller than the roughness of the Mg layer. Furthermore, although the contrast in SLD between the Fe and Pd layers is small, the roughness at the Fe/Pd interface appears to be high as well. Finally, the roughness of the Pd/air interface remains large.

The best fit results of all three samples are given in Table 6.1. All fitted layer thicknesses are in good agreement with the intended thicknesses. For all samples, the first Fe layer has a roughness of about 0.5 nm, while the found Mg roughnesses are 2.2, 1.5 and 2.6 nm for the 20, 7.2 and 2.4 nm Mg samples. The following Fe and Pd layers then follow a similar roughness as the Mg layer. If we assume that Mg and Fe intermixing does not happen, already from these results we may say that the Mg layer growth on Fe is probably non-uniform.

Since it is difficult to distinguish the true roughness from intermixing, we performed cross-section TEM. Figure 6.11 shows High-Angle Annular Dark Field - Scanning Transmission Electron Microscopy (HAADF-STEM) images of cross sections of

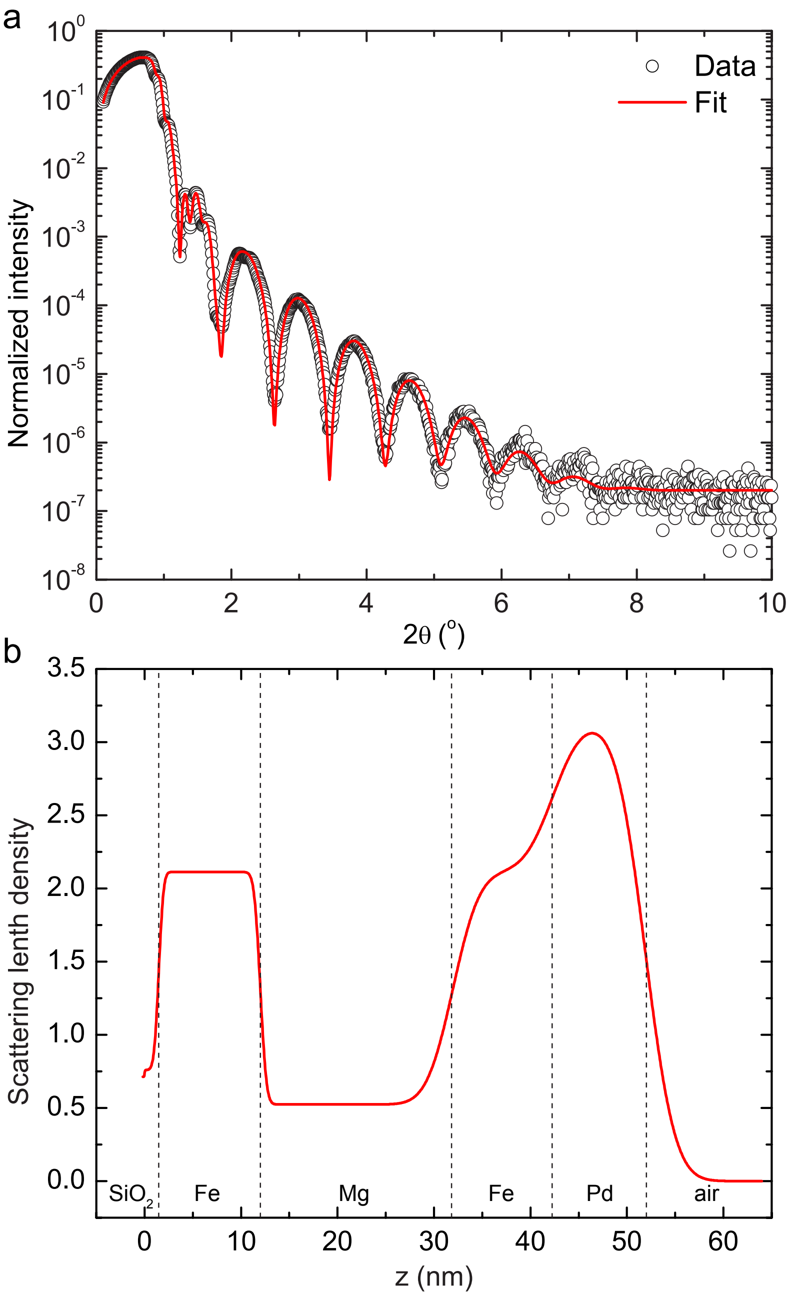

Figure 6.10 (a) XRR data and best fit of a 10 nm Fe, X =20 nm Mg, 10 nm Fe and 10 nm Pd multilayer. (b) The real part of the scattering length density of the best fit as a function of z, the height perpendicular to the Si substrate.

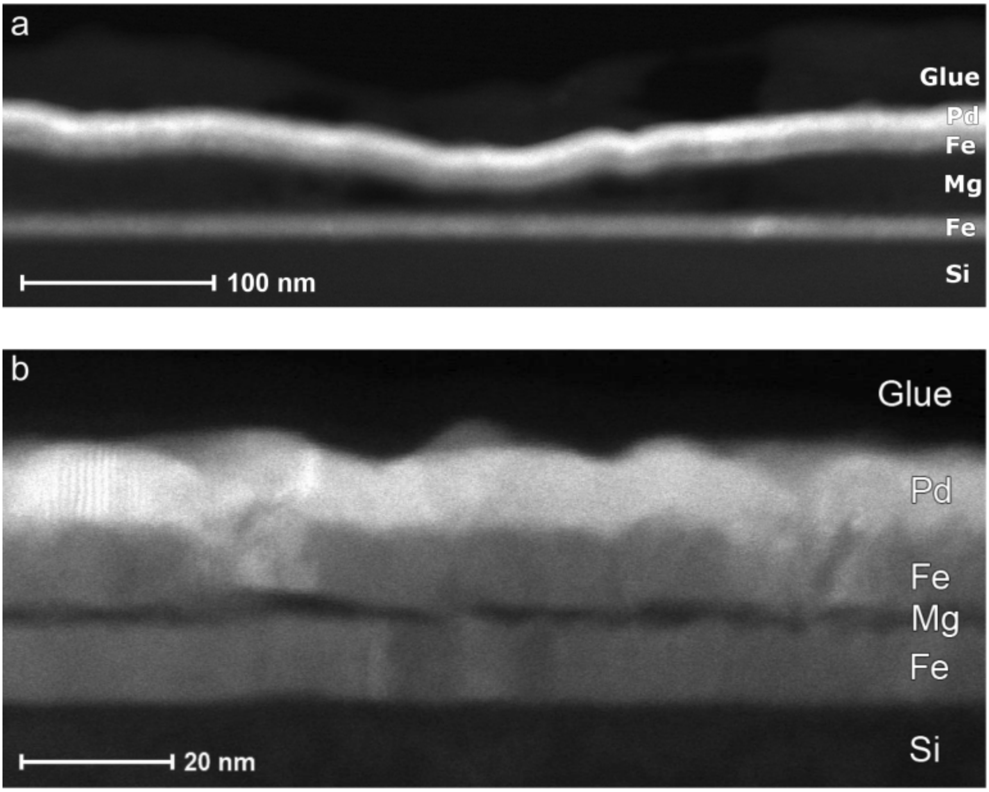

Figure 6.11 HAADF-STEM images of as-deposited multilayers with (a) X = 38 nm and (b) X = 3.2 nm.

two Mg/Fe multilayers, one with $X = 38$ nm and one with $X = 3.2$ nm. In the HAADF-STEM mode, the intensity of the image scales with the atomic number of the atomic species. Therefore, heavier elements will appear brighter than lighter elements. Thus, the Fe, Mg and Pd can be clearly distinguished. In both samples, the first Fe layer grows conformally on the Si substrate. The Mg layer, however, grows non-uniformly on the first Fe layer. In the image of the 38 nm sample, the Mg thickness varies from 20 to 50 nm.

In the $X = 3.2$ nm Mg sample, the Mg thickness again varies. Now, however, there are regions without any Mg at all, such as the region in the middle of the image in Figure 6.11b. Thus, the Mg appears to grow via an island growth mechanism.

For both samples, the second Fe and Pd cap layers grow more or less conformally on top of the rough Mg. Combining these results with the XRR results, we can say that the average Mg thickness is indeed as intended, but that the Mg layer shows large variations in the layer thickness. The top Fe and Pd layers then grow (more or less) conformally on Mg and therefore the roughnesses of the respective interfaces are similar to the Mg layer roughness.

The observed morphology is surprising when considering thin film growth from a surface and interface energy perspective. These parameters often govern the growth mode of thin films on substrates (in this case the substrate is Fe for the Mg layer, and Mg for the second Fe layer). Literature values for γ_{Mg}^{002} are significantly smaller than the ones for γ_{Fe}^{110} (resp. $0.523\ ^{\mathrm{J}}/_{\mathrm{m}^2}$ and $2.36\ ^{\mathrm{J}}/_{\mathrm{m}^2}$)[123, 41], which means that one would expect Mg to grow flatter than Fe.

We believe that instead the growth of Mg is governed by the presence of high-angle grain boundaries (GB's). When comparing a Mg layer grown on Ti with one grown on Fe, we find little evidence for high-angle (out-of-plane) GB's in the former sample, while many of such GB's are present in the latter type of sample. An example of what the Mg microstructure looks like in cross-section is shown in Figure 6.12. In Figure 6.12a, a cross section image of a 38 nm Mg layer grown on (and covered with) Ti is shown. The image has been enhanced to show the microstructure of the Mg layer. Although the Mg layer appears polycrystalline both in-plane and out-of-plane, the texturing remains (002) in nature, similar to the Ti layers. In contrast, a Mg layer grown on Fe shows an off-axis texturing, with a large fraction of the Mg having its (002) planes at an angle with the Fe layers (Figure 6.12b). We postulate that this is due to an epitaxial relation between the Mg and Fe layer. This relationship results in the formation of more high-angle GB's in the Mg layer. The presence of high angle GB's during growth can cause mound formation because the GB's act as ad-atom diffusion barriers, thereby causing the observed roughness.[124]

The GB in the Mg layer furthermore influences the growth of the top Fe layer. In Figure 6.12b the GB continues to be present in the top Fe layer grown, which is a second indication for an epitaxial relationship between Mg and Fe. This GB in Fe may furthermore act as a diffusion pathway for impurities, affecting the hydrogenation as we will discuss below.

6.5 Discussion

Now that we know that the Mg layer grows non-uniformly on the first Fe layer, we will try to relate this to: The double plateau in absorption, the single plateau in desorption, the thickness dependence of the plateau pressures and the instability of the layers at high temperature.

We first of all discard the possible (partial) formation of Mg_2FeH_6 as an explanation for any of our observations. It has been reported that Mg_2FeH_6 cannot be dehydrogenated at temperatures below 620 K.[125, 126] Therefore, any Mg that is converted to Mg_2FeH_6 will be unavailable for further hydrogenation cycles. The formation of Mg_2FeH_6 has been reported for the hydrogenation of Mg alloyed with ¿15

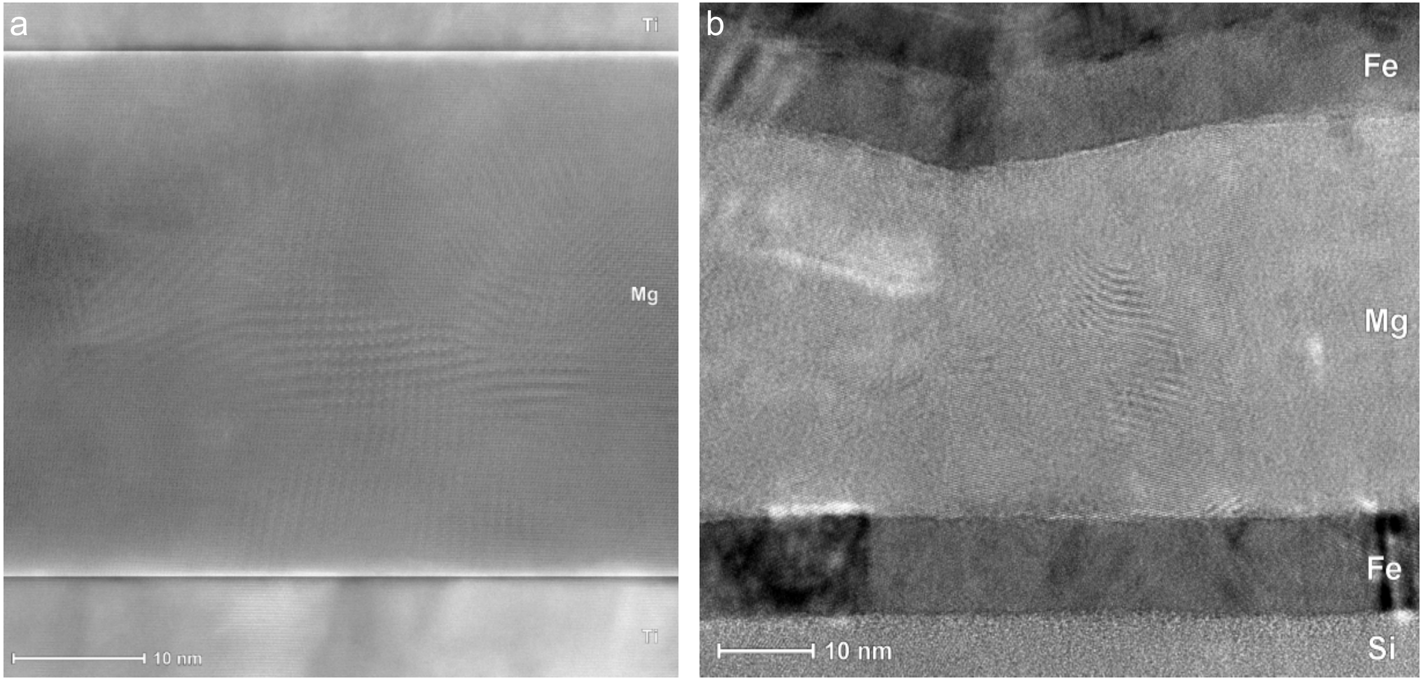

Figure 6.12 (a) HAADF-STEM image of an as-deposited Ti/Mg/Ti multilayer with X = 38 nm and (b) a HR-TEM image of an as-deposited Fe/Mg/Fe multilayer. In the Ti/Mg/Ti layer, few (high-angle) grain boundaries can be detected that are accompanied by a change in the Mg texture, In (b) an example of a high-angle grain boundary in the Mg layer, which is furthermore present in the top Fe layer. The Mg layer in (a) is optically enhanced to show the grain structure with low angle grain boundaries becoming visible, as well as clear (002)-texturing in all grains and the Ti layers.

at% Fe thin films at 413 K of Zheng *et al.*[118] We have, however, found no evidence of the presence of this phase with X-ray diffraction. Below 453 K, the cycling of the multilayer with hydrogen appears to proceed without losing Mg. At 453 K, we do observe loss of available Mg. However, the presence of irreversible Mg_2FeH_6 would not easily explain, for instance, the double plateau and the relation of the plateau widths and plateau pressures with the Mg thickness. Hence, we conclude that Mg_2FeH_6 formation is not the underlying mechanism for the bulk of our observations.

Instead we believe that there is a direct relation between the microstructure of the Mg layer and the hydrogenation behavior. We validate this assertion by preliminary hydrogenation experiments of Ti/Mg/Fe/Pd multilayers. In these samples, the Mg layer is as flat as in the Ti/Mg/Ti/Pd multilayer samples (see Figure 6.12). The ab- and desorption isotherms of the 4th hydrogenation cycle, recorded at 453 K, are shown in Figure 6.13. We find that even in this 4th cycle there are well defined plateaus, both in ab- and desorption. Furthermore, the upper plateau presents itself only when the Mg layer thickness is below 5 nm. At the same temperature, the Fe/Mg/Fe samples showed degradation already in the first cycle. At 423 K, the onset thickness for the double plateau was 9.8 nm, thus in the Ti/Mg/Fe sample it is significantly reduced. Thus, this shows that the Mg layer microstructure must be directly related to the observed instability with temperature and the formation of the double plateau.

In desorption, the thinnest Mg layers have the highest plateau pressures, pointing at a destabilization of the MgH_2 phase for thinner Mg thicknesses. At 453 K we do not expect a kinetic effect to be dominant. In fact, both the ab- and desorption pressures are higher than those of Ti/Mg/Ti samples.[84] In our previous experiments on Ti/Mg/Ti at 453 K, we found an absorption pressure of 1.4×10^4 Pa for a 3.2 nm Mg layer. The desorption pressure for this layer was 1.2×10^3 Pa. In the Ti/Mg/Fe case, for the same thickness we find an ab- and desorption pressure of 5×10^4 Pa and 2.7×10^3 Pa respectively. With equation 6.1 we find $\Delta\gamma = 0.4$ J/m^2 for hydrogen desorption, which is much higher than the 0.1 J/m^2 we found for Ti/Mg/Ti at the same temperature.[84] Accounting for only one Mg/Fe interface being present and not two, the value $\Delta\gamma$ becomes 0.7 J/m^2 for a Mg/Fe interface. As mentioned earlier, what matters in practice for a hydrogen storage material is the actual desorption pressure. Compared to Ti/Mg/Ti, it has increased by more than a factor 2. This shows that—all else being equal (*e.g.* the same microstructure)—compared to Ti/Mg the MgH_2 is truly destabilized by the presence of the Mg/Fe interface.

Thus, if Mg is flat, Fe works perfectly fine to nanoconfine the Mg layer. In the previous section we observed that, when Mg grows as in the Fe/Mg/Fe samples, the grain boundaries in the Mg layer extend into the top Fe layer because of a epitaxial relation between Mg and Fe. We postulate that these GB's can now act as a diffusion pathway for Pd. A Mg layer in contact with Pd has been shown to greatly alter the hydrogenation thermodynamics of Mg,[58, 64] which we proposed to be due to

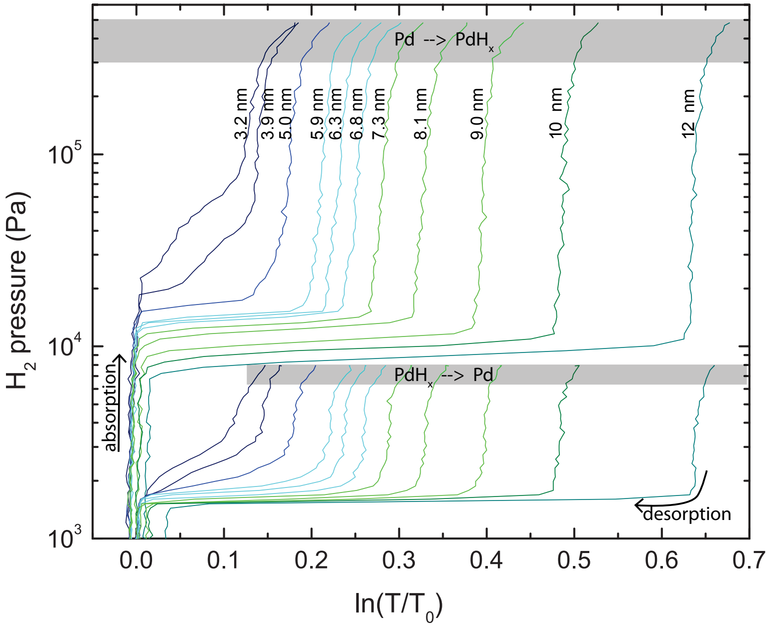

Figure 6.13 Isotherms of the 4th absorption cycle of a 10 nm Ti / Mg wedge / 10 nm Fe / 10 nm Pd multilayer recorded at 453 K for several Mg layer thicknesses. The gray boxes indicate the hydrogenation of the top Pd layer, which is visible in ab- and desorption. There is a strikingly large contrast with the Fe/Mg/Fe multilayers, which degraded heavily upon cycling with hydrogen at this temperature.

plastic deformation effects (Chapter 5). This mechanism would explain the double plateau and the Mg layer thickness dependence: The Pd rich regions are related to the upper plateau, and the Pd poor regions to the lower plateau. Furthermore, we know that the Mg grain size is roughly equal to the Mg thickness. Hence, the thinner the Mg layer, the more grain boundaries there are. This results in more Pd diffusion pathways in the Fe layer and therefore more Pd-rich regions will exist in thinner Mg layers than in thick ones. This logically explains why the upper plateau dominates thin Mg layers and is hardly present in thick Mg layers.

In our experiments on Pd-capped Mg, however, we found a large decrease in the plateau width which indicates that a significant amount of Mg is lost for hydrogenation. Here, in Figure 6.3 we observed that the plateau width is hardly affected, whatever the widths of the lower and upper plateaus. This may indicate that only very little Pd is needed to have a large effect on the hydrogenation behavior. Direct evidence for the presence of Pd in and around the GB's is needed to settle this question.

Finally, a remark on our observations in hydrogen desorption. The Fe/Mg/Fe multilayers have a constant desorption pressure, which in absolute terms is lower than for Ti-sandwiched Mg. We have also observed this for the desorption pressure of Pd-capped Mg and $Mg_{1-y}Pd_y$ alloys. In both these systems, we found voids in the layers cycled with hydrogen, which indicates that in desorption the creation of new surface is an energetically more favorable process than plastic deformation (see Chapter 5). What exactly causes the desorption pressures of MgH_2 in Pd/Mg and Fe/Mg/Fe to decrease compared to Ti/Mg/Ti is at present unclear. The fact that MgH_2 in the Ti/Mg/Fe sample desorbs at a higher pressure than Ti/Mg/Ti now strongly suggests that the Mg microstructure and its relation with the confining layer (Fe or Ti) is key. It would appear that the Ti layer (in Ti/Mg/Ti) is slightly more transparent for Pd than the Fe layer (in Ti/Mg/Fe), which results in the increased desorption pressures of MgH_2 in the latter sample. This transparency for Pd is a direct function of the number of defects in the Ti and Fe layers (*e.g.* grain boundaries). Apparently, the slightest contact of Mg with Pd will render useless any a destabilization effect (such as from the interface energy).

How exactly such a minute amount of Pd has such a drastic effect on the hydrogen sorption properties is unclear. We know that an increase in the hysteresis—as observed with increasing magnitude for Ti/Mg, Fe/Mg and Pd/Mg—is the result of an increase in the plastic deformation energy.[61, 60] We philosophize that the mechanical deformation mechanism that Mg undergoes upon hydrogenation is somehow altered by the Pd.

In summary, it is likely that a grain boundary free microstructure of the Mg and protective Fe layers is vital to avoid impurities such as Pd from reaching the Mg layer. Indeed, we observe a destabilization of MgH_2 in the microstructurally "clean"

Ti/Mg/Fe/Pd multilayers.

6.6 Conclusion

Summarizing our observations, we have seen that during hydrogen absorption there are two plateaus instead of one. From an analysis of the plateau width, we furthermore saw that, although the Mg seems stable at low temperature, at high temperature the Mg quickly degrades. Observing the trend of the plateau pressures with $1/d_{Mg}$, we find that the interface energy effect is very likely insufficient to explain the large spread in plateau pressures. Finally, in desorption we now see no double plateau and no change in the desorption pressure compared to bulk or Mg/Ti.

We conjecture that the number of high angle grain boundaries in the Mg layer is key when comparing the above observations with Ti/Mg/Ti multilayers, which are better behaved. The number of GB's is larger when Mg is grown on Fe than on Ti. These grain boundaries furthermore extend into the top Fe layer, thereby providing a diffusion pathway for Pd. This not only explains the instability at high temperature, but also the large increase of absorption plateau pressures and slight decrease of the desorption plateau pressures.

A reduction of the number of grain boundaries by growing Mg on Ti instead of Fe reveals that MgH_2 can indeed be destabilized by the presence of Fe. We directly observe this destabilization from an increase of the MgH_2 desorption pressure instead of from $\triangle H$ and $\triangle S$ values. This is important because the latter method hides the absolute hydrogen pressures, which is of utmost importance when discussing metal hydrides for hydrogen storage and sensing applications.

Thus, we show that the microstructure of the Mg layer and its protective layers should be controlled to achieve a maximum stability with temperature and cycling with hydrogen. This has important consequences for the design of thin film metal hydride based hydrogen sensors and nanoconfined metal hydrides for hydrogen storage.

Bibliography

[1] N. Stern, *The Economics of Climate Change: The Stern Review*, Crown, 2006.

[2] *Unburnable Carbon: Wasted capital and stranded assets*, ed. J. Leaton, Carbon Tracker, 2013.

[3] E. Musk, *Interview on Metaphysical Milkshake*, Soulpancake.com, 2013.

[4] N. N. Taleb, *The Black Swan: Second Edition*, Random House Trade, 2010.

[5] P. G. Bruce, S. A. Freunberger, L. J. Hardwick and J.-M. Tarascon, *Nat Mater*, 2011, **11**, 19–29.

[6] *Hydrogen as a Future Energy Carrier*, ed. A. Zuttel, A. Borgschulte and L. Schlapbach, Wiley-VCH, 2008.

[7] A. Fujishima and K. Honda, *Nature*, 1972, **238**, 37–38.

[8] *Photoelectrochemical Hydrogen Production*, ed. R. van de Krol and M. Gratzel, Springer, 2012.

[9] A. Zuttel, *materialstoday*, 2003, 24–33.

[10] L. Schlapbach and A. Zuttel, *Nature*, 2001, **414**, 353–358.

[11] H. van Mal, K. Buschow and A. Miedema, *J Less-Common Met*, 1974, **35**, 65–76.

[12] J. Kurtz, C. Ainscough, L. Simpson and M. Caton, *Hydrogen Storage Needs for Early Motive Fuel Cell Markets*, National Renewable Energy Laboratory Technical Report NREL/TP-5600-52783, 2012.

[13] P. Selvam, B. Viswanathan, C. Swamy and V. Srinivasan, *Int J Hydrogen Energ*, 1986, **11**, 169–192.

[14] J. Stampfer, C. Holley and J. Suttle, *J Am Chem Soc*, 1960, **82**, 3504–3508.

[15] J. Vajo, F. Mertens, C. Ahn, R. Bowman and B. Fultz, *J Phys Chem B*, 2004, **108**, 13977–13983.

[16] A. S. Ingason, A. K. Eriksson and S. Olafsson, *J Alloy Compd*, 2007, **446**, 530–533.

[17] F. J. Castro, V. Fuster and G. Urretavizcaya, *J Alloy Compd*, 2011, **509**, S595–S598.

[18] N. Takeichi, K. Tanaka, H. Tanaka, T. T. Ueda, Y. Kamiya, M. Tsukahara, H. Miyamura and S. Kikuchi, *J Alloy Compd*, 2007, **446**, 543–548.

[19] M. Gonzalez-Silveira, R. Gremaud, A. Baldi, H. Schreuders, B. Dam and R. Griessen, *Int J Hydrogen Energ*, 2010, **35**, 6959–6970.

[20] J. Cermak and L. Kral, *Int J Hydrogen Energ*, 2008, **33**, 7464–7470.

[21] D. Nagengast, A. van Gogh, E. Kooij, B. Dam and R. Griessen, *Appl Phys Lett*, 1999, **75**, 2050–2052.

[22] J. Isidorsson, I. Giebels, E. Kooij, N. Koeman, J. Rector, A. van Gogh and R. Griessen, *Electrochim Acta*, 2001, **46**, 2179–2185.

[23] H.-Y. Tien, M. Tanniru, C.-Y. Wu and F. Ebrahimi, *Int J Hydrogen Energ*, 2009, **34**, 6343–6349.

[24] G. Liang, J. Huot, S. Boily, A. V. Neste and R. Schulz, *J Alloy Compd*, 1999, **292**, 247.

[25] N. Hanada, T. Ichikawa and H. Fujii, *J Phys Chem B*, 2005, **109**, 7188–7194.

[26] H. Schimmel, J. Huot, L. Chapon, F. Tichelaar and F. Mulder, *J Am Chem Soc*, 2005, **127**, 14348–14354.

[27] B. Zahiri, C. T. Harrower, B. S. Amirkhiz and D. Mitlin, *Appl Phys Lett*, 2009, **95**, 103114.

[28] V. A. Vons, A. Anastasopol, W. J. Legerstee, F. M. Mulder, S. W. H. Eijt and A. Schmidt-Ott, *Acta Mater*, 2011, **59**, 3070–3080.

[29] X. Tan, B. Zahiri, C. M. B. Holt, A. Kubis and D. Mitlin, *Acta Mater*, 2012, **60**, 5646–5661.

[30] W. Oelerich, T. Klassen and R. Bormann, *J Alloy Compd*, 2001, **315**, 237–242.

[31] T. K. Nielsen, F. Besenbacher and T. R. Jensen, *Nanoscale*, 2011, **3**, 2086.

[32] A. Zaluska, L. Zaluski and J. Strom-Olsen, *J Alloy Compd*, 1999, **288**, 217–225.

[33] V. Berube, G. Chen and M. S. Dresselhaus, *Int J Hydrogen Energ*, 2008, **33**, 4122–4131.

[34] J. Gao, P. Adelhelm, M. H. W. Verkuijlen, C. Rongeat, M. Herrich, P. J. M. van Bentum, O. Gutfleisch, A. P. M. Kentgens, K. P. de Jong and P. E. de Jongh, *J Phys Chem C*, 2010, **114**, 4675–4682.

[35] T. K. Nielsen, K. Manickam, M. Hirscher, F. Besenbacher and T. R. Jensen, *ACS Nano*, 2009, **3**, 3521–3528.

[36] R. Bhakta, J. Herberg, B. Jacobs, A. Highley, R. B. Jr, N. Ockwig, J. Greathouse and M. Allendorf, *J Am Chem Soc*, 2009, **131**, 13198–13199.

[37] M. L. Christian and K. F. Aguey-Zinsou, *ACS Nano*, 2012, 1–13.

[38] J. Zou, X. Zeng, Y. Ying, X. Chen, H. Guo, S. Zhou and W. Ding, *Int J Hydrogen Energ*, 2013, **38**, 2337–2346.

[39] K.-J. Jeon, H. R. Moon, A. M. Ruminski, B. Jiang, C. Kisielowski, R. Bardhan and J. J. Urban, *Nat Mater*, 2011, **10**, 286–290.

[40] P. Ngene, M. R. van Zwienen and P. E. de Jongh, *Chem Commun*, 2010, **46**, 8201–8203.

[41] K. C. Kim, B. Dai, J. K. Johnson and D. S. Sholl, *Nanotechnology*, 2009, **20**, 204001.

[42] J. Huiberts, R. Griessen, J. Rector, R. Wijnaarden, J. Dekker, D. de Groot and N. Koeman, *Nature*, 1996, **380**, 231–234.

[43] F. den Broeder, S. van der Molen, M. Kremers, J. Huiberts, D. Nagengast, A. van Gogh, W. Huisman, N. Koeman, N. Koeman, B. Dam, J. Rector, S. Plota, M. Haaksma, R. Hanzen, R. Jungblut, P. Duine and R. Griessen, *Nature*, 1998, **394**, 656–658.

[44] S. van der Molen, J. Kerssemakers, J. Rector, N. Koeman, B. Dam and R. Griessen, *J Appl Phys*, 1999, **86**, 6107–6119.

[45] A. V. Gogh, D. Nagengast, E. Kooij, N. Koeman, J. Rector, R. Griessen, C. Flipse and R. Smeets, *Phys Rev B*, 2001, **63**, 195105.

[46] A. Borgschulte, W. Lohstroh, R. Westerwaal, H. Schreuders, J. Rector, B. Dam and R. Griessen, *J Alloy Compd*, 2005, **404**, 699–705.

[47] R. Gremaud, C. P. Broedersz, D. M. Borsa, A. Borgschulte, P. Mauron, H. Schreuders, J. H. Rector, B. Dam and R. Griessen, *Adv Mater*, 2007, **19**, 2813–2817.

[48] R. Gremaud, M. Slaman, H. Schreuders, B. Dam and R. Griessen, *Appl Phys Lett*, 2007, **91**, 231916.

[49] C. Langhammer, V. P. Zhdanov, I. Zorić and B. Kasemo, *Phys Rev Lett*, 2010, **104**, 135502.

[50] A. Baldi, *Ph.D. thesis*, VU University Amsterdam, Faculty of Sciences, Amsterdam, The Netherlands, 2010.

[51] R. Gremaud, J. L. M. van Mechelen, H. Schreuders, M. Slaman, B. Dam and R. Griessen, *Int J Hydrogen Energ*, 2009, **34**, 8951–8957.

[52] R. Gremaud, A. Borgschulte, C. Chacon, J. V. Mechelen, H. Schreuders, A. Zuttel, B. Hjorvarsson, B. Dam and R. Griessen, *Appl Phys A-Mater*, 2006, **84**, 77–85.

[53] D. M. Borsa, R. Gremaud, A. Baldi, H. Schreuders, J. H. Rector, B. J. Kooi, P. Vermeulen, P. H. L. Notten, B. Dam and R. Griessen, *Phys Rev B*, 2007, **75**, 205408.

[54] C. P. Broedersz, R. Gremaud, B. Dam, R. Griessen and O. M. Lovvik, *Phys Rev B*, 2008, **77**, 024204.

[55] Y. Pivak, *Ph.D. thesis*, Delft University of Technology, Faculty of Applied Sciences, Delft, The Netherlands, 2012.

[56] A. Baldi, G. K. Palsson, M. Gonzalez-Silveira, H. Schreuders, M. Slaman, J. H. Rector, G. Krishnan, B. J. Kooi, G. S. Walker, M. W. Fay, B. Hjorvarsson, R. J. Wijngaarden, B. Dam and R. Griessen, *Phys Rev B*, 2010, **81**, 224203.

[57] A. Baldi, *Ph.D. thesis*, VU University Amsterdam, Faculty of Sciences, Amsterdam, The Netherlands, 2010.

[58] A. Baldi, M. Gonzalez-Silveira, V. Palmisano, B. Dam and R. Griessen, *Phys Rev Lettt*, 2009, **102**, 226102.

[59] Y. Pivak, R. Gremaud, K. Gross, M. Gonzalez-Silveira, A. Walton, D. Book, H. Schreuders, B. Dam and R. Griessen, *Scripta Mater*, 2009, **60**, 348–351.

[60] Y. Pivak, H. Schreuders and B. Dam, *Crystals*, 2012, **2**, 710–729.

[61] Y. Pivak, H. Schreuders, M. Slaman, R. Griessen and B. Dam, *Int J Hydrogen Energ*, 2011, **36**, 4056–4067.

[62] A. Pundt, *Adv Eng Mater*, 2004, **6**, 11–21.

[63] A. Baldi, V. Palmisano, M. Gonzalez-Silveira, Y. Pivak, M. Slaman, H. Schreuders, B. Dam and R. Griessen, *Appl Phys Lett*, 2009, **95**, 071903.

[64] C.-J. Chung, S.-C. Lee, J. R. Groves, E. N. Brower, R. Sinclair and B. M. Clemens, *Phys Rev Lett*, 2012, **108**, 106102.

[65] R. von Helmolt and U. Eberle, *J Power Sources*, 2007, **165**, 833–843.

[66] R. Janot, L. Aymard, A. Rougier, G. Nazri and J. Tarascon, *J Mater Res*, 2003, **18**, 1749–1752.

[67] W. P. Kalisvaart, C. T. Harrower, J. Haagsma, B. Zahiri, E. J. Luber, C. Ophus, E. Poirier, H. Fritzsche and D. Mitlin, *Int J Hydrogen Energ*, 2010, **35**, 2091–2103.

[68] R. Gremaud, C. P. Broedersz, A. Borgschulte, M. J. van Setten, H. Schreuders, M. Slaman, B. Dam and R. Griessen, *Acta Mater*, 2010, **58**, 658–668.

[69] D. Kyoi, T. Sato, E. Ronnebro, N. Kitamura, A. Ueda, M. Ito, S. Katsuyama, S. Hara, D. Noreus and T. Sakai, *J Alloy Compd*, 2004, **372**, 213–217.

[70] K.-F. Aguey-Zinsou and J.-R. Ares-Fernandez, *Chem Mater*, 2008, **20**, 376–378.

[71] S. B. Kalidindi and B. R. Jagirdar, *Inorg Chem*, 2009, **48**, 4524–4529.

[72] R. Bogerd, P. Adelhelm, J. H. Meeldijk, K. P. de Jong and P. E. de Jongh, *Nanotechnology*, 2009, **20**, 204019.

[73] V. Berube, G. Radtke, M. Dresselhaus and G. Chen, *Int J Energ Res*, 2007, **31**, 637–663.

[74] M. Fichtner, *Nanotechnology*, 2009, **20**, 204009.

[75] R. Schwarz and A. Khachaturyan, *Acta Mater*, 2006, **54**, 313–323.

[76] S. X. Tao, P. H. L. Notten, R. A. van Santen and A. P. J. Jansen, *Phys Rev B*, 2010, **82**, 125448.

[77] A. Zuttel, P. Wenger, P. Sudan, P. Mauron and S. Orimo, *Mat Sci Eng B-Solid*, 2004, **108**, 9–18.

[78] E. Callini, L. Pasquini, E. Piscopiello, A. Montone, M. V. Antisari and E. Bonetti, *Appl Phys Lett*, 2009, **94**, 221905.

[79] P. E. de Jongh, *Nature Publishing Group*, 2011, **10**, 265–266.

[80] A. Anastasopol, T. V. Pfeiffer, A. Schmidt-Ott, F. M. Mulder and S. W. H. Eijt, *Appl Phys Lett*, 2011, **99**, 194103.

[81] F. M. Mulder, S. Singh, S. Bolhuis and S. W. H. Eijt, *J Phys Chem C*, 2012, **116**, 2001–2012.

[82] M. Wagemaker, F. M. Mulder and A. V. D. Ven, *Adv Mater*, 2009, **21**, 2703–+.

[83] R. Malik, F. Zhou and G. Ceder, *Nat Mater*, 2011, **10**, 587–590.

[84] L. P. A. Mooij, A. Baldi, C. Boelsma, K. Shen, M. Wagemaker, Y. Pivak, H. Schreuders, R. Griessen and B. Dam, *Acta Mater*, 2011, **1**, 754–758.

[85] J. Ryden, B. Hjörvarsson, T. Ericsson, E. Karlsson, A. Krozer and B. Kasemo, *J Less-Common Met*, 1989, **152**, 295–309.

[86] D. Wang, T. B. Flanagan and T. Kuji, *Phys Chem Chem Phys*, 2002, **4**, 4244–4254.

[87] H. Fujii, K. Higuchi, K. Yamamoto, H. Kajioka, S. Orimo and K. Toiyama, *Mater Trans*, 2002, **43**, 2721–2727.

[88] A. Pundt and R. Kirchheim, *Annu Rev Mater Res*, 2006, **36**, 555–608.

[89] T. Flanagan, C. Park and W. Oates, *Prog Solid State Ch*, 1995, **23**, 291–363.

[90] J. Sethna, K. Dahmen, S. Kartha, J. Krumhansl, B. Roberts and J. Shore, *Phys Rev Lettt*, 1993, **70**, 3347–3350.

[91] J. A. Dura, S. T. Kelly, P. A. Kienzle, J. H. Her, T. J. Udovic, C. F. Majkrzak, C. J. Chung and B. M. Clemens, *J Appl Phys*, 2011, **109**, 093501.

[92] S. W. H. Eijt, H. Leegwater, H. Schut, A. Anastasopol, W. Egger, L. Ravelli, C. Hugenschmidt and B. Dam, *J Alloy Compd*, 2011, **509**, S567–S571.

[93] E. Machlin, *T Am I Min Met Eng*, 1953, **197**, 437–445.

[94] D. Turnbull, *T Am I Min Met Eng*, 1951, **191**, 661–665.

[95] J. W. Christian, *The Theory of Transformations in Metals and Alloys: Part I*, Pergamon, 3rd edn., 2002.

[96] Z. T. Trautt, M. Upmanyu and A. Karma, *Science*, 2006, **314**, 632–635.

[97] A. Pedersen, J. Kjøller, B. Larsen and B. Vigeholm, *Int J Hydrogen Energ*, 1983, **8**, 205–211.

[98] W. Burton, N. Cabrera and F. Frank, *Philos Tr R Soc S-A*, 1951, **243**, 299–358.

[99] B. van der Hoek, J. van der Eerden and P. Bennema, *J Cryst Growth*, 1982, **56**, 108–124.

[100] P. Huang, F. Wang, M. Xu, T. J. Lu and K. W. Xu, *Mat Sci Eng A-Struct*, 2011, **528**, 5908–5913.

[101] C. E. Carlton and P. J. Ferreira, *Acta Mater*, 2007, **55**, 3749–3756.

[102] J. Zhang, Y. C. Zhou, Z. S. Ma, L. Q. Sun and P. Peng, *Int J Hydrogen Energ*, 2013, **38**, 3661–3669.

[103] B. Yang, Y.-P. He and Y.-P. Zhao, *Appl Phys Lett*, 2011, **98**, 081905.

[104] P. Adelhelm, K. P. de Jong and P. E. de Jongh, *Chem Commun*, 2009, 6261–6263.

[105] L. Mooij and B. Dam, *Phys Chem Chem Phys*, 2013, **15**, 2782–2792.

[106] M. Avrami, *J Chem Phys*, 1939, **7**, 1103–1112.

[107] W. Johnson and R. Mehl, *T Am I Min Met Eng*, 1939, **135**, 416–442.

[108] K. Nörthemann and A. Pundt, *Phys Rev B*, 2011, **83**, 155420.

[109] J. J. D. Yoreo and P. G. Vekilov, *Rev Mineral Geochem*, 2003, **54**, 57–93.

[110] D. A. Porter and K. E. Easterling, *Phase Transformations in Metals and Alloys*, CRC Press, 2nd edn., 2004.

[111] R. Kirchheim, *Scripta Mater*, 2010, **62**, 67–70.

[112] A. Remhof and A. Borgschulte, *ChemPhysChem*, 2008, **9**, 2440–2455.

[113] B. Dam, R. Gremaud, C. P. Broedersz and R. Griessen, *Scripta Mater*, 2007, **56**, 853–858.

[114] H. Oesterreicher, J. Clinton and H. Bittner, *Mater Res Bull*, 1976, **11**, 1241–1247.

[115] J. Huot, A. Yonkeu and J. Dufour, *J Alloy Compd*, 2009, **475**, 168–172.

[116] L. Mooij and B. Dam, *Phys Chem Chem Phys*, 2013, **15**, 11501–11510.

[117] P. E. de Jongh and P. Adelhelm, *ChemSusChem*, 2010, **3**, 1332–1348.

[118] S. Zheng, K. Wang, V. Oleshko and L. Bendersky, *J Phys Chem C*, 2012, **116**, 21277–21284.

[119] Z. Tan, C. Chiu, E. J. Heilweil and L. A. Bendersky, *Int J Hydrogen Energ*, 2011, **36**, 9702–9713.

[120] F. Salah, B. Harzallah and A. van der Lee, *J Appl Crystallogr*, 2007, **40**, 813–819.

[121] A. Krozer and B. Kasemo, *J Less-Common Met*, 1990, **160**, 323–342.

[122] M. Bjorck and G. Andersson, *J Appl Crystallogr*, 2007, **40**, 1174–1178.

[123] S. Hong, *Curr Appl Phys*, 2003, **3**, 457–460.

[124] M. Rost, *Phys Rev Lett*, 2007, **99**, 266101.

[125] B. Bogdanovic, A. Reiser, K. Schlichte, B. Spliethoff and B. Tesche, *J Alloy Compd*, 2002, **345**, 77–89.

[126] W. P. Kalisvaart, A. Kubis, M. Danaie, B. S. Amirkhiz and D. Mitlin, *Acta Mater*, 2011, **59**, 2083–2095.

Summary

Magnesium hydride is a potential hydrogen storage material, which is a key component in a renewable energy system based on hydrogen. Magnesium can store up to 7.6 wt% of hydrogen, with a volumetric hydrogen density higher than that of liquid hydrogen. In bulk form, magnesium hydride (MgH_2) is very stable, which means that hydrogen is released only at elevated temperature. Furthermore, the kinetics of hydrogen sorption is slow, which further hampers the practical use of this hydrogen storage material. A solution to both these issues may be found in nanoconfinement. At the nanoscale, the contribution of the surface (or interface) energy starts to play a role and has the potential to destabilize the magnesium hydride. Also the kinetics is expected to improve due to the increased surface area and shorter diffusion lengths. To study nanoconfinement in powder samples is not trivial due to agglomeration effects (loss of surface area) and sample inhomogeneity.

Here, we use a thin film model system in which the confinement of magnesium can be directly controlled by changing the local environment of magnesium in two ways: Firstly, by changing the thickness of the magnesium layer we directly control the surface-to-volume ratio. Secondly, by changing the materials surrounding the magnesium layer (sandwich layers) the nature of the interaction can be changed. We study the hydrogen sorption properties of these thin film multilayers with Hydrogenography, an optical technique that uses the change in optical transmission that many materials undergo upon absorption of hydrogen. This effect is especially large for the hydrogenation of the Mg metal to the MgH_2 insulator, thereby making it possible to easily measure the hydrogenation of single thin Mg layers down to a thickness of 1 nm.

Using this thin film model system, we first study the effect of the interface energy on the hydrogenation thermodynamics of Mg nanoconfined by TiH_2. From theory, it is expected that the change in the interface (or surface) energy that occurs upon (de-)hydrogenation either stabilizes or destabilizes the metal hydride phase. For thin magnesium layers sandwiched between TiH_2 we find experimentally that the magnesium hydride phase is destabilized compared to bulk magnesium hydride, if it is made sufficiently thin. We confirm these results with DFT calculations of the interface energies of MgH_2/TiH_2 and Mg/TiH_2. The destabilization we observe in our thin films is equivalent to an order of magnitude increase in equilibrium pressure for a hypothetical 1.8 nm Mg nanoparticle.

From theory, one expects that this destabilization acts equally on the ab- and desorption branches of the hysteresis. We find, however, that the equilibrium pressure increases with decreasing layer thickness more strongly in absorption than in desorption. Hence, the hysteresis increases with decreasing Mg layer thickness. To investigate the nature of this increase we perform sub-hysteresis cycles—i.e. incomplete isotherms—which should reveal the effects of nucleation and growth. We measure sub-hysteresis isotherms for both a 3.1 nm and a 10 nm Mg layer, which surprisingly shows that the nucleation barrier of MgH_2 increases the observed plateau pressure for hydrogen absorption of the 10 nm layer, but not for the 3.1 nm layer. This points at different mechanisms for hydride phase nucleation and growth as a function of the Mg layer thickness.

In the 10 nm magnesium layer, the nucleation barrier can in fact be used to our advantage when we apply a low hydrogen over-pressure, i.e. a low driving force (70 Pa H_2 at 90 °C). In this case, the nucleation rate is so low that the number of MgH_2 nuclei is very low. The limited number of MgH_2 nuclei (or domains) implies that these MgH_2 domains are free to grow with a small probability of being impinged by another domain. In fact, by observing these samples for many hours, we can detect by eye the in-plane 2D growth process of MgH_2 domains up to millimeters in size. The visibility of the MgH_2 domains allows for a careful examination of the growth processes. We use the Johnson-Mehl-Avrami-Kolmogorov (JMAK) model of the kinetics of solid-state phase transformations to first analyze the eye-visible transformation to MgH_2 of 10 nm Mg layers. From this analysis we confirm what we already could detect by eye: The TiH_2 domains grow 2-dimensionally. Then, we apply JMAK to cases where an analysis by eye is not possible, because the growth process occur on a smaller scale than we can detect. For hydrogenation at somewhat higher pressure (100 Pa H2 at 90 oC), we find that 2D growth of the hydride phase is still the most likely mechanism. The analysis of the nucleation and growth processes furthermore reveals that the growth rate is limited by the plastic deformation energy of the Mg and the protective TiH_2 and Pd layers that are deposited on top of the Mg. Plastic deformation occurs because the volume expansion of Mg transforming to MgH_2 is 30%. The only way to accommodate this expansion of the clamped thin film is by a 30% increase of the layer thickness.

Upon hydrogen desorption, we find no effect of the plastic deformation energy. We deduce that this is due to the large mechanical asymmetry between hydrogen ab- and desorption: In absorption, the Mg layer has to expand during the actual hydrogen uptake while in desorption—as an alternative to contraction—new surfaces and voids may be created. Thus, temporarily a highly porous Mg layer is expected to form. This interpretation is confirmed by the observation of a very fast rehydrogenation if performed soon after a dehydrogenation. If the rehydrogenation is performed after several hours, such a fast rehydrogenation is not possible anymore.

So far, in all our experiments, the Mg layers were protected by surrounding Ti layers. Although polycrystalline in nature, these multilayers are highly textured and grow with flat interfaces that remain flat upon cycling with hydrogen. Upon exchanging the

Ti layers for other materials, such as Pd and Fe, drastic changes in the kinetics and thermodynamics of hydrogenation of the Mg layer occur. We find that these changes can again be related to plastic deformation, albeit aided by the effects of alloying and microstructure.

If the top catalytic Pd layer is directly deposited on the Mg layer, large changes in the thermodynamics of hydrogenation were observed. From an analysis of both ab- and desorption isotherms, we conclude that the previously proposed elastic clamping model and the interface alloy model do not grasp the underlying nature of the changes in hydrogenation thermodynamics of Pd-capped magnesium layers. We compare Pd-capped Mg layers with deliberately made $Mg_{1-y}Pd_y$ alloys, and indeed find many similarities, most notably the formation of voids within these thin films upon cycling with hydrogen. Contrary to the Ti-sandwiched Mg layers, here we find direct evidence of voids that remain stable.

Our studies show that there is a complex relation between the microstructure development studied with TEM and XRD and hydrogen sorption characteristics, which complicates the formulation of a quantitative model. This leads us to propose a qualitative model, which emphasizes the effects of mechanical deformation and hydride nucleation. In hydrogen absorption, the volume expansion is only possible via plastic deformation of the multilayer, while in desorption the creation of free surface is the energetically more favorable pathway. The required plastic deformation energy results in a large increase in the absorption plateau pressure, while the formation of free surfaces (and thereby voids) during desorption—a process which we find is independent of the local environment of MgH_2—hardly influences the desorption plateau pressure.

The importance of good control over the microstructure of the Mg and surrounding layers becomes evident from Fe-sandwiched Mg layers. From XRD we find that the resulting multilayer is textured, with Fe (110) —— Mg (0001) —— substrate. With Hydrogenography, we find that during hydrogen absorption there are two plateaus instead of the expected single one. From an analysis of the plateau width, we furthermore find that, although the Mg seems stable at low temperature, at high temperature (¿150 °C) the Mg quickly degrades. Observing the trend of the plateau pressures with $1/d_{Mg}$, we find that an interface energy effect is insufficient to explain the large spread in plateau pressures. Finally, in desorption we now see no double plateau and no change in the desorption pressure compared to bulk or Ti-sandwiched Mg layers. From cross section transmission electron microscopy we find that the relatively poor texturing of the Fe layers results in the presence of high angle grain boundaries (GB's) in the Mg layers. We conjecture that the number of high angle grain boundaries in the Mg layer is key when comparing the above observations with Ti/Mg/Ti multilayers, in which the Ti layers grow highly oriented to the substrate. The number of GB?s is larger when Mg is grown on Fe than on Ti. These grain boundaries furthermore extend into the top Fe layer, thereby providing a diffusion pathway for Pd. This not only explains the instability at high temperature, but also the large increase of the absorption plateau pressures and slight decrease of the desorption plateau pressures.

As a proof of principle, we exchange the lower Fe layer with Ti, thereby allowing the Mg layer to grow with a low number of high angle GB's. Again a Fe layer is deposited on the Mg layer, which reveals that MgH_2 is destabilized by the presence of Fe, and more so than by Ti. We directly observe this destabilization from an increase of the MgH_2 desorption pressure.

As a general conclusion, we find that the interface energy does affect the thermodynamics of hydrogenation of magnesium. The magnitude of this effect is, however, relatively small especially compared to the effects of plastic deformation and alloying. The latter two effects are also expected to occur in, for instance, nano-infiltrated metal hydrides.

Furthermore, we conclude that one needs to fully characterize the temperature and thickness dependence of both the hydrogen ab- and desorption plateau pressures in order to obtain insight into the thermodynamics of hydrogenation. Often, conclusions on the destabilization of a metal hydride are based on hydrogen absorption alone. In our research, we find large differences in the magnitude of nano effects on the ab- and desorption isotherms. This is especially important when investigating nanosized metal hydrides that are to be destabilized compared to their bulk equivalents.

Samenvatting

Waterstofopslag is een essentieel onderdeel van een duurzaam energiesystem met waterstof als energiedrager. Magnesiumhydride (MgH_2) is een potentieel waterstofopslagmateriaal, met een gewichtspercentage waterstof van 7.6%. Tegelijkertijd is de volumetrische dichtheid van waterstof in MgH_2 groter dan van vloeibaar waterstof. Jammer genoeg is magnesiumhydride zeer stabiel, wat betekent dat waterstof slechts bij verhoogde temperatuur vrijkomt. Daarbij is de kinetiek van de ab- en desorptie van waterstof traag, wat de praktische toepassing van magnesiumhydride als waterstofopslagmateriaal verder belemmert. Een oplossing voor deze twee kwesties ligt potentieel in de opsluiting van MgH_2 op nanoschaal, ofwel nano-opsluiting. Op de nanoschaal begint de contributie van oppervlakte- (en grensvlak-)spanning een rol te spelen in de thermodynamica van waterstofsorptie, wat het mogelijk maakt magnesiumhydride te destabiliseren. Daarbij verbetert de kinetiek door de verkleining van de gemiddelde padlengte voor waterstofdiffusie. Het is echter niet triviaal om de effecten van nano-opsluiting te bestuderen in poedermonsters, omdat agglomeratie (gepaard gaande met een verlies van vrije oppervlakte) en monsterinhomogeniteit moeilijk te vermijden zijn.

In dit onderzoek gebruiken we een dunne film modelsysteem waarin, door de lokale omgeving van magnesium te veranderen, de nano-opsluiting van magnesium op twee manieren wordt gestuurd: Ten eerste kunnen we door de dikte van de magnesiumlaag te variëren direct de oppervlakte-volume ratio veranderen. Ten tweede kunnen we het materiaal kiezen dat de magnesiumlaag omringt, waardoor het karakter van de grensvlakinteractie kan worden aangepast. We bestuderen de waterstofsorptie-eigenschappen van deze dunne film multilagen met behulp van Hydrogenografie. Dit is een optische techniek die de verandering van optische transmissie ten gevolge van de introductie van waterstof meet. De verandering van optische transmissie is zeer groot bij de omzetting van het Mg metaal naar de MgH_2 isolator. Hierdoor is de hydrogenatie van een Mg laag dunner dan 1 nm te meten. Met behulp van dit dunne film modelsysteem bestuderen we allereerst het effect van de grensvlakspanning op de thermodynamica van hydrogenatie van Mg nano-opgesloten door TiH_2. Op basis van theorie verwachten we dat de verandering van de grensvlakspanning ten gevolge van hydrogenatie de metaalhydridefase stabiliseert dan wel destabiliseert, afhankelijk van het verschil tussen de grensvlakspanningen van de metaalhydridefase en de metaalfase. Voor Mg-lagen dunner dan 10 nm en geplaatst tussen twee TiH_2-lagen vinden we experimenteel dat de magnesiumhydridefase gedestabiliseerd wordt in vergelijking met bulk-magnesiumhydride. Deze resultaten worden bevestigd door dichtheidsfunctionaaltheorie-berekeningen van de grensvlakspanningen van de MgH_2/TiH_2 en Mg/TiH_2 grensvlakken. De destabilisatie die wij observeren in de MgH_2 dunne films betekent dat een hypothetisch Mg-nanodeeltje met een diameter van 1,8 nm en omgeven door TiH_2 een tien keer grotere plateaudruk zal hebben in vergelijking tot bulk MgH_2.

Hoewel we, theoretisch gezien, verwachten dat deze destabilisatie een gelijke werking heeft op de waterstof ab- en desorptietakken van de hysterese, vinden we dat voor waterstof-absorptie de plateaudruk sterker verhoogd wordt als functie van de krimpende Mg-laagdikte dan voor waterstof-desorptie. Dit betekent dat de hysterese groter wordt bij kleinere laagdikte. Om de aard van deze groei in hysterese te onderzoeken, voeren we sub-hysteresescans uit. Dit zijn metingen van incomplete isothermen waarbij de richting (waterstofab- of de-sorptie) wordt gewisseld voordat de volledige fasetransformatie is voltooid. Deze scans kunnen het effect van nucleatie en groei op de gemeten hysterese onthullen. We voeren subhysteresescans uit op monsters met een Mg-laagdikte van 3,1 nm en 10 nm en we zien dat er inderdaad een nucleatiebarrière werkzaam is op de plateaudruk. Verrassend genoeg geldt dit slechts voor het monster met 10 nm Mg, maar niet voor het monster met 3,1 nm Mg. Dit geeft aan dat het vormingsmechanisme van magnesiumhydride verschilt voor veranderende Mg-laagdikte.

De aanwezigheid van de nucleatiebarrière in de 10 nm Mg-laag gebruiken we tot ons voordeel door bij een lage waterstofoverdruk, ofwel een lage drijvende kracht (70 Pa H2 bij 90 °C), de groei nader te onderzoeken. Onder deze condities is de nucleatiesnelheid zeer laag te opzichte van de groeisnelheid en het aantal gevormde MgH_2-nuclei blijft hierdoor beperkt. Het aantal nuclei is zo laag dat de gevormde MgH_2-domeinen vrij zijn te groeien zonder door andere MgH_2-domeinen belemmerd te worden. Door de monsters vele uren lang te observeren, kunnen we individuele MgH_2-domeinen met het blote oog detecteren. De zichtbaarheid van de MgH_2-domeinen laat een gedetailleerd onderzoek van het groeiproces toe. We gebruiken hiertoe het Johnson-Mehl-Avrami-Kolmogorov-model (JMAK-model) van de kinetiek van vaste-stof fasetransformaties. Deze analyse bevestigt onze eerdere observatie met het blote oog: De MgH_2-domeinen groeien 2-dimensionaal. Hierna passen we het JMAK-model toe op situaties waarbij een analyse met het blote oog niet mogelijk is, omdat de nucleatie- en groeiprocessen plaats vinden op een kleinere schaal dan de zichtbare. Voor de hydrogenatie bij een hogere waterstofdruk (100 Pa H2 bij 90 °C) vinden we dat het meest waarschijnlijke mechanisme wederom 2-dimensionale groei van MgH_2 is.

De analyse van het nucleatie- en groeimechanisme onthult verder dat de groeisnelheid gelimiteerd wordt door de plastische deformatie-energie van de Mg- lagen zelf en de beschermende TiH_2- en Pd-lagen die op het Mg gegroeid zijn. Plastische deformatie is het gevolg van de grote volume-expansie van ongeveer 30% die gepaard gaat met de transformatie van Mg naar MgH_2. De enige manier waarop deze expansie van de aan het substraat vastzittende Mg-laag geaccommodeerd kan worden, is door een 30% vergroting van de laagdikte.

In tegenstelling tot waterstofabsorptie, vinden we tijdens de waterstofdesorptie geen effect van de plastische deformatie-energie. We leiden hieruit een grote mechanische asymmetrie tussen waterstof ab- en desorptie af: Tijdens absorptie moet de Mg laag expanderen gedurende de eigenlijke waterstofabsorptie, terwijl tijdens desorptie, als alternatief voor contractie, nieuwe oppervlakken en holtes gevormd kunnen worden. Dit betekent dat, op zijn minst tijdelijk, een poreuze Mg-laag wordt gevormd. Deze interpretatie wordt bevestigd door de observatie van zeer snelle rehydrogenatie indien deze wordt uitgevoerd kort na de dehydrogenatie. Wanneer de rehydrogenatie enkele uren na de dehydrogenatie wordt uitgevoerd, heeft de rehydrogenatie eenzelfde snelheid als een “normale” hydrogenatie.

Tot dusver zijn de Mg-lagen in al onze experimenten omringd door Ti lagen. Hoewel de multilagen polykristallijn van aard zijn, hebben ze een duidelijke preferente oriëntatie en groeien ze met een relatief vlak oppervlakte. Zodra de Ti-lagen vervangen worden door andere materialen zoals Pd en Fe, vinden we drastische veranderingen in zowel de kinetiek als de thermodynamica van waterstofsorptie van de Mg-laag. We vinden dat deze veranderingen wederom kunnen worden gerelateerd aan plastische deformatie, hetzij dat de plastische deformatie in dit geval beïnvloed wordt door menging bij het grensvlak en door de microstructuur.

Wanneer de bovenste, katalytische Pd-laag direct op de Mg-laag gedeponeerd wordt, zijn grote veranderingen in de thermodynamica van hydrogenatie geobserveerd. Van een analyse van zowel de ab- als desorptie isothermen, concluderen we dat de eerder geponeerde modellen, die gebaseerd zijn op de effecten van elastische vastklemming en grensvlaklegeringen, de onderliggende aard van verandering van thermodynamica van Pd-afgesloten Mg-lagen niet volledig beschrijven. We vergelijken Pd-afgesloten Mg-lagen met doelbewust gemaakte $\mathrm{Mg}_{1-y}\mathrm{Pd}_y$-legeringen en vinden vele overeenkomsten, met als meest opmerkelijke uitkomst de vorming van holtes in deze dunne lagen na schakelen met waterstof. In tegenstelling tot Ti-afgesloten Mg-lagen, vinden we in dit geval dat de holtes in dit geval stabiel zijn.

Ons onderzoek laat zien dat er een complexe relatie bestaat tussen de ontwikkeling van de microstructuur, zoals bestudeerd met transmissie-elektronenmicroscopie en röntgendiffractie, en de waterstofsorptie-eigenschappen. Deze complexe relatie bemoeilijkt het formuleren van een kwantitatief model, wat ons heeft geleid tot het formuleren van een kwalitatief model. Dit model benadrukt de effecten van mechanische deformatie en hydride nucleatie. In absorptie is de volume-expansie slechts mogelijk via plastische deformatie van de multilaag, terwijl in desorptie de vorming van vrije oppervlakken een energetisch voordeliger pad is. De benodigde plastische deformatie-energie resulteert in een verhoogde plateaudruk van waterstofabsorptie, terwijl de formatie van vrije oppervlakten (en daarbij holtes)—die onafhankelijk blijkt te zijn van de lokale omgeving van het MgH_2—ervoor zorgt dat de plateaudruk van waterstofdesorptie vrijwel ongemoeid blijft.

Het belang van een goede controle op de microstructuur van de Mg- en omringende lagen wordt duidelijk aan de hand van de structurele karakterisatie van Fe-omringde Mg-lagen. Met röntgendiffractie zien we dat deze Fe/Mg multilagen preferente groei kennen, net als de Ti/Mg multilagen. Hierbij vinden we dat het Fe(110)-vlak parallel is aan het Mg(0001)-vlak, met beide vlakken parallel aan het substraat. In tegenstelling tot Ti/Mg vinden we met Hydrogenografie twee plateaudrukken in absorptie. Uit een analyse van de plateaubreedtes vinden we dat het Mg stabiel blijkt te zijn na schakelen met waterstof, maar dat het snel degradeert na schakelen bij hoge temperatuur (¿150 °C). De trend in de plateaudrukken als functie van $1/d_{Mg}$ laat zich in dit geval moeilijk met een grensvlakenergie-effect verklaren. De waterstofdesorptie-isothermen hebben, in tegenstelling tot waterstofabsorptie, een enkel plateau en geen verandering van de plateaudrukken ten opzichte Ti/Mg of Mg in bulkvorm. Met behulp van dwarsdoorsnede transmissie-elektronenmicroscopie zien we dat de kristaloriëntatie van de Fe-lagen meer varieert dan van de Ti-lagen. Deze spreiding in kristaloriëntatie zorgt ervoor dat er een vergroot aantal korrelgrenzen in de Mg-lagen te vinden zijn. We veronderstellen dat het aantal korrelgrenzen een bepalende rol speelt voor het gedrag van Fe-omringde Mg-lagen in vergelijking met Ti-omringde Mg-lagen. Het aantal korrelgrenzen in de Mg-laag is groter wanneer ze op Fe groeit dan wanneer ze op Ti groeit. Deze korrelgrenzen worden daarbij ook overgenomen door de bovenste Fe-laag, waardoor er een diffusiepad voor Pd ontstaat. Dit zou niet alleen de instabiliteit bij hoge temperatuur van de Fe-omringde Mg-lagen verklaren, maar ook de verhoging van de plateaudrukken voor waterstofabsorptie en onveranderde plateaudrukken voor waterstofdesorptie.

Als test voor deze korrelgrenshypothese verwisselen we de onderste Fe-laag door een Ti-laag, waarop een Mg-laag gegroeid kan worden met een klein aantal korrelgrenzen. Hierna wordt er wederom een Fe-laag op de Mg-laag gedeponeerd. Hydrogenografiemetingen van deze monsters laten zien dat het MgH_2 is gedestabiliseerd door het grensvlak met de Fe-laag. De destabilisatie is in dit geval sterker dan wanneer het Mg louter met Ti omringd is, wat we direct observeren door de verhoging van de plateaudruk van waterstofdesorptie van het MgH_2. Dit betekent dat destabilisatie van MgH_2 door nano-opsluiting met Fe inderdaad mogelijk is.

Als algemene conclusie stellen wij dat de grensvlakenergie inderdaad een verandering van de thermodynamica van de hydrogenatie van magnesium teweeg kan brengen. De grootte van dit effect is echter relatief klein in vergelijking met de effecten van plastische deformatie en de vorming van legeringen. Van deze laatste twee effecten verwachten we dat zij ook sterk van invloed zullen zijn op de kinetiek en thermodynamica van, bijvoorbeeld, nano-geïnfiltreerde metal hydriden.

Verder concluderen we dat het van groot belang is de volledige dikte- en temperatuurafhankelijkheid van zowel de ab- als desorptie plateaudrukken te analyseren, voordat enige conclusies ten aanzien van (verandering van) de thermodynamica van hydrogenatie gemaakt kunnen worden. Vaak worden deze conclusies echter gemaakt slechts op basis van metingen van de waterstofabsorptie-isothermen. Ons onderzoek laat zien dat er grote verschillen kunnen zijn tussen nano-effecten op de waterstof ab- en desorptieprocessen. Dit is belangrijk, in het bijzonder wanneer gezocht wordt naar nano-metaalhydriden die ge(de)stabiliseerd zijn ten opzichte van dezelfde metaalhydriden in bulkvorm.

List of publications

1. Y. Liang, T. Tsubota, L.P.A. Mooij, R. van de Krol, *Highly Improved Quantum Efficiencies for Thin Film* $BiVO_4$ *Photoanodes*, J Phys Chem C 115, 2011, 17594-17598.

2. L.P.A. Mooij, A. Baldi, Ch. Boelsma, K. Shen, M. Wagemaker, Y. Pivak, H. Schreuders, R. Griessen, B. Dam, *Interface Energy Controlled Thermodynamics of Nanoscale Metal Hydrides*, Adv Energy Mater 1, 2011, 754-758.

3. T. Mongstad, Ch. Platzer-Björkman, J.P. Maehlen, L.P.A. Mooij, Y. Pivak, B. Dam, E.S. Marstein, B.C. Hauback, S. Zh. Karazhanov, *A new thin film photochromic material: Oxygen-containing yttrium hydride*, Solar Energy Materials & Solar Cells 95, 2011, 3596-3599.

4. Q. Zhen, Y. Pivak, L.P.A. Mooij, A.M.J. van der Eerden, H. Schreuders, P.E. de Jongh, J.H. Bitter, B. Dam, *EXAFS investigation of the destabilization of the Mg-Ni-Ti (H) system*, Int J Hydrogen Energ 37, 2012, 4161-4169.

5. Lennard Mooij and Bernard Dam, *Hysteresis and the role of nucleation and growth in the hydrogenation of Mg nanolayers*, Phys Chem Chem Phys 15, 2013, 2782-2792.

6. R.J. Westerwaal, J.S.A. Rooijmans, L. Leclercq, D.G. Gheorghe, T. Radeva, L. Mooij, T. Mak, L. Polak, M. Slaman, B. Dam, *Nanostructured Pd-Au based fiber optic sensors for probing hydrogen concentrations in gas mixtures*, Int J Hydrogen Energ 38, 2013, 4201.

7. Lennard Mooij and Bernard Dam, *Nucleation and growth mechanisms of nano magnesium hydride from the hydrogen sorption kinetics*, Phys Chem Chem Phys 15, 2013, 11501-11510.

8. Y. Pivak, L.P.A. Mooij, H. Schreuders, B. Dam, *Destabilization effect in* $Mg_{1-x-y}Ti_xAl_yH_z$ *films as studied by Hydrogenography.*
   In preparation.

9. L. Mooij, T. Perkisas, G. Pálsson, M. Wolff, H. Schreuders, B. Hjörvarsson, G. van Tendeloo, S. Bals, B. Dam, *The effect of microstructure on the hydrogenation of Mg/Fe thin film multilayers*.
   In preparation.

10. L. Mooij, A. Baldi, G. Krishnan, B.J. Kooi, R. Griessen, B. Dam, *Hydrogenation of Mg/Pd alloys and multilayers*.
    In preparation.

Acknowledgements

Here I would like to shortly but fervently acknowledge everyone who has contributed—in the broadest sense of the word—to the coming together of this thesis.

My supervisor, Bernard Dam, is greatly appreciated for giving me the freedom to explore the many sidetracks I walked into. I like to think that I did finally start learning to 'focus', but it may of course be merely an illusion. Bernard's super fast revisions of papers and parts of this thesis helped to keep me going, I guess especially in the last couple of months! Yet, Bernard's contribution goes beyond science and practicalities, with his philosophical nature and diplomatic pragmatism in life at its basis.

Also, my gratitude goes out to Ronald Griessen, who's enthusiasm and solid knowledge are always an inspiration. New ideas naturally follow from, or arise in, a conversation with him.

Furthermore, I very much appreciate the fruitful collaboration with Tyché Perkisas and Sara Bals from the University of Antwerp; Gunnar Pálsson, Max Wolff and Björgvin Hjörvarsson from Uppsala University; Gopi Krishnan and Bart Kooi from the University of Groningen; and Anca Anastasopol and and Stephan Eijt from the TU Delft.

For many of the past six or so years I've been so lucky to be a member the MECS group. This full sentence I dedicate without hesitation to Herman and Joost (Project N forever!). Thank you Christiaan, Arjen, Genya, Fatwa, Andrea, Cédric, Moreno, Petra, Peter, Ruud, Digda, Kohta, Hans, Wim, Ellen, Ruben, Ruben, Roel, Yongqi, Thijs, Ali, Qingping, Tobias, Heleen, Anne, Mercedes, Andreas, George, Jicheng, Borja, Evert, Maarten, Aaike, Tsveta, Ewa, Roberto, Soledad and many others for the excellent times we had and have in the lab, during our coffee breaks or with a borrel in the garden.

I also really enjoyed the year I spent at the condensed matter physics group at the VU in Amsterdam, a year in a different yet equally excellent atmosphere. I learned a great deal there. Many thanks to Martin, Kier, Jan, Davide, Audrius, Grzegorz, Dhwajal, Rinke, Rene, Matteo, Valerio, Sven, Marta and Andrea C.

Voor hun steun en onvoorwaardelijke gastvrijheid als ik weer eens op eigen uitnodiging kwam eten, veel dank aan mijn familie, in het bijzonder Maurice, mama, papa en oma en natuurlijk Charlotte en Job.

Aan mijn vrouw Justine betuig ik mijn grootste dank, vooral voor haar altijd vrolijke en liefdevolle aanwezigheid en gezelligheid. Ik kijk uit naar onze toekomstige avonturen samen!

Curriculum Vitae

Lennard Mooij was born on July 4, 1983 in Woerden, The Netherlands. After finishing pre-university education at the Vrijzinnig Christelijk Lyceum in The Hague in 2001, he moved on to finish a BSc in Molecular Science and Technology at Leiden University and Delft University of Technology. As he started to become more interested in the chemistry and physics of solid state materials, he moved on to receive a MSc degree in Materials Science and Engineering at Delft University of Technology in January 2009. During the work on his master thesis under supervision of dr. ir. Roel van de Krol, entitled “Photo-electrochemical and Optical Properties of $BiVO_4$”, his broad interest in sustainable energy and sustainable hydrogen in perticular further increased. In February 2009 he started his Ph.D. research at the VU University Amsterdam under supervision of prof. dr. Bernard Dam in the Condensed Matter Physics group headed by prof. dr. Ronald Griessen. After one year, he continued his research at his alma mater, after the move of the metal hydride related projects to the Materials for Energy Conversion and Storage group, now headed by Bernard Dam, at Delft University of Technology. The results of this research project obtained at both universities are described in this thesis. Since june 2013 he is a postdoctoral researcher in the same group at Delft University of Technology. He lives with his wife Justine in Amsterdam.